Inspired by Nature: materials biomimicry to support human activities

Doctoral Dissertation
Doctoral Program in Materials Science and Technology (29th Cycle)

Inspired by Nature
Materials biomimicry to support human activities

By

Pierluigi Freni

******

Supervisor(s):
Prof. Sabrina Grassini, Supervisor
Prof. Paolo Fino, Co-Supervisor

Doctoral Examination Committee:
Prof. Luigi De Nardo, Referee, Politecnico di Milano
Prof. Federica Bondioli, Referee, Università degli Studi di Parma

Politecnico di Torino
2017

Declaration

I hereby declare that, the contents and organization of this dissertation constitute my own original work and does not compromise in any way the rights of third parties, including those relating to the security of personal data.

Pierluigi Freni

2017

* This dissertation is presented in partial fulfillment of the requirements for **Ph.D. degree** in the Graduate School of Politecnico di Torino (ScuDo).

Contents

List of Figures

List of Tables

Chapter 1

Biomimicry in biomedical applications

The classes of materials used in the biomedical field are manifold: metals, ceramics, polymers and their composites. All these materials are often used in synergic combination in order to meet different requirements. In the design of a biomedical device and in the selection of the materials it is made of, the requirements are particularly stringent since, in addition to carry out its primary function, the device itself must not hamper the host body.

Therefore, biomaterials must, first and foremost, ensure biocompatibility.

Aiming at the synergic integration of implanted biomaterials with the host organism, a design framework results crucial: biomimicry. It is straightforward to get inspiration from structures and solutions occurring in Nature in order to design devices intended to operate in symbiosis with a living organism [1].

The work presented in this thesis was conceived and developed within such outlook. Two major topics were addressed: ElectroActive Polymers (EAPs), used as artificial muscles and Magnesium foams, used as orthopaedic implants.

As far as EAPs are concerned, it was studied their implementation in actuation devices manufactured according to bioinspired geometries, which can reproduce as faithfully as possible the structure of natural muscle tissues. In fact, in line with the principles of biomimicry, the structures proposed recall the human physiology of

muscle bundles and allow the integration of a recruitment mechanism of the motor units [2], [3].

EAPs have a typical transducers behaviour: if prompted with an electric signal (in particular a voltage), they react with a mechanical deformation, and vice versa. Therefore, EAPs can be described as smart materials, suitable to be used both as actuators and as sensors. As actuators, EAPs have several advantages over the solutions currently present in the state of the art of traditional robotics. In fact, EAPs allow more fluid and biomimetic movements, if compared to those achievable with mechanical counterparts: polymers are flexible and not limited by the rigidity of devices relying on gears and bearings. For this reason, and thanks to stress and deformation values similar to those of biological tissues, EAPs are also referred to as "artificial muscles" [3]-[6].

As far as magnesium foams are concerned, within a biomimicry outlook, the context of orthopaedic surgery sets the morphology of natural bone as reference. Designing choices regarding materials selection, production methods and treatments (in bulk and/or on surface) were addressed to reproduce the mechanical and functional features of natural bone. In fact, if on one side the orthopaedic implant is required not to collapse under the mechanical load applied, on the other it should not bear excessively or exclusively the forces acting on the bone in order not to induce a *stress-shielding* effect. This phenomenon, in fact, may be critical since it reduces considerably the stimulation of regenerative bone cells and, ultimately, slows down the recovery of natural bone. The natural bone has a complex structure, resulting from millions of years of evolution, which fulfils several functions: it provides specific structural support, locally adapted to load conditions; it does not add unnecessary weight by means of an optimized minimization of mass and it allows nutrients supply to tissues through adequate vascularization. Such multi-functionality is enabled by the peculiar structure of the spongy bone tissue. Starting from these observations, the mimesis of cancellous bone conformation is one of the most appropriate guideline in choosing and designing materials for orthopaedic applications.

Among the feasible technological solutions, metallic foams with open interconnected porosity have been identified as the most promising choice [2]-[5] and this thesis is focused on this solution. In fact, these materials can be designed to combine the mechanical properties and the morphological characteristics of natural bone, as well as the vascularization function and the stimulation of bone tissue growth. Furthermore, metallic foams represent one of the most suitable

option to coherently develop a biomimetic device that reproduces the main features of natural bone.

In the light of the requirements outlined so far, pure magnesium represents an optimal solution. This metallic material in fact meets the multi-functionality requirement previously described: it has mechanical properties of the same order of magnitude as those of natural bone tissue, it can be produced in the form of foam, it is biocompatible and bioresorbable. This last feature enables the possibility to avoid second surgery usually needed to remove orthopaedic devices once their function is fulfilled. Supporting this choice, there is a wide scientific literature which, in recent years, has recognized magnesium as a very promising material for biomedical applications, although there are still some critical aspects to be solved. In fact, the process of corrosion of magnesium in the body fluids results in the formation of gaseous hydrogen that, if produced too rapidly, can be harmful for the human body [4].

Chapter 2

Electroactive polymers

2.1 Introduction

The study related to electroactive polymers, that is presented in the following, originates from the project: “CoSpaR - Soft solutions for hard problems”. The aim of that project was to design a hand exoskeleton that could enhance astronauts’ performance during Extra-Vehicular Activities, which are fundamental for human exploration of space. Environmental conditions and pressurized spacesuits expose astronauts to fatigue problems during lengthy EVAs. Arms and hands are particularly affected. The project was a preliminary study of a possible technological solution able to reduce the fatigue of the astronaut’s hand, while avoiding hindering its natural movements. The challenge was the realization of one or more prototypes of a lightweight hand exoskeleton to be embedded in the astronaut’s glove, in order to overcome the stiffness of the pressurized suit. Both the high complexity of the human hand, in terms of degrees of freedom and working space, and the extreme environment in which the exoskeleton will have to work create a series of different constraints increasing the complexity of the project [6]. This brought the focus on innovative and high-risk solutions designed from scratch for a soft glove. *Soft robotics* was the leitmotiv throughout all the project development and was chosen as opposed to the more traditional *hard robotics* approach. Therefore, the research about the state of the art, as well as the selection and concept design activities, was carried out within a *soft* framework. In the light of the highly innovative field the team worked within, the first phase of the project was devoted to assessing the state of the art of the available exoskeleton solutions.

At the same time information and data were collected in order to have an overview about the technologies representing the edge of development in sensors, control and actuation systems.

Starting from the outcome of this project, further activities were carried out and a complete design methodology for the design of actuators based on multiple Electroactive Polymer (EAP) fibers is here proposed. In addition, the procedure gives an idea of the required parameters that must be clearly modelled and characterized at EAP material level. Finally, the solution proposed was patented [7].

2.2 Materials for actuation and sensing

Since the solution required not to add complexity, rigidity or weight to the spacesuit glove, a traditional *hard* approach was not suitable: in fact, a metal exoskeleton, operated with motors, pumps or compressors, would imply a significant increase in the mass of the spacesuit, as well as a higher stiffness of the system and a reduction of the astronaut dexterity. Thus, *soft robotics* appeared as the best solution for this application. As the name suggests, systems built within this approach are soft, flexible and compliant. Furthermore, it is possible to abate the total weight of the exoskeleton and to get rid of rigid elements constraints. One of the key points of soft robotics is biomimicry: in place of heavy, rigid and noisy motors, *artificial muscles* are in charge of the movement of the soft structure, allowing a number of degrees of freedom unthinkable with traditional mechanics [8]-[12].

The shift from hard to soft robotics brings the focus on materials: actuating and sensing devices are embedded in the material itself, which turns out to be smart. *Smart materials* represent a wide class of materials, belonging to different families (polymers, metal alloys and ceramics) and characterized by a large number of control mechanisms. They can respond to external stimuli of diverse nature, like an applied stress or an imposed strain, a change in temperature, relative humidity or pH of the environment, a magnetic or electric field and so forth. In this variety of possibilities, materials with very different properties may be found.

In the framework of soft robotics and taking into account the requirements of the project (Table 1), polymeric smart materials appeared to be the most suitable choice for the application under study (Figure 1). In particular, the attention was focused on *Electroactive Polymers* (EAPs): these polymeric materials work as transducers, converting electrical inputs into mechanical outputs, and vice versa.

They show features that cannot be traced in other *traditional* functional materials (e.g. piezoelectric ceramics), such as large active strains, high energy density, mechanical compliance and flexibility, very low weight, zero noise emission, simple and scalable structures and tailorable properties. All these characteristics make EAPs the actuation system closest to natural muscles [12], [13].

Table 1 CoSpaR project requirements

Requirement identifier	**Statement**
	Functional requirements
RD_F1	Pinching and grasping with thumb, index finger and middle finger must be augmented.
RD_F2	Total weight shall be minimized.
RD_F3	The device shall fit inside the astronaut glove.
RD_F4	The structure shall not hamper the physiological dexterity.
RD_F5	The power consumption shall be minimized.
	Safety requirements
RD_S1	The device shall not damage the skin of the user.
RD_S2	In case of breakdown, the device shall not be an ignition source.
RD_S3	In case of breakdown, the device shall not constitute electric shock hazard.
RD_S4	In case of breakdown, the structure shall not hamper the physiological dexterity.
RD_S5	The device shall not cause hazards to the mechanical structure of the hand.
	Interface requirements
RD_I1	The user interface shall be seamless.
RD_I2	The device must work always according to the user will.
	Environmental requirements
RD_E1	The device shall operate in a range of temperature between 0°C and 40°C.
RD_E2	The device shall operate in moist environment.
RD_E3	The device shall survive the launch environment.
RD_E4	The device shall withstand the radiation environment of the ISS.
RD_E5	The device shall operate in presence of LEO radiation environment.
RD_E6	The device shall operate at the pressure of 4.3 psi.
RD_E7	The device shall operate in a pure oxygen atmosphere.

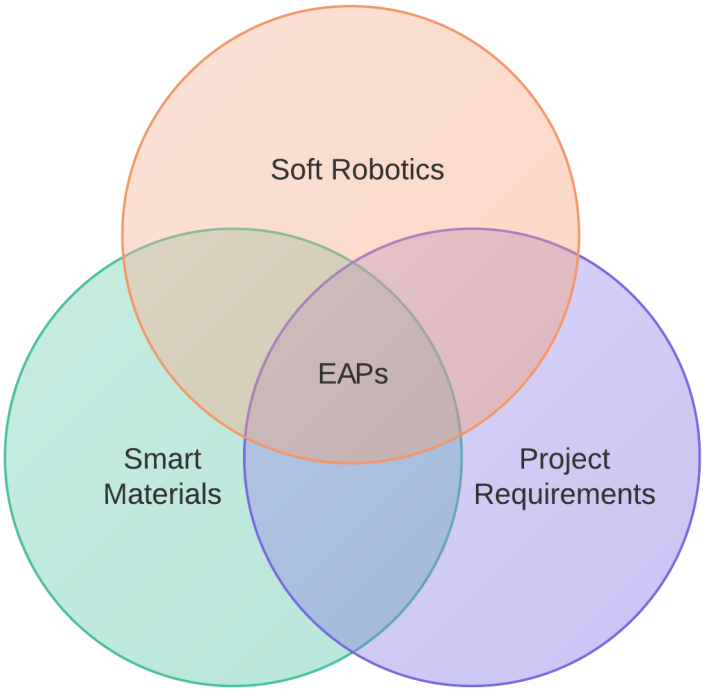

Figure 1 Selection process

Despite the first awareness about the potentialities of Electroactive Polymers may be traced back to 1880, just nowadays this technology is moving from academic laboratories to industrial production and commercialization. Therefore, EAPs represent the cutting edge in the context of functional materials [13], [14].

Electroactive polymers are usually divided into two principal classes, according to their actuation mechanism: ionic EAPs and electronic EAPs. The first group relies on electric activation mediated by charge carriers, i.e. ions and/or molecules, while materials belonging to the latter group respond to the stimulation of an electric field. When the triggering mechanism depends on the diffusion of relatively bulky chemical species, the rate of response is slowed down. Consequently, the actuation speed of ionic EAPs is much slower, compared to electronic EAPs: this is their major drawback. On the other hand, smart polymers actuated by electric fields are able to apply relatively small forces and require very high voltages.

A brief look at some electroactive polymers may be useful to get a general picture about the technology and to analyse advantages and drawbacks of different alternatives.

2.3 Ionic EAPs

2.3.1 Ionic Gels

These materials are hydrogels, i.e. crosslinked polymers which are able to swell if placed in a proper solvent. Acting on the polymer-liquid interaction, the swelling behaviour may be tuned and, therefore, the material can be actuated. Hydrogels are usually responsive to environmental changes in pH or temperature and some of them react also to electric fields. The actuation mechanism relies on the diffusion of the solvent molecules into and out of the polymer network and, for this reason, response rate is quite slow and encapsulation constitutes an issue [12], [13].

2.3.2 Ionic Polymer–Metal Composites

Ionic polymer-metal composites (IPMCs) are made up of a polymer ion exchange membrane, sandwiched between two compliant metal electrodes (percolated nanoparticle of Pt or Au). This technology is based on the peculiar properties of the membrane: it is characterized by an interconnected porosity which let solvents move through it. This way, when a bias voltage is applied, the ions migrate to the oppositely charged electrode, making the polymer swell on one side and shrink on the other, with a net bending of the material. The actuation needs very low tension (in the order of few volts), but the achievable strain is modest. Therefore their application as artificial muscles is limited [12], [13], [15]-[17].

2.3.3 Conducting Polymers

Even if most polymeric materials are insulators, some of them have a chemical structure which turns them into conductors. In particular, the presence of alternated double bonds along the backbone chain (conjugated system) leads to the formation of a *macromolecular orbital*: the π-bonds give rise to a wide resonance structure and the delocalization of the electrons lets charge carriers move almost freely along the polymer chain. Polypyrrole and polyaniline (PANI) are the most widely used conductive polymers. Nevertheless, conductive polymers behave more like semiconductors than pure conductors and, furthermore, they can undergo a reversible doping through redox reactions. The actuation of this electroactive polymer is based precisely on electrochemical processes: by means of doping, electrical charges are localized throughout the chain and the uptake of counterions causes an increase in volume, perpendicularly to the chains orientation. This requires the presence of a liquid electrolyte that has to flow through the polymer.

Conductive polymers suffer from very low operating efficiency (around 1%), limited actuation speed and encapsulation issues [10], [12], [13], [18], [19].

2.3.4 Carbon Nanotubes

Carbon nanotubes (CNTs) are nowadays used in a really wide range of applications, thanks to their peculiar features. In fact, they show outstanding mechanical properties (Young modulus up to 1 TPa) and high conductivity. Moreover, they may be functionalized and used as transducer: if suspended in an electrolyte, carbon nanotubes are able to enlarge thanks to double-layer charge injection. The mechanism is activated applying a potential between CNTs and a counterelectrode; the polarization of CNTs surfaces generates an ion migration in the electrolyte in order to recover the overall electrical neutrality of the system. Due to their high stiffness, achievable strains are small (< 2%); on the other hand, required voltage are low as well (≈ 1 V) [12], [13], [20], [21].

2.4 Electronic EAPs

2.4.1 Piezoelectric Polymers

The molecular structure of piezoelectric polymers contains permanent dipoles, due to the presence of high electronegative halogens atoms in the side groups. These dipoles can be aligned by means of an electric field and, as a result, the material can be polarized permanently. Furthermore, the polarization can be cancelled out applying an opposite bias or bringing the material above a defined temperature, called Curie temperature. In particular, if the material is above its Curie point, a reversible transition between polar and non-polar phase is possible. This is the property exploited to use those materials as actuators. Polyvinylidene difluoride (PVDF) is one of the most common piezoelectric polymers: above its Curie point, which is close to room temperature, the transition between the β paraelectric phase (non-polar) and the α ferroelectric phase (polar) can be induced with an electric field. The phase transition is accompanied by a change in the morphological structure of the polymeric chain and eventually leads to a volume variation. PVDF has lower piezoelectric performances as compared to the ceramic counterpart, but, as a polymer, it is more lightweight and flexible, easier to form and capable to produce two orders of magnitude larger strains. One of the major concerns regarding these materials is the great energy loss due to hysteresis phenomena during polarization [12].

2.4.2 Electrostrictive Polymers

The materials belonging to this group are copolymers based on vinylidene fluoride (VDF) and trifluoroethylene (TrFE) with the same actuation mechanism of piezoelectric polymers. P(VDF-TrFE) has the advantages of a chemically tailorable Curie temperature and a lower energy barrier for the $\alpha - \beta$ phase transition. This results in reduced hysteresis energy loss, higher efficiency and more flexibility on operating temperatures [12], [22].

2.4.3 Liquid Crystal Elastomers

These polymers are characterized by the presence of mesogen phases (typical of liquid crystals) within an elastomeric network. Mesogens are rigid segments that can be oriented in partly ordered structures via thermal or electrical stimuli, causing a deformation of the material. Thermally activated LCEs show very high strains (up to 400%), but their effectiveness is limited by the need for heat diffusion, which slows down the response rate. On the other hand, electrically activated LCEs are much faster, but they can reach lower strains [12], [13].

2.4.4 Dielectric Elastomers

The working principle underlying dielectric elastomers is the same of a capacitor. A dielectric elastomeric thin sheet is covered on both side with conductive flexible material in order to create a capacitor characterized by very compliant electrodes. When a voltage is applied between the two electrodes, the opposite charges on the two faces are attracted, while the like charges on each side repel each other. The resulting effect on the elastomer is a net contraction in thickness and a planar expansion. The actuation voltages are very high (in the order of kilovolts), but the capacitive nature of the solution guarantees little currents and, therefore, very low power consumption. The output stress increases quadratically with the applied electric field and large strains may be achieved. Both silicone rubbers and acrylic elastomers are used as dielectric elastomers. Furthermore, applying a prestrain to the material, efficiency can be highly improved and preferential actuation in one direction can be realized [12], [23], [24].

2.4.5 Carbon Nanotube Aerogels

Differently from the ionic carbon nanotubes, the aerogel solution does not require a liquid electrolyte: carbon nanotubes are parallel arranged in ordered *forests*.

Applying a positive voltage between the CNTs and a grounded electrode, the like charges generated on the surface of nanotubes repel each other causing a transversal expansion. This material has an incredibly low density and it is capable of high and quick strains. One of the few drawbacks is represented by the relatively low forces generated [13], [25].

2.5 Materials selection

The literature about electroactive polymers is still fairly poor in numerical data because these materials are quite recent and the research in the field is fragmented. Therefore, the considered properties have been measured in different conditions and can be used just for a qualitative comparison.

One of the most important properties for the considered application is the *maximum strain* (S_m). In fact, artificial muscles shall be flexible and able to undergo large deformation without getting damaged. The maximum strain is the largest displacement reached, normalized to the initial length of the sample in the direction of actuation and it is described by:

$$S_m = \frac{(L - L_0)}{L_0} = \lambda_m - 1$$

(Eq. 1)

where L is the maximum length of the sample undergoing a uniaxial stretch, L_0 is the initial length and $\lambda_m = L/L_0$ is the longitudinal stretch [24].

Together with the strain, also the stress that the material is able to sustain is important. As far as actuators are concerned, the *maximum pressure* (T_m) is the largest force per cross-sectional area that the material is capable to develop:

$$T_m = \frac{F_m}{A_0}$$

(Eq. 2)

where F_m is the maximum forced applied to the sample and A_0 is its initial cross-section area [24].

Usually, the peak strain and the peak stress do not correspond: it is common to measure the greatest force at zero strain and to have a null stress when the deformation is at its maximum.

To compare different actuation solutions, another metrics is more appropriate: the *actuator energy density* (e_a), i.e. "the maximum mechanical energy output per cycle and per unit volume of material" [26]. This feature takes into account both stress and strain, giving a more comprehensive description of the material:

$$e_a = p \cdot s_z$$

(Eq. 3)

where p is the effective actuation pressure (as detailed in the following par. 2.6) and s_z is the polymer thickness strain. Nevertheless, the *elastic energy density*, equal to the half of the actuator energy density, is conventionally used. Moreover, if the energy is referred to unit mass (dividing it by density), the *Specific elastic energy density* is obtained.

The *Coupling efficiency*, k^2, is defined as the ratio between the energy converted into mechanical work per cycle (U_{mech}) and the electrical energy provided per cycle ($U_{el,input}$) [24]:

$$k^2 = \frac{U_{mech}}{U_{el,input}}$$

(Eq. 4)

It is useful to guarantee a consistent comparison with traditional piezoelectric materials. Low values of this parameter imply that high efficiency in actuation cannot be reached due to large energy loss [26].

For the artificial muscles application, the actuation speed of the material is not negligible. In fact, fast response is needed to guarantee performances as close as possible to natural muscles and to develop a device reliable in a wide range of movements.

An overview of data available in the literature is presented in Table 2. Natural muscles are used as a reference and other technologies are reported for comparison.

At a first sight, some of the electronic EAPs show the largest strains and, even though they do not register the best performances in the maximum pressure, their mechanical properties are comparable with (and slightly superior to) those of natural muscles. For a more comprehensive analysis and coherent selection a multicriteria approach was adopted. The considered properties were: maximum strain, maximum pressure, elastic energy density and relative speed. Furthermore, the values of maximum pressure were normalized on the density, in order to have more homogeneous data.

Data span on such a wide range of values that, to perform an effective comparison, their logarithmic values (on basis 10) needed to be used for the subsequent considerations. Each property of the materials was ranked with a grade, in a scale from 1 to 10, covering the whole range of values so that the lowest one scored 1 and the highest one scored 10. Afterwards, a weighted average was computed and a final grade was assigned to each material (

Table 3). A weighting factor of 2 was assigned to the maximum strain because flexibility and device compliance are of major relevance for the considered application. All the other properties had the same weight (weighting factor of 1). Due to lack of data, some options were penalized, but the results are acceptable for a qualitative assessment.

Table 2 Electroactive polymers: overview on data available in literature

	Type (specific)	Maximum strain	Maximum pressure	Specific elastic energy density	Elastic energy density	Coupling efficiency k^2	Maximum efficiency	Specific density	Relative speed (full cycle)	References
		%	MPa	J/g	J/cm^3	%	%	g/cm^3		
Natural reference	Natural muscle (human skeletal)	40	0,35	0,07	0,07	–	35	1	Medium	[26], [27]
	Natural muscle (peaks in nature)	100	0,8	0,04	0,04	–	40	1	Slow–fast	[10], [12], [27]
Ionic EAPs	Ionic gels (polyelectrolyte)	40	0,3	0,06	0,06	–	30	1	Slow	[26]
	IPMC	3	30	–	–	–	–	1	–	[12], [15], [16]
	Conducting polymer (PANI)	10	450	23	23	1	5	1	Slow	[12], [26], [28]
	Carbon Nanotubes	2	26	200	200	–	–	1	Fast	[10], [12], [13]
Electronic EAPs	Piezoelectric polymer (PVDF)	10	4,8	0,0013	0,0024	7	–	1,8	Fast	[26]
	Electrostrictive polymer [P(VDF–TrFE)]	4,3	43	0,49	0,92	–	80	1,8	Fast	[26], [29]
	Liquid Crystal Elastomers	4	–	–	0,02	–	–	–	Fast	[12]
	Dielectric elastomer (acrylic with prestrain)	380	7,2	3,4	3,4	85	60–80	1	Medium	[10], [12], [26], [30]
	Dielectric elastomer (silicone with prestrain)	63	3	0,75	0,75	63	90	1	Fast	[12], [30]
	Dielectric elastomer (silicone - nominal prestrain)	32	1,36	0,22	0,2	54	90	1	Fast	[26]
	Carbon Nanotubes Aerogels	220	16	0,03	–	–	–	0,0015	Fast	[25]
Other materials	Piezoelectric ceramic (PZT)	0,2	110	0,013	0,1	52	90	7,7	Fast	[26]
	Piezoelectric single crystal (PZT-PT)	1,7	131	0,13	1	81	90	7,7	Fast	[26]
	Shape memory alloy (TiNi)	5	200	15	100	5	10	6,5	Slow	[26]
	Magnetostrictive (Terfenol-D)	0,2	70	0,0027	0,025	–	60	9	Fast	[26]
	Electrostatic devices (integrated force array)	50	0,03	0,0015	0,0025	50	90	1	Fast	[12], [26]
	Electromagnetic (Voice Coil)	50	0,1	0,003	0,025	–	90	8	Fast	[12], [26]

Table 3 Grades for each material properties

	Type (specific)	Maximum pressure/ρ	Maximum strain	Elastic energy density	Relative speed (full cycle)	Final grade
Natural reference	Natural muscle (human skeletal)	3	8	3	5	**5,40**
	Natural muscle (peaks in nature)	4	9	3	5	**6,00**
Ionic EAPs	Ionic gels (polyelectrolyte)	3	8	3	1	**4,60**
	IPMC	6	4	0	0	**2,80**
	Conducting polymer (PANI)	8	6	9	1	**6,00**
	Carbon Nanotubes	6	4	10	10	**6,80**
Electronic EAPs	Piezoelectric polymer (PVDF)	4	6	1	10	**5,40**
	Electrostrictive polymer [P(VDF–TrFE)]	6	5	6	10	**6,40**
	Liquid Crystal Elastomers	0	4	2	10	**4,00**
	Dielectric elastomer (acrylic with prestrain)	5	10	7	5	**7,40**
	Dielectric elastomer (silicone with prestrain)	5	8	6	10	**7,40**
	Dielectric elastomer (silicone - nominal prestrain)	4	7	4	10	**6,40**
	Carbon Nanotubes Aerogels	10	10	0	10	**8,00**
Other technologies	Piezoelectric ceramic (PZT)	6	1	4	10	**4,40**
	Piezoelectric single crystal (PZT-PT)	6	3	6	10	**5,60**
	Shape memory alloy (TiNi)	6	5	10	1	**5,40**
	Magnetostrictive (Terfenol-D)	5	1	3	10	**4,00**
	Electrostatic devices (integrated force array)	1	8	1	10	**5,60**
	Electromagnetic (Voice Coil)	1	8	3	10	**6,00**

In this evaluation, the *Natural muscle (peaks in nature)* scores 6/10: therefore, all the alternatives with higher grades are “sufficient” and suitable candidates for artificial muscles applications, even though further considerations are needed.

The ranking list is reported in Table 4. The top performing option is represented by *Carbon Nanotubes Aerogels*. This is a promising technology, even though at the very first stage of development: it gets the maximum score (10) in pressure provided, strain and actuation speed. Data about energy are missing and further investigations are needed. Thanks to its dramatically low density due to the aerogel

formulation, stiffness provided by carbon nanotubes and large achievable strains enabled by the actuation mechanism, CNT Aerogels are potentially the best option. The state of the art of the technology is still too immature for an application in the short-medium term and, therefore, it was disregarded for the moment.

Table 4 Ranking list of the alternative materials

Rank	Type (specific)	Final grade	Rank	Type (specific)	Final grade
1	Carbon Nanotubes Aerogels	**8**	11	Electrostatic devices (integrated force array)	**5,6**
2	Dielectric elastomer (silicone with prestrain)	**7,4**	12	Shape memory alloy (TiNi)	**5,4**
3	Dielectric elastomer (acrylic with prestrain)	**7,4**	13	Piezoelectric polymer (PVDF)	**5,4**
4	Carbon Nanotubes	**6,8**	14	Natural muscle (human skeletal)	**5,4**
5	Electrostrictive polymer [P(VDF–TrFE)]	**6,4**	15	Ionic gels (polyelectrolyte)	**4,6**
6	Dielectric elastomer (silicone - nominal prestrain)	**6,4**	16	Piezoelectric ceramic (PZT)	**4,4**
7	Conducting polymer (PANI)	**6**	17	Magnetostrictive (Terfenol-D)	**4**
8	Electromagnetic (Voice Coil)	**6**	18	Liquid Crystal Elastomers	**4**
9	**Natural muscle (peaks in nature)**	**6**	19	IPMC	**2,8**
10	Piezoelectric single crystal (PZT-PT)	**5,6**			

The second and the third places are occupied by *Dielectric elastomers*. Both solutions require a material prestrain to guarantee high performances and, in this respect, the possibility to tailor a preferential direction of actuation represents a plus, according to the project requirements. Furthermore, this technology is already available on the market and its development has already reached a quite mature state.

Carbon nanotubes have such a high grade mainly thanks to the great elastic energy density and the fast actuation response. Nevertheless, they are not appropriate for the project application because they need a liquid electrolytic medium to work, with all the resulting complications (encapsulation of the device), and they have a very poor maximum strain.

Electrostrictive polymer [P(VDF-TrFE)] scores a sufficient mark, thanks to the relatively high pressure that it is able to provide and the fast response. Anyway, it still has some drawbacks: the maximum strain achievable, reported in literature, is small and the actuation mechanism is highly temperature dependent. The latter

feature represents an important constraint for space application because proper working cannot be guaranteed in presence of large thermal excursions, typically registered during extra-vehicular activities.

PANI, a conductive polymer, results sufficient: it is characterized by the highest maximum pressure and it shows good elastic energy density, but its actuation response is slow and its maximum strain limited.

IPMC and *Liquid Crystals Elastomers* pay the price of missing information, resulting in an underestimation of their actual performance. For this reason, further investigations and, possibly, testing are required.

In order to have a graphical outlook, the top-score results have been reported in Figure 2.

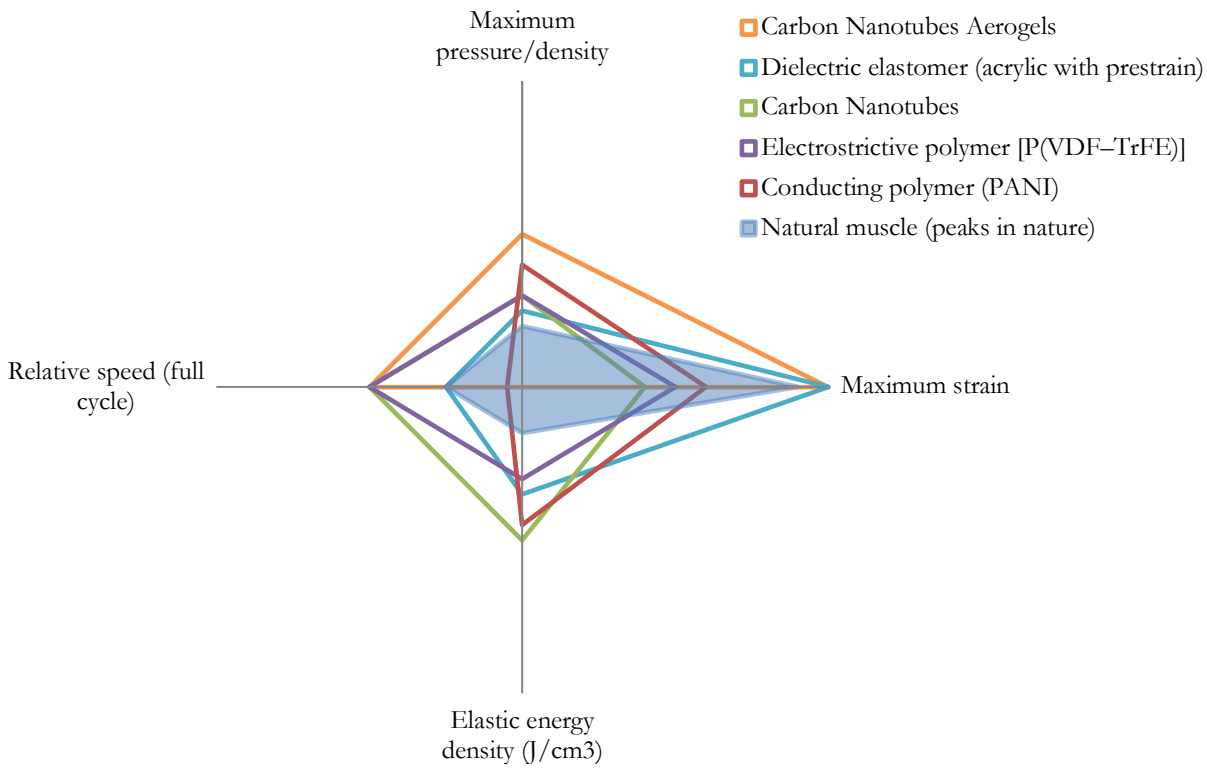

Figure 2 Radar chart of the top-score options

Each shape represents a material and its dimensions are given by the score obtained in the four considered properties: the bigger is the shape, the better is the

performance of each alternative. The reference, *Natural muscle (peaks in nature)*, is indicated by the filled quadrangle. Despite the *Carbon Nanotubes Aerogel* presents the largest area, the *Dielectric elastomer (acrylic with prestrain)* has a shape analogous to the natural muscle's one, but larger: this is an additional confirmation of the fact that the Dielectric Elastomers option is consistent with the reference and, therefore, adequate for artificial muscles application.

Further considerations for the material comparison may be drawn from a Pareto efficiency[1] analysis of the available alternatives. For each material, two parameters (to be optimized) were chosen: maximum pressure, divided by density, and maximum strain. The inverse of the logarithm on base 10 of both quantities was then computed and taken into account. The resulting plot is reported in Figure 3: each bubble represents a candidate material and the alternatives which perform better, with respect to the parameters considered, are the closest to the axes origin. Looking at the chart, there is no option that minimizes, at the same time, both the parameters; therefore, a trade-off curve (Pareto front) has was traced. The bubbles on the Pareto front are *not dominated* by any other possibility and they are Pareto efficient, while all the others are *dominated* and do not optimize the performance.

The not dominated solutions are the *Carbon Nanotubes Aerogel* and the *Dielectric elastomer (acrylic with prestrain)*. These materials present the best combinations of maximum pressure and maximum strain and, in this context, are the best alternatives.

According to the available data and the previous considerations, the ***dielectric elastomers*** represent the best compromise for the intended application. In fact, they allow large strains and both maximum pressure and energy density are superior to (but of the same order of magnitude of) the natural muscles' ones. Those features make them the favorite candidates to perform as artificial muscles, intended to help astronauts in their extra-vehicular activities: in fact they should provide enough pressure without further limiting dexterity and with no risk of hurting the user.

[1]. In the engineering context, Pareto efficiency is a useful selection method. Each option is first assessed under multiple criteria and then a subset of options is identified with the property that no other option can categorically outperform any of its members.

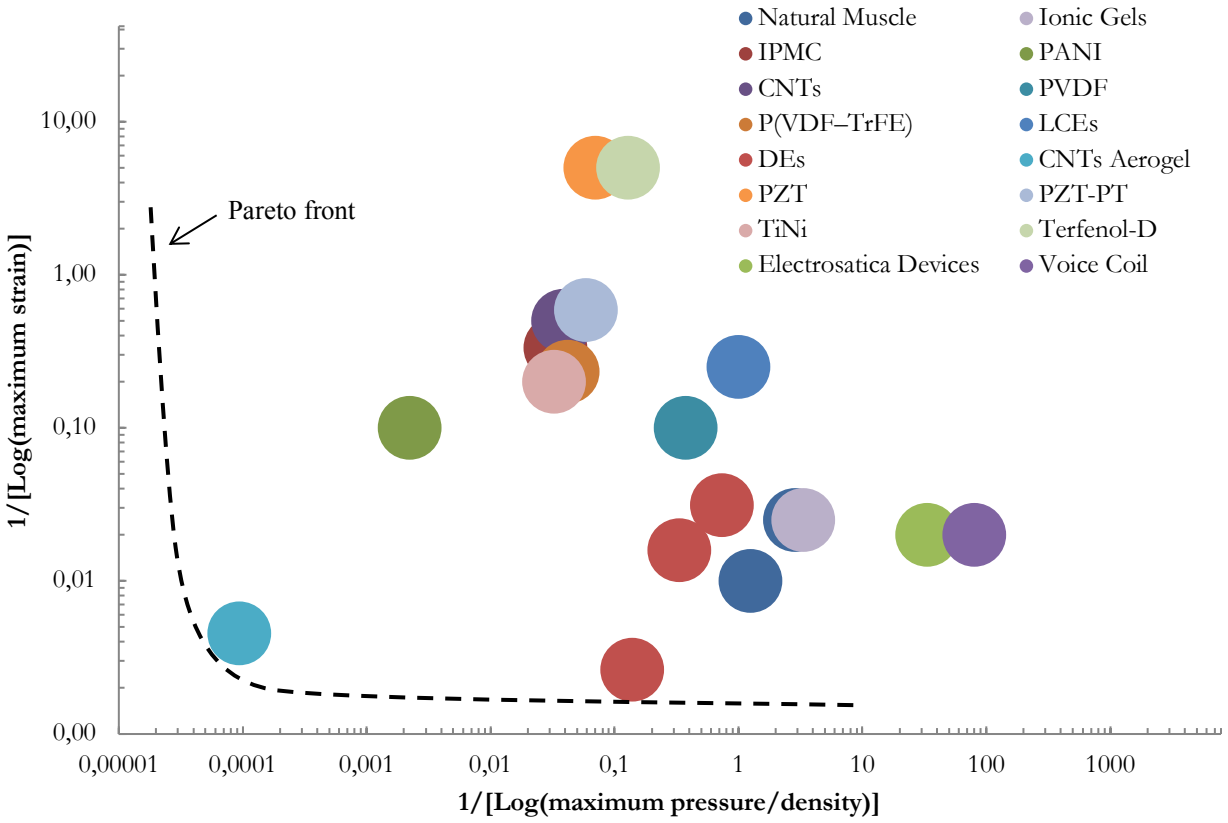

Figure 3 Materials bubble chart with Pareto front

2.5.1 Dielectric elastomers materials

Elastomeric materials are usually characterized by a hyperelastic behaviour, i.e. the stress-strain curve presents three regions (Figure 4): a first linear region with a relatively "high" stiffness, followed by a *plateau* region, in which the Young modulus drops, and culminating in a *stretch-hardening* region, in which the elastomer becomes stiffer again.

Among the candidates for dielectric elastomer actuators, three groups of polymers were identified: silicones, polyurethanes and acrylic elastomers. The mechanical and electrical properties of few representatives of those groups of materials are presented in Table 5.

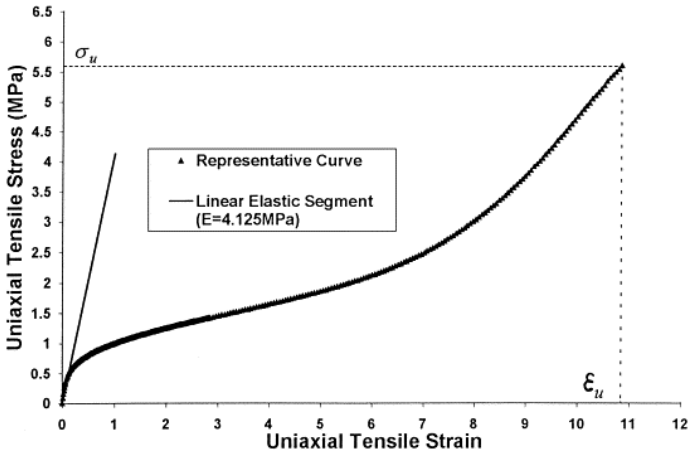

Figure 4 Typical stress-strain curve for an elastomer

Table 5 Comparison of some dielectric elastomers properties

Polymer (specific type)	Prestrain	Energy density	Maximum actuation pressure	Thickness strain	Area strain	Young's modulus	Breakdown electric field	Dielectric constant	Efficiency	Reference
	(x%, y%)	MJ/m^3	Mpa	%	%	MPa	MV/m		%	
Silicone (Nusil CF19-2186)	(45, 45)	0,75	3	39	64	1,0	350	2,8	79	[23]
Polyurethane (Deerfield PT6100S)	–	0,087	1,6	11	–	17	160	7	–	[26]
Acrylic (3M VHB 4910)	(300, 300)	3,4	7,2	61	158	3,0	412	4,8	80	[23]

2.5.2 Effects of prestrain on dielectric elastomers

Prestraining the elastomeric dielectric film, it is possible to increase its properties and improve the functioning of the actuator device as a whole. The material benefits from the prestrain application in terms of higher breakdown strength, better mechanical efficiency and faster actuation response, with just a limited reduction of the dielectric constant [12].

Furthermore, by means of prestrain, a tailorable anisotropy can be introduced in the material. With a proper design of the device, it is therefore possible to reach a preferential direction of actuation "by applying high prestrain in the direction

perpendicular to the desired actuation direction and low prestrain along the actuation direction" [12].

Although prestrain brings many advantages, it requires a framing structure to keep the material in mechanical tension during actuation. This adds complexity to the device itself, increasing its mass and volume, and needs a focused design process.

2.6 Dielectric Elastomers modelling

As previously mentioned, the working principle of a dielectric elastomers (DEs) actuator is grounded in its capacitive nature: it is modelled as a parallel plate capacitor with dielectric made of a linearly elastic material. The application of bias causes a contraction in thickness of the dielectric, due to the electrostatic attractive force between the two electrodes, and a planar expansion in the other two directions (Figure 5).

The dielectric material can be reasonably assumed to be incompressible, therefore:

$$l \cdot w \cdot t = cost$$

(Eq. 5)

where l is the length, w the width and t the thickness of the dielectric. Or alternatively:

$$(1 + s_x)(1 + s_y)(1 + s_z) = 1$$

(Eq. 6)

where s_x, s_y and s_z are the strains in the three directions.

The electrostatic stress generated across the electrodes is the Maxwell pressure, described by:

$$p = \varepsilon_r \cdot \varepsilon_0 \cdot E^2$$

(Eq. 7)

where ε_r is the material relative dielectric constant, ε_0 is the vacuum dielectric constant and E is the applied electric field. Furthermore, the previous equation can be written as a function of voltage V and dielectric thickness t:

$$p = \varepsilon_r \cdot \varepsilon_0 \cdot \left(\frac{V}{t}\right)^2$$

(Eq. 8)

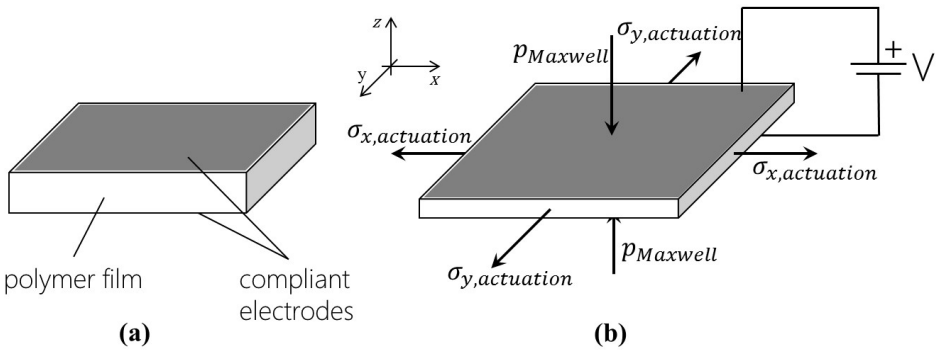

Figure 5 Working principle of dielectric elastomers

2.6.1 Free boundary condition

To a first approximation, the dielectric material was considered linearly elastic and isotropic (with a Young Modulus Y) and a free boundary condition[2] was assumed for the actuator. Under those hypotheses, the thickness strain is given by:

$$s_z = -\frac{p}{Y} = -\frac{\varepsilon_r \cdot \varepsilon_0 \cdot E^2}{Y} = -\frac{\varepsilon_r \cdot \varepsilon_0 \cdot (V/t)^2}{Y}$$

(Eq. 9)

[2]. When no constraint is applied to the DE actuator, the electrostatic pressure (Eq. 7) strains the polymeric film until the elastomer's elastic stress (spring back effect) prevents further expansion.

This simple model is valid only for small strains (<10%). For larger deformation, maintaining the linear elasticity assumption, another model has been put forward by Pelrine et al. [12], [31]:

$$s_z = \frac{2}{3} + \frac{1}{3}\left[f(s_{z0}) + \frac{1}{f(s_{z0})}\right]$$

(Eq. 10)

where

$$f(s_{z0}) = \left[2 + 27s_{z0} + \frac{[-4 + (2 + 27s_{z0})^2]^{1/2}}{2}\right]^{1/3}$$

(Eq. 11)

and

$$s_{z0} = -\frac{\mathrm{p}}{Y} = -\frac{\varepsilon_r \cdot \varepsilon_0 \cdot E^2}{Y} = -\frac{\varepsilon_r \cdot \varepsilon_0 \cdot (V/z_0)^2}{Y}$$

(Eq. 12)

In the free boundary condition the strains in the *x* and *y* direction can be considered equal

$$s_x = s_y = s_a$$

(Eq. 13)

and, therefore, recalling the constant volume constraint (Eq. 6) and solving for s_a:

$$s_a = (1 + s_z)^{-0,5} - 1$$

(Eq. 14)

A comparison of the two models was performed (Figure 6): the large deformation (Eq. 10) provided values of strain higher than those resulting from the equation valid for small deformations (Eq. 9).

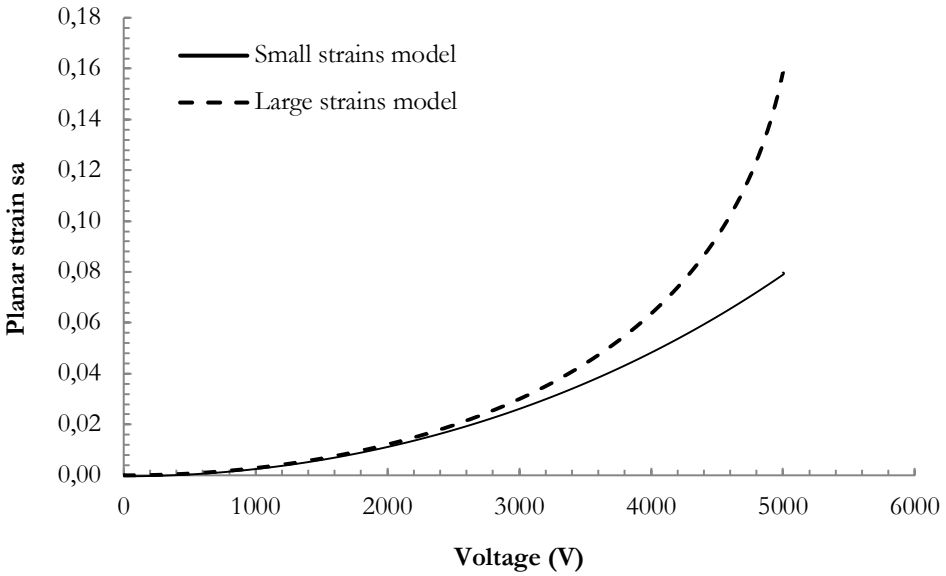

Figure 6 Small strains and large strains models compared

Both the previously described models are hookean, i.e. they assume the Young modulus to be constant throughout all the deformation process. Actually, elastomeric materials usually show a viscoelastic, time-dependent behavior and are non-hookean. More accurate models, which take into account those features of the material, have been developed [12], but for the preliminary assessment aimed in this work, the hookean model represents a reasonably good approximation. Furthermore, according to their typical mechanical behavior, elastomers show a decrease in elastic modulus with increasing strains. Therefore, the application of a hookean model gives an overestimation of the material stiffness and the predicted strains will be lower than those really achievable during actuation (Eq. 9 shows that strain and Young modulus are inversely proportional). Eventually, the use of the simple hookean approach will bring to an underestimation of the actuation strains and to an over dimensioning of the system (conservative approach).

2.7 Actuator multilayer design

The actuation device is based on the selected electroactive polymers, the dielectric elastomers. DEs proved to be the best trade-off in terms of deformability and maximum stress they are able to apply. According to their working principle, these smart polymeric materials are linear actuators, i.e. they apply a stress along a plane,

mainly in one direction (if prestrained). On the other hand, the finger joints need a bending actuation and, therefore, an appropriate design of the device becomes necessary.

The adopted solution is based on the unimorph cantilever working principle: the coupling of a DEs layer with a passive layer results in an overall bending of the device (Figure 7).

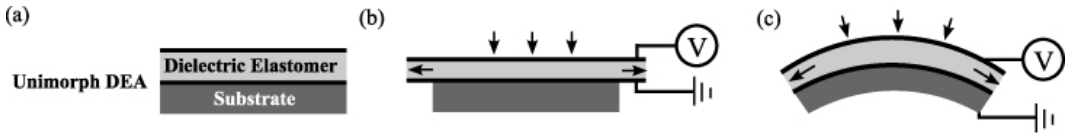

Figure 7 Unimorph DE actuators working principle

Due to the peculiarity of finger joints, aside from bending, the device needs also to linearly elongate. For this reason it is not possible to use a passive stiff layer in the unimorph design.

Consequently the multilayer structure designed is made of N active layers. In the example presented in Figure 8 $N=5$. Each layer performs a different linear elongation, so that $\varepsilon_5 > \varepsilon_4 > \varepsilon_3 > \varepsilon_2 > \varepsilon_1$. The resulting actuation is both a linear expansion along the finger and a bending on the joint.

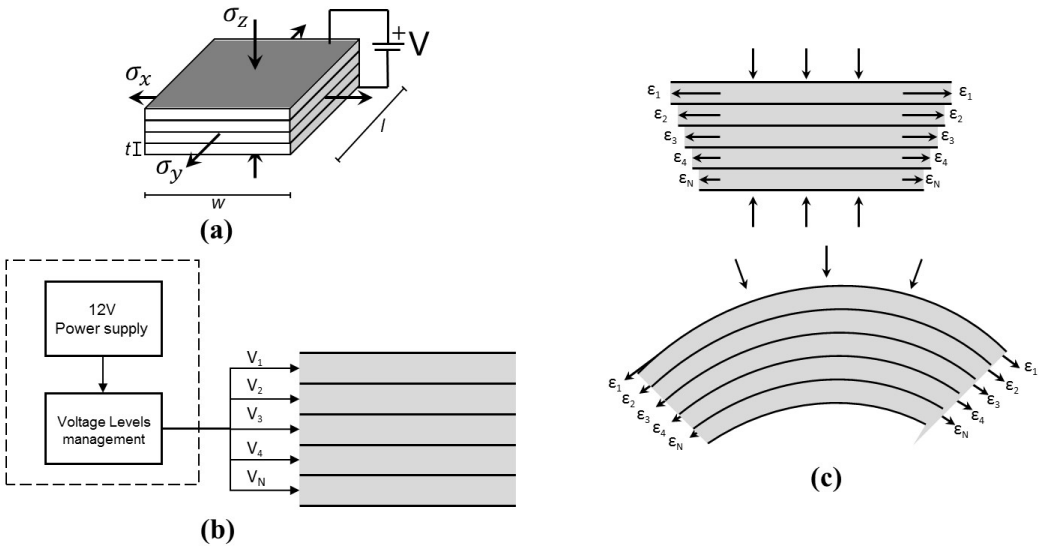

Figure 8 Multilayer Elongation and Bending Actuator (MEBA). (a) No voltage applied. (b) The application of different voltages causes different linear elongations. (c) The resulting deformation is both a linear elongation and a bending.

To achieve a gradient of linear strains across the device's thickness, a different voltage is applied on each layer. According to the considerations previously drawn, the planar strain along the polymeric dielectric increases with the bias applied and, therefore

$$\varepsilon_5 > \varepsilon_4 > \varepsilon_3 > \varepsilon_2 > \varepsilon_1 \Leftrightarrow V_5 > V_4 > V_3 > V_2 > V_1$$

As a result, applying the proper voltage to each layer, the device actuates according to the requirements, remaining compliant with the finger. The device described above has been named MEBA (Multilayer Elongation and Bending Actuator).

Figure 9 shows the arrangement on the index finger of the three MEBAs, one for each joint (MCP in green, PIP in red and DIP in yellow). Every MEBA needs to be dimensioned according to the specific geometry of the joint and to the loading conditions.

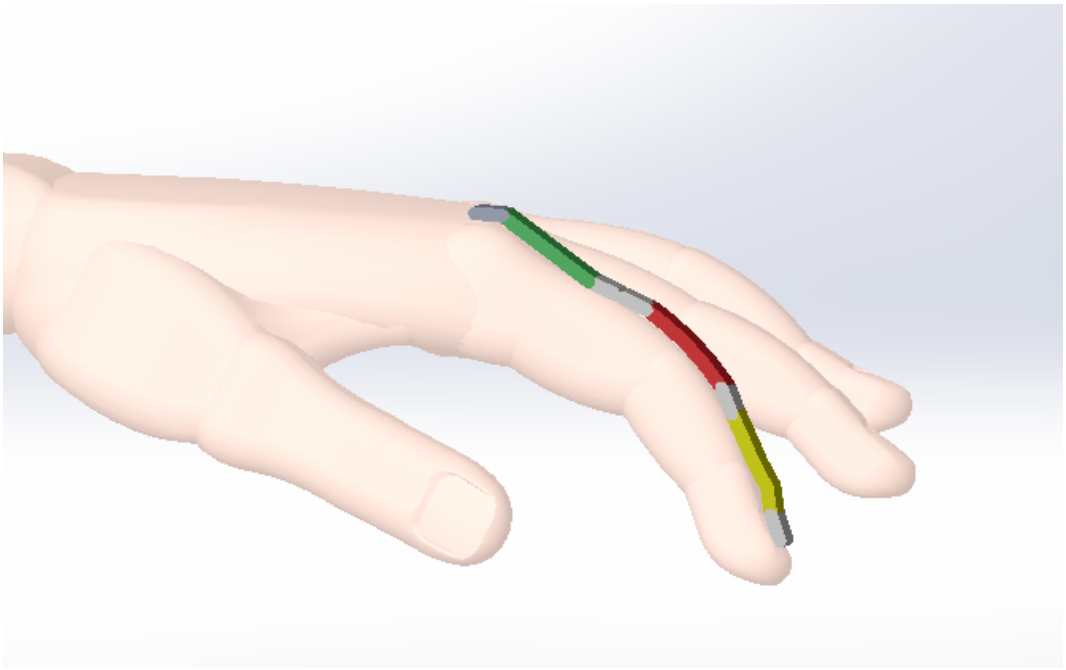

Figure 9 MEBAs arrangement on the index finger

2.7.1 Kinematics and dynamics specifications

The needed actuation obviously depends on the applied external forces and on the way these forces are translated to torques on finger joints. After having identified the torque on each joint, the interaction between finger and actuation and the geometrical and physical characteristics of the Elastomer, it is possible to define the maximum stress acting on Elastomer. This is also the stress the Elastomer must provide by means of voltage-stress relationship; thus, we will verify the coherence between available actuation stress and required stress.

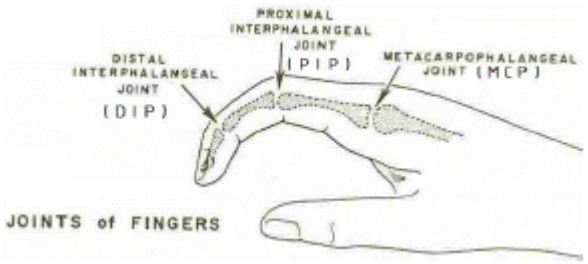

Figure 10 Joints of finger

Several studies [32] have been performed on hand-tools interactions to identify the forces applied by the hand in actions similar to the ones that astronauts do in EVAs. Obviously, we start from an experimentally identified set of forces and we multiply them for a coefficient to assure that the actuation can provide the maximum required force.

Table 6 Forces of the finger joints [32]

Motions	**Force (N)**
Finger MCP joint	3,92
Finger PIP and DIP joint	8,82
Lateral motion of thumb	7,84
Thumb MCP joint	6,86
Thumb PIP and DIP joints	5,39

The needed torques are calculated,

$$\begin{Bmatrix}\tau_1\\ \tau_2\\ \tau_3\end{Bmatrix} = \mathrm{J}_1(\boldsymbol{q})^T \cdot \begin{Bmatrix}F_{x1}\\ F_{y1}\end{Bmatrix}, \qquad \begin{Bmatrix}\tau_1\\ \tau_2\\ \tau_3\end{Bmatrix} = \mathrm{J}_2(\boldsymbol{q})^T \cdot \begin{Bmatrix}F_{x2}\\ F_{y2}\end{Bmatrix}, \qquad \begin{Bmatrix}\tau_1\\ \tau_2\\ \tau_3\end{Bmatrix} = \mathrm{J}_3(\boldsymbol{q})^T \cdot \begin{Bmatrix}F_{x3}\\ F_{y3}\end{Bmatrix}$$

And their sum give us the total torques.

$$\begin{Bmatrix}\tau_1\\ \tau_2\\ \tau_3\end{Bmatrix} = \mathrm{J}_1(\boldsymbol{q})^T \cdot \begin{Bmatrix}F_{x1}\\ F_{y1}\end{Bmatrix} + \mathrm{J}_2(\boldsymbol{q})^T \cdot \begin{Bmatrix}F_{x2}\\ F_{y2}\end{Bmatrix} + \mathrm{J}_3(\boldsymbol{q})^T \cdot \begin{Bmatrix}F_{x3}\\ F_{y3}\end{Bmatrix}$$

The calculations for all the positions are necessary to identify the maximum absolute torques, the maximum torque required at maximum rotation, and to understand if there are positions in which specifications are less strict.

With rough calculation is easy to find, in the most critical configuration, the following values of torques. We assume as forces values the ones reported in the table in order to have the chance to totally sustain the external loads by mean if the robotic glove.

$$\begin{Bmatrix}\tau_1\\ \tau_2\\ \tau_3\end{Bmatrix} = \mathrm{J}_1(\mathbf{0})^T \cdot \begin{Bmatrix}0\\ 3.92\ N\end{Bmatrix} + \mathrm{J}_2(\mathbf{0})^T \cdot \begin{Bmatrix}0\\ 8.82\ \ N\end{Bmatrix} + \mathrm{J}_3(\mathbf{0})^T \cdot \begin{Bmatrix}0\\ 8.82\ N\end{Bmatrix}$$

$$\begin{Bmatrix}\tau_1\\ \tau_2\\ \tau_3\end{Bmatrix} = \begin{Bmatrix}\mathbf{7.9 \cdot 10^{-1}\ Nm}\\ \mathbf{2.4 \cdot 10^{-1}\ Nm}\\ \mathbf{4.4 \cdot 10^{-2}\ Nm}\end{Bmatrix}$$

These are approximate values that are useful to evaluate the feasibility of the solutions we analyse. We remind that the torque τ_1 calculated in this way is referring to the joint MCP, the torque τ_2 to the PIP and τ_3 to DIP.

2.7.2 Structural model of the actuator

Actuation is provided by the three MEBAs put on the upper side of the finger, each one corresponding to a joint. The functioning of the three joints is analogue, thus we can analyse only one of them. In particular the PIP joint was considered; with appropriate changes, the found solution can be adapted to the other joints of the finger.

The actuator, in contact with the end, exchanges a train of loads to maintain the finger in equilibrium state or to provide a rotation to it. A first modeling can be the one depicted in Figure 11. The momentum reported is caused by the external forces, whose relationship and value are explained above.

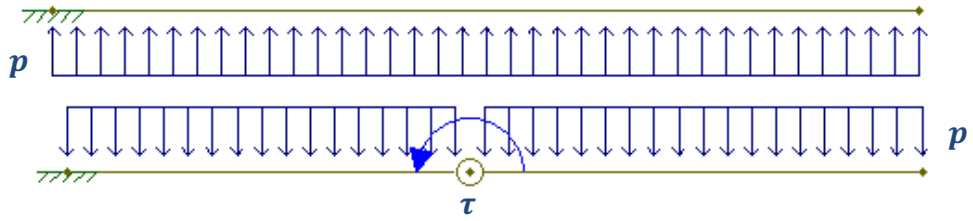

Figure 11 Interaction model between actuator (top) and finger (bottom)

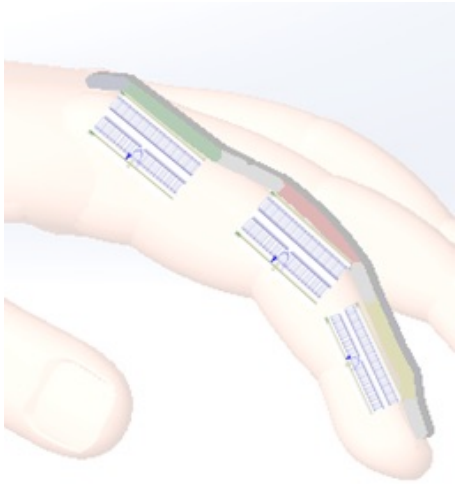

Figure 12 Visual representation of the interaction between actuator and finger

The two elements are grounded because the finger is joined to the hand and the actuator is joined to the previous one, blocked by the control. In order to consider the worst situation, we substitute the pressure load train with a concentrated force at the end of the contact area between the actuator and the finger.

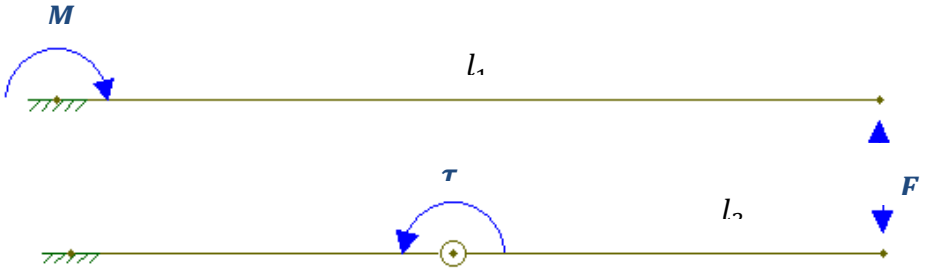

Figure 13 Simplified interaction model between actuator (top) and finger (bottom)

The maximum momentum the actuator has to sustain is given by the simple expression:

$$M_{max} = \tau \cdot \frac{l_1}{l_2} = 2\tau$$

From now on, we will focus on the second joint (PIP), because the CMC is in a position allowing more space for the actuator, so that it would not be a problem to increase the dimension of the MEBA to sustain a larger momentum. The DIP joint has such a small torque that dimensioning is not critical.

The maximum mechanical stress required to apply this momentum, referring to the structure of MEBA, and with the reasonable hypothesis that the number of elements it is large enough, could be calculated this way:

$$M_{max} = b \cdot \sum_{1=i}^{N} \sigma_i \cdot y_i \cdot h_i = b \cdot \int_{-\frac{t}{2}}^{\frac{t}{2}} \sigma \cdot y \cdot dy$$

In which b is the width, y is the vertical coordinate (with the origin in the middle of the section), and h_i is the thickness of each layer. The MEBA is actuated to have a linear distribution of σ, written as the sum of a mean value σ_t, and a linear zero mean component, $\sigma_f = \sigma_{max,f} \cdot \frac{y}{t/2}$, where t is the thickness of the MEBA.

$$M_{max} = b \cdot \int_{-\frac{t}{2}}^{\frac{t}{2}} \left(\sigma_t + \sigma_{max,f} \cdot \frac{y}{t/2} \right) \cdot y \cdot dy = \sigma_{max,f} \cdot b \cdot \frac{t^2}{6}$$

$$\sigma_{max,f} = \frac{M_{max}}{b \cdot \frac{t^2}{6}}$$

So, the maximum stress is given by the sum of the spring back effect and of the momentum given to equilibrate the structure.

The elastic return effect depends on the rotation of the considered joint. In fact, being the neutral axis not in the center of the MEBA, it will be subjected to a linear deformation with mean value different from zero.

The maximum bending strain is computed from:

$$\varepsilon_{f,max} = \frac{y_{max}}{\rho} = \frac{t}{2\rho} = \frac{t}{2\left(l_\rho + \frac{t}{2}\right)}$$

Where ρ is the curvature radius, which split in two components, one depending from the height of the material $\frac{t}{2}$ and the remaining being l_ρ. The curvature radius obviously depends on the performed rotation.

The mean strain of the section is easily computed considering the curvature radius again. In fact, the overall mean deformation is given by the arc of the created circumference and the strain is computed in the following way:

$$r \cdot \alpha = \Delta L \implies \varepsilon_t = \frac{r \cdot \alpha}{L_0} = \frac{\left(\frac{h_f}{2} + \frac{t}{2}\right) \cdot \alpha}{L_0}$$

Where L_0 is the length of the MEBA, h_f is the finger thickness of the, and α is the rotation of the joint.

Finally, the maximum total stress to be sustained is given by:

$$\begin{aligned}\sigma_{tot} &= \sigma_{max,f} + Y\left(\varepsilon_{f,max} + \varepsilon_t\right) \\ &= \frac{M_{max} \cdot 6}{b} \cdot \frac{1}{t^2} + \mathrm{Y} \cdot \left(\frac{t}{2\left(l_\rho + \frac{t}{2}\right)} + \frac{\left(\frac{h_f}{2} + \frac{t}{2}\right) \cdot \alpha}{L_0} \right)\end{aligned}$$

(Eq. 15)

where Y is the Young modulus.

For substituting the numerical values we will focus on the second joint (PIP), because the MCP is in a position allowing more space for the actuator, so that it would not be a problem to increase dimension of the Elastomer to sustain an larger momentum, whereas the DIP joint has such a small torque that dimensioning is not critical.

Numerical values were extracted from different sources and methods, integrating:

- data of studies of researches, as in the case of the forces or average values of finger dimension
- data given directly by astronauts in interviews
- data experimentally measured and estimated

The maximum momentum to be sustained from the second joint was found to be:

$$M_{max} = 4.8\ 10^{-1}\ Nm$$

From the interviews to astronauts it was known that the most closed condition required is equivalent to holding a 5 cm diameter ball in one hand. It was estimated that this corresponds to a maximum rotation of 45 degrees and to a curvature radius of 2 cm (l_ρ).

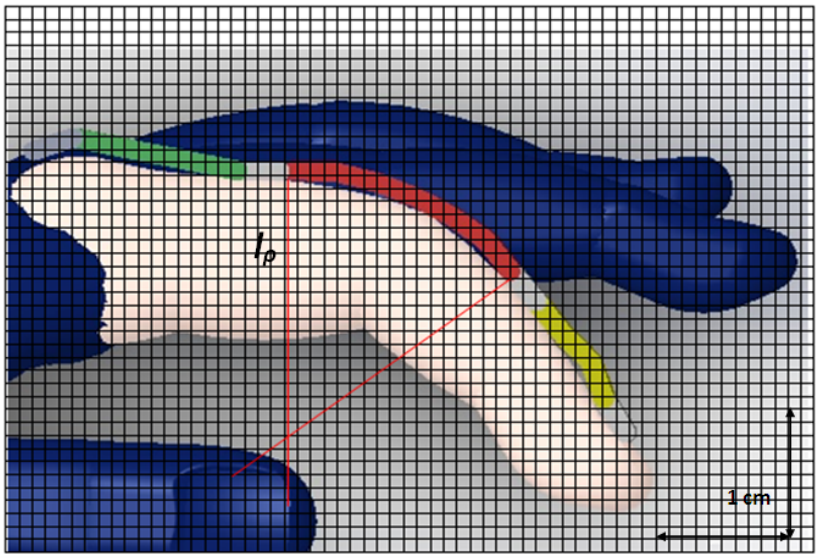

Figure 14 The figure reports the deformed configuration used to extract the geometric parameters needed for the dimensioning

The other data needed to compute the relationship between the stress σ_{tot} and the height of the material t are:

$$\boldsymbol{Y = 3\ MPa} \qquad \boldsymbol{h_f = 0.012\ m} \qquad \boldsymbol{L_0 = 0.020\ m}$$

$$\boldsymbol{l_\rho = 0.020\ m} \qquad \boldsymbol{\alpha = \frac{\pi}{4}\ rad}$$

(Eq. 15) describes the maximum stress in the top layer (the most stressed and strained) of the MEBA. σ_{tot} can be plotted as a function of total thickness (t) of the MEBA (Figure 15): the graph shows that, as the total thickness increases, the stress on the top layer decreases. Comparing this feature with the actuation stress applied by the dielectric elastomer, it is possible to determine the threshold thickness for the MEBA.

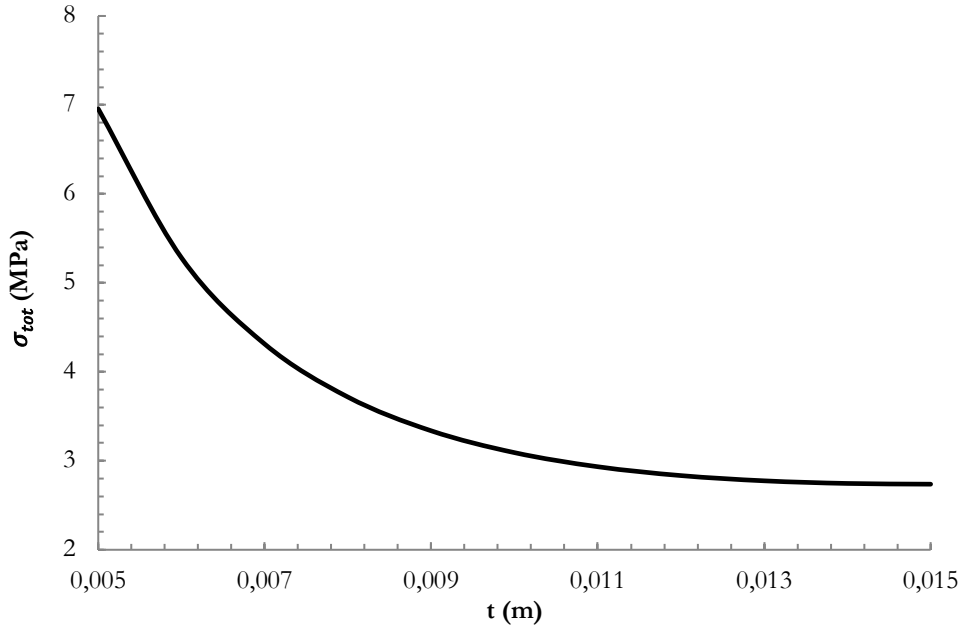

Figure 15 Dependence between maximum stress on the actuator and its height

Two considerations have to be drawn to motivate the hypothesis done.

First, the high flexibility of the material could induce to think that the momentum it has to sustain will cause too big deformation to the material itself, changing the contact point with the finger. This phenomenon is not due to happen because we plan to put a covering around the material, similarly to an internal glove (as depicted in the Figure 16), in order to prevent a radial deformation of the elastomer over a fixed value. In this way, we will be sure that the MEBA will transmit the forces as modelled.

Secondly, the contact between the Elastomer and the just explained covering will reduce the load on the most critical point of the material, increasing the safety factor.

Lastly, the most critical conditions for the external forces and for the bending contributions were summed. Nevertheless, they take part to two completely opposite situation, when the finger is completely stretched for the forces, and when the finger is completely closed for the bending. This is another reason why the forces we can apply are underestimated in these calculations.

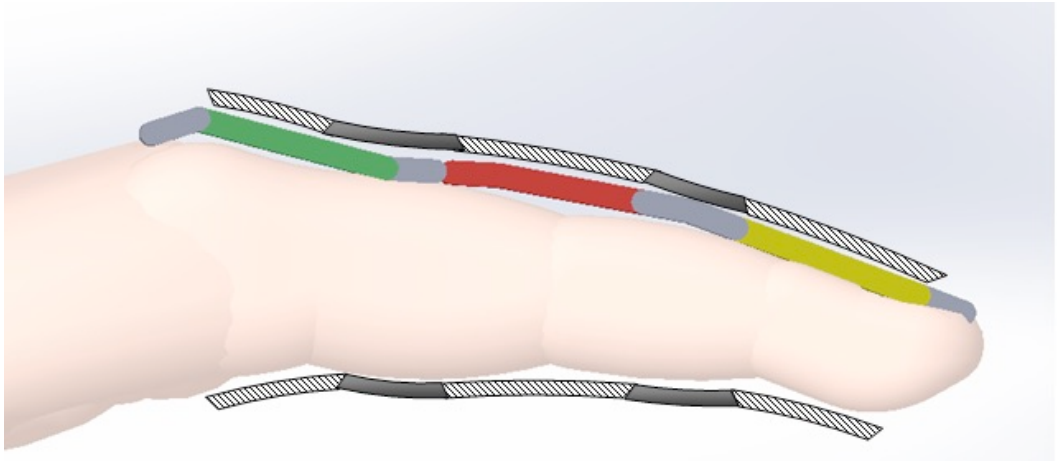

Figure 16 Representation of the external structure limiting to a maximum radial deformation the actuator

2.7.3 MEBA dimensioning

(Eq. 15) gives an indication of the major stress that the dielectric elastomer actuator is required to apply. Therefore, the values computed and reported in Figure 15 represent the threshold pressure that the material has to provide, as a function of the device's thickness. The next step is to compute the maximum pressure the DE is able to produce and to compare it to the requirements, in order to choose the minimum thickness needed for the device to work properly.

The worst loading conditions occur in the top layer of the MEBA, so, for the following evaluations, a small element of that layer is considered. The presence of loading constraints requires a proper evaluation and, even though the mathematical model previously presented is no longer valid, the initial assumptions on the material are the same: we consider the DE to be incompressible, homogeneous, isotropic, with a linear elastic mechanical behaviour.

The element taken into account (Figure 17) is prestrained in the z-direction. This way, no further deformation along z can occur and $z_0 = const$. The Maxwell pressure, due to the application of the voltage V, is applied along y and the actuation stress is directed along x.

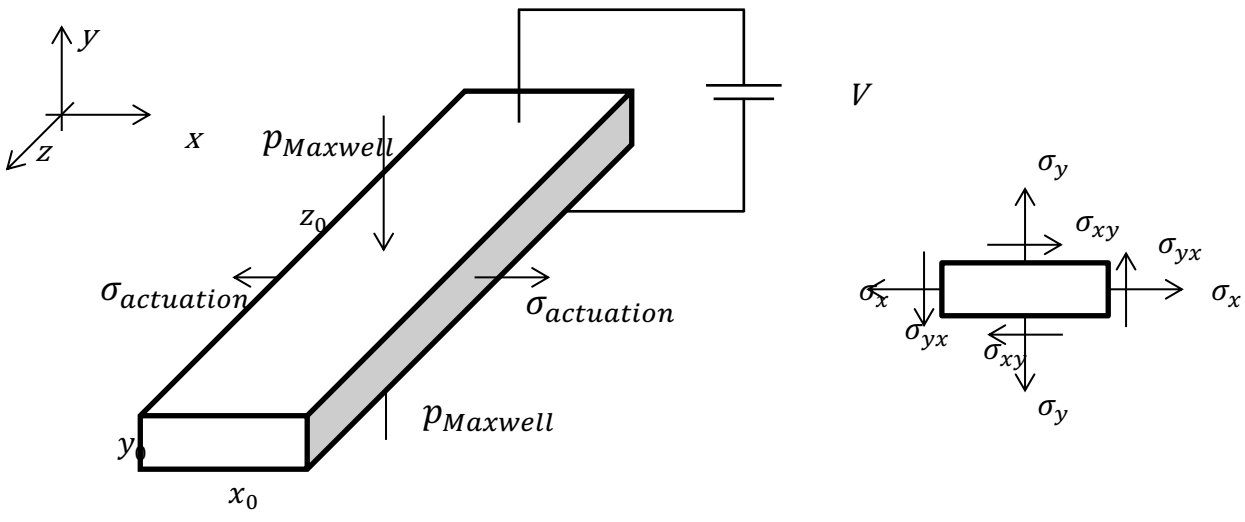

Figure 17 Dielectric elastomer element

The loading state and the geometry of the element lead to a *plane strain* in each *x-y* section and it can be assumed that all the cross sections, along *z*, are in the same condition [33], [34]. Taking one of those sections, the state of stress is described by the Hooke's law in the form of:

$$\begin{bmatrix}\varepsilon_x\\ \varepsilon_y\\ \varepsilon_z\end{bmatrix} = \frac{1}{Y}\cdot\begin{bmatrix}1 & -\nu & -\nu\\ -\nu & 1 & -\nu\\ -\nu & -\nu & 1\end{bmatrix}\cdot\begin{bmatrix}\sigma_x\\ \sigma_y\\ \sigma_z\end{bmatrix}$$

(Eq. 16)

Where Y is the Young modulus and ν is the Poisson's ratio.

The plane strain condition imposes $\varepsilon_z = 0$ and, therefore, it is possible to write:

$$\sigma_z = \nu(\sigma_x + \sigma_y)$$

$$\varepsilon_x = \frac{1}{Y}\left[(1-\nu^2)\sigma_x - \nu(1+\nu)\sigma_y\right]$$

$$\varepsilon_y = \frac{1}{Y}\left[(1-\nu^2)\sigma_y - \nu(1+\nu)\sigma_x\right]$$

(Eq. 17)

Moreover, no shear stress is present along *x* and *y*, therefore $\sigma_{xy} = 0$, as well as $\varepsilon_{xy} = 0$.

To evaluate the maximum actuation stress the material can apply along *x*, a dummy constraint is placed so that the deformation in the *x*-direction is imposed to be zero, $\varepsilon_x = 0$. Consequentely, it is possible to write a direct relation between the stresses in the *y* and *x* directions:

$$\sigma_x = \frac{\nu(1+\nu)}{(1-\nu^2)}\cdot\sigma_y$$

Substituting σ_x and σ_y with $\sigma_{actuation}$ and $p_{Maxwell}$:

$$\sigma_{actuation} = \frac{\nu(1+\nu)}{(1-\nu^2)}\cdot p_{Maxwell}$$

(Eq. 18)

For elastomeric materials the Poisson's ratio is $\nu \cong 0{,}50$. It results, recalling (Eq. 8), that:

$$\sigma_{actuation} \cong p_{Maxwell} = \varepsilon_r \cdot \varepsilon_0 \cdot \left(\frac{V}{h}\right)^2$$

(Eq. 19)

where ε_r is the material relative dielectric constant, ε_0 is the vacuum dielectric constant, V is the applied voltage and h is the thickness of the DE layer.

Eventually, it is possible to express the actuation stress the material is able to exert as a function of both layer thickness and voltage applied. Superimposing the resulting curves to the plot of Figure 15, it is possible to identify the working point of the actuator, dimensioning both thickness and voltage to apply.

To perform those evaluations, the Acrylic Dielectric Elastomer (3M VHB 4910) has been chosen because it is the best performing alternative. The properties of the material are presented in Table 7.

Table 7 Properties of Acrylic Dielectric Elastomer (3M VHB 4910)

Prestrain	**Energy density**	**Maximum actuation pressure**	**Young's modulus**	**Breakdown electric field**	**Dielectric constant**	**Efficiency**	**Reference**
(x%, y%)	**MJ/m^3**	**Mpa**	**MPa**	**MV/m**		**%**	
(300, 300)	3,4	7,2	3,0	412	4,8	80	[23]

It is important to point out that the maximum actuation pressure (7,2 MPa) has been computed by means of the Maxwell relation (Eq. 7), applying the breakdown electric field. Therefore, this value represents the superior limit to the actuation stress that the material is able to provide, regardless the device's geometry.

The MEBA designed for the PIP joint is made of $N=8$ layers. Thus the thickness of each layer is $h = t/8$, where t is the total thickness of the MEBA, and the actuation strain (Eq. 19) becomes:

$$\sigma_{actuation} = \varepsilon_r \cdot \varepsilon_0 \cdot \left(\frac{V}{t/8}\right)^2$$

(Eq. 20)

In Figure 18the actuation stress, provided by the Acrylic Dielectric Elastomer on the top layer of the MEBA with different voltages, is superimposed to the total stress required on the PIP joint, as computed thanks to (Eq. 15).

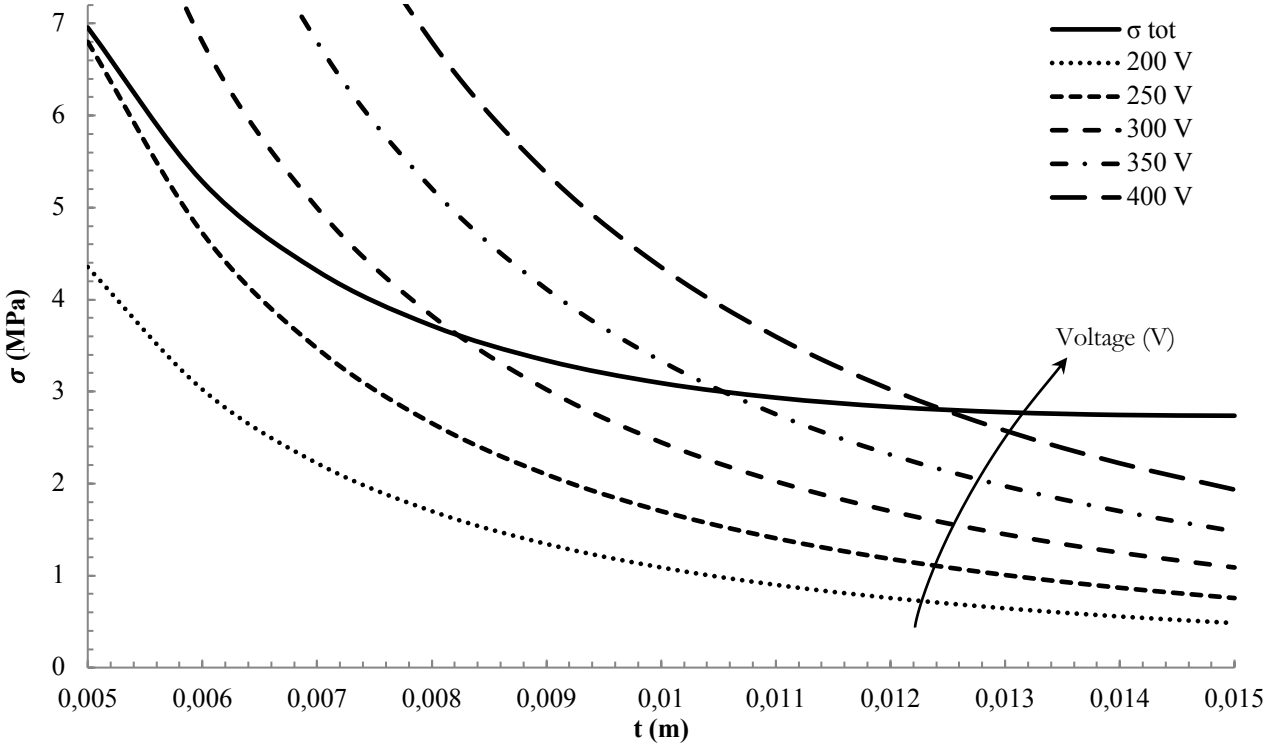

Figure 18 Superposition of the actuation stresses provided by DEs at different voltages and the total stress required

The intersections between the full line and the dotted lines identify the maximum MEBA thickness for each voltage. In order to provide enough pressure,

the top layer of the MEBA needs at least the application of $300\ V$. With that bias, the maximum thickness of the actuator can be $t = 0{,}008\ m$ and, for the single layer, $h = 0{,}001\ m$. Since the other layers of the MEBA are less stressed, they need a lower voltage to guarantee the proper working of the device.

According to the previous calculations and considerations, the Acrylic Dielectric Elastomer MEBA proved to satisfy the actuation requirements for the PIP joint of the index fingers. With some changes in the geometry it is possible to realize the actuators for the other joints and, eventually, a complete, light and compliant actuation for the fingers movement can be realized.

2.8 Actuator coaxial design

In order to endow fabrics with actuating functions, fiber-shaped actuators may be particularly effective. At the end of the 1990s, conducting polymer fiber actuators was presented [35] obtaining a fiber-like structure that showed strains of about 0,3% and active stresses around 3 MPa, with driving voltages lower than 1 V. However, the deformation of a conducting polymer was strongly anisotropic, with a deformation along the radial size that made the fibers not suitable in a real use-case scenario.

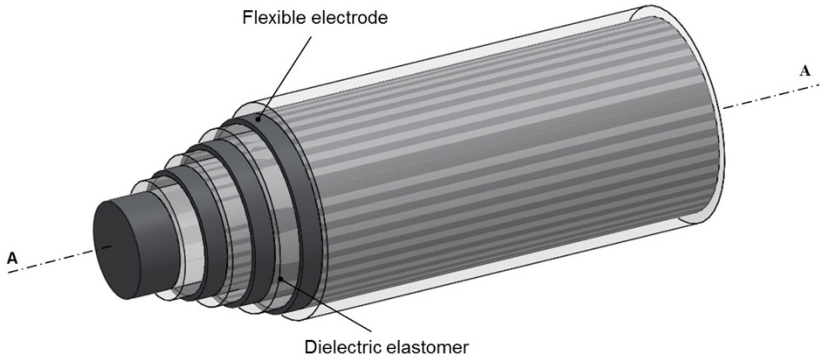

Figure 19 Dielectric elastomer coaxial design

Figure 19 shows the solution here proposed. This solution exploits the advantages of the multilayer geometry previously described, “rolling” it into a coaxial configuration. A coaxial structure allows the design of a fiber-shaped

actuator that can be endowed within a fabric. As mentioned above, different voltage levels are applied to different EAP layers, obtaining a fine control of the final deformation along the axial direction. Furthermore, the coaxial solution leads to an improvement of efficiency in terms of energy stored, with respect to the planar geometry. From an energy storage point of view, the EAP planar configuration can be approximated to a parallel-plate capacitor, whose capacitance is:

$$C = \varepsilon \frac{S}{d}$$

(Eq. 21)

where ε is the dielectric constant of the polymer, S is the surface area of the plates and d is the distance between them. Therefore, the energy stored (W) is

$$W = \frac{1}{2} C V^2 = \varepsilon \frac{S}{2d} V^2$$

(Eq. 22)

As described in (Eq. 22), the energy stored is directly proportional to the surface area (S) and to the square of the applied voltage (V). Moreover, it is inversely proportional to the plates distance (d), that in the specific case of the EAP layer is the thickness (t) of the dielectric elastomer.

Given those preliminary considerations, the coaxial design leads to relevant benefits in terms of energy storage efficiency and force generated. This come straightforward from a simple geometric consideration: given a fixed volume, a multilayer planar geometry has always a smaller surface area then a coaxial cylindrical one ($l^2 < \pi l^2$), as shown in Figure 20.

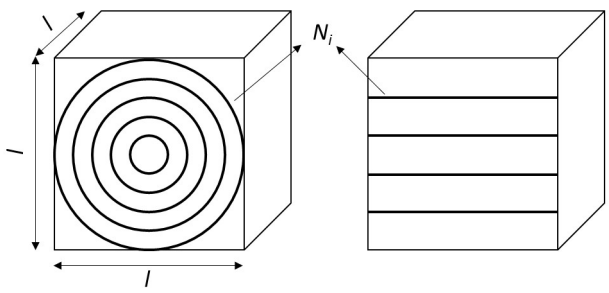

Figure 20 Comparison of coaxial and planar architecture

In the following, an analytical demonstration of this assumption is provided, comparing a multilayer planar architecture and a coaxial cylindrical architecture. Figure 21 shows the final actuation result of a single EAP coaxial fiber.

$$S_{i,p} = l_i^2$$

$$S_{i,c} = \pi d_i \cdot l$$

where d is the diameter of the cylinder, $S_{i,p}$ and $S_{i,c}$ are the *i-th* surface areas of a plane and a cylinder, respectively. Considering an equal number of planar layers (N) and coaxial cylinders inscribed within a cube with the same volume, the sum of surface areas $S_{N,p}$ and $S_{N,c}$ are respectively:

$$S_{N,p} = l_i^2 \cdot N$$

$$d_i = l - (i - l) \cdot \frac{l}{N}$$

$$S_{N,c} = \sum_{i=1}^{N} \pi l^2 \left[1 - \frac{i-1}{N}\right]$$

By solving the series $S_{N,c}$, the intial assumption is demonstrated as follows:

$$S_{N,p} < S_{N,c}$$

$$l^2 N < \pi l^2 \left[N - \frac{N-1}{N}\right]$$

where the inequation is always respected for $N > 1$. The result is a resizing of the device and an increase of the force generated.

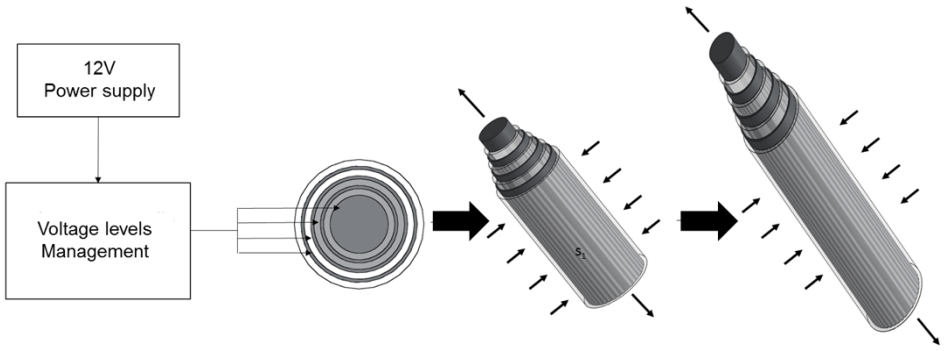

Figure 21 EAP coaxial fiber activation with different voltages applied on each layer

Considering the coaxial principle and investigating into the skeletal muscle architecture, the hierarchical structure of muscle fibers can be approximated to a bundle of EAP coaxial fibers that are able to generate a movement in response to an electrical stimulus. Figure 22 compares the muscle structure with a multi-fibers coaxial EAP architecture. Taking into account the possibility to individually activate each EAP fiber, applying different voltages, the muscle hierarchical selective recruitment principle can be mimicked. This allows to obtain the following advantages:

- to have a fine control of the force produced;
- to control the direction of the resulting deformation;
- to further reduce the voltages required for the actuation.

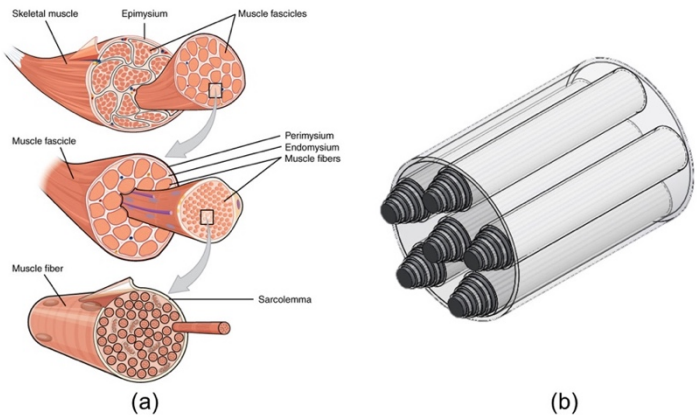

Figure 22 (a) Muscle hierarchical structure (b) Multi-fibers coaxial EAP architecture

2.8.1 Proof of Concept of the working principle

Electroactive Polymers need high voltages to be activated, typically in the order of *3–5kV*. The use of passive components such as resistors and capacitors has been suggested as a method for simple and inexpensive coupling of electrical and mechanical response of the actuator [36]. The aim of the control circuit specifically designed is to test the possibility of controlling the polymer actuator layer at different voltages with an AVR microcontroller. This circuit makes use of a DC to DC converter, providing an output voltage in the range 100V to 3kV with an input of 1–12V range and a maximum output power of 1,5W.

The test of the electronic circuit was performed using a single EAP layer (thickness of $100\mu m$) based on 3M VHB acrylic material and monitoring its behaviour. Initially, the VHB sheet was pre-stretched (300% deformation along the two axes) with a squared pantograph structure (Figure 23) and attached to a rigid frame.

Figure 23 Squared pantograph structure

Then, thanks to the adhesive present on both sides of the VHB sheet, the flexible electrodes were made by depositing a dispersion of micro particles of

graphite (Sigma-Aldrich, average particle size $< 20\mu m$) on both sides. Finally, two copper connectors were attached with carbon grease to the flexible electrodes in order to allow the electrical connection to the control circuit. Figure 24 shows the EAP proof of concept that is able to change the diameter size of *1 mm/kV*. The system was tested with different voltages adjusted with a digital potentiometer and voltage dividers. The DC-DC high voltage converter showed a linear input-output characteristic; however, the material does not change its shape with an applied voltage lower than 1 kV. Another monitored parameter was the relaxation time that resulted around 100 ms and was mainly due to the elastic recovery of the material.

(a) (b)

Figure 24 EAP proof of concept

The production of a multilayer proof of concept was not possible with the available facilities and resources. In fact, the production process of a multilayer configuration has a high degree of complexity and needs a fine control of different parameters, such as the homogeneous thickness of all the layers, a proper mechanical compliance among the electrodes and the dielectric layers and an effective electric connection with the control circuit. Different attempts failed to produce stable prototypes. One of the major issue was the occurrence of short circuits where the dielectric material had any defect or in correspondence with the connections with the external control circuit.

Eventually, it emerged the need of designing and producing a dedicated manufacturing setting and facilities, that required resources that were not available. For this reason, it was not possible to bring to completion to realization of a complete proof of concept for the solution conceived.

2.9 Conclusions and further activities

In this chapter, a new concept of EAP geometry inspired by the muscle architecture and a proof of concept of the working principle of dielectric elastomers based EAPs has been presented. A deep analysis of a EAP multilayer configuration (well known in the scientific community) in combination with the application of different voltages on each layer is expected to lead to relevant improvements within the soft actuators technology. A fine control of the deformation and lower voltage applied are the major improvement with respect to the literature. Since an excessive increase in the number of layers may cause a stiffening of the actuator, the coaxial geometry provides a good solution to this issue. In fact, a performance improvement can be obtained by increasing the total surface area of the flexible electrodes without affecting the mechanical properties of the material. Furthermore, a coaxial structure allows to develop active fibers, that can be partially woven within a fill the gap of wearable man-machine interfaces. This solution was patented and brought to a further level of innovation taking inspiration from the anatomy of natural muscles. In principle, a multi-fibers coaxial configuration would allow further improvements of the EAP performance introducing the control of each fiber within a bundle. In fact, the selective activation of the fibers can be leveraged to control and change the strength and movement of the whole bundle, mimicking the behaviour of natural muscle fibers.

Despite those promising improvements, there are several challenges to overcome from a material, electronic and integration point of view. Firstly, the material selection and improvement need to focus on dielectric elastomers with lower anisotropy values and lower dielectric constant in order to increase the electrostatic effect. This would bring, together with a reduction of the layers' thickness, to reducing the required driving voltages. Besides, with a lower driving voltage, the overall size of the electronic circuit can be reduced.

Another issue is the material-circuit interface through metallic plates. Actually, the wiring of the flexible electrodes with the electronic circuit is fragile and peak effects, generated by the metallic plates, can pierce the elastomeric layer, leading to a failure of the actuator. Carbon grease improves the connection of the plates, however is not perfectly stable. Finally, another challenge regards the manufacturing process, with particular reference to the coaxial configuration. Techniques used to develop and produce optical fibers, mainly based on co-extrusion process, have been identified as viable options.

Despite these and other challenges (e.g. improvement of the device reliability and efficiency), the integration within a fabric of a EAP-based actuator and electronic and power functions represent a high potential enabler to develop completely compliant wearable electronic textiles. Figure 25 depicts graphically the technological jump required to move from well-known traditional actuator devices to the EAP technology. Currently, EAPs are in the area of technology discontinuity, having lower competitive advantages and performances with respect to commercial products, but with a promising growth and potential to fill the technological gap.

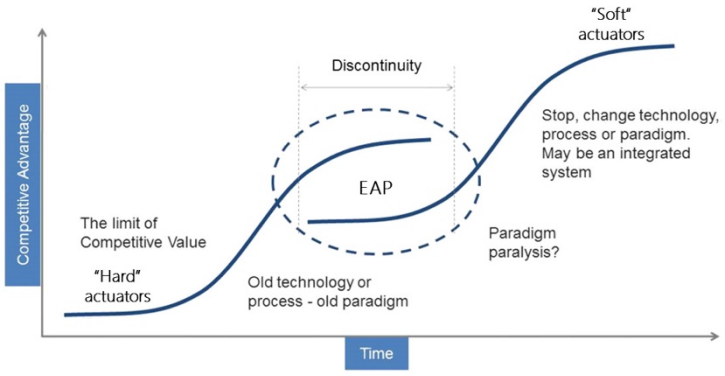

Figure 25 EAP technology trend compared to traditional "hard" actuators

Further development of the manufacturing process of the EAP fibers with the optimization solutions presented in this chapter may lead to fill the existing gap between mechanical actuators and the human body.

Chapter 3

Magnesium foams

3.1 Introduction

Aiming at the synergic integration of implanted biomaterials with the host organism, a design framework results crucial: biomimicry. It is straightforward to get inspiration from structures and solutions occurring in Nature in order to design devices intended to operate in symbiosis with a living organism.

Within such outlook, the context of orthopaedic surgery sets the morphology of natural bone as reference. Designing choices regarding materials selection, production methods and treatments (in bulk and/or on surface) are addressed to reproduce the mechanical and functional features of natural bone. In fact, if on one side the orthopaedic implant is required not to collapse under the mechanical load applied, on the other it should not bear excessively or exclusively the forces acting on the bone in order not to induce a *stress-shielding* effect. This phenomenon, in fact, may be critical since it reduces considerably the stimulation of regenerative bone cells and, ultimately, slows down the recovery of natural bone [37]-[40]. Given the previous considerations, the most important mechanical characteristics of natural bones are reported in Table 8 [3], [4], [41]-[43].

Table 8 Typical characteristics of human bones

Average bone density	1 – 2 g/cm^3
Young's Modulus of cortical bone	3 – 23 GPa
Young's Modulus of cancellous bone	0,01 – 1,57 GPa
Yield strength of cortical bone	105 – 180 MPa
Ultimate tensile strength of cancellous bone	1,5 – 38 MPa

The natural bone has a complex structure, resulting from millions of years of evolution, which fulfils several functions: it provides specific structural support, locally adapted to load conditions; it does not add unnecessary weight by means of an optimized minimization of mass and it allows nutrients supply to tissues through adequate vascularization. Such multi-functionality is enabled by the peculiar structure of the spongy bone tissue. [44]

Starting from these observations, the mimesis of cancellous bone conformation is one of the most appropriate guideline in choosing and designing materials for orthopaedic applications.

3.2 Magnesium foams as viable biomedical material

Among the feasible technological solutions, metallic foams with open interconnected porosity have been identified as the most promising choice [3]-[5], [41], [45] and the work of this thesis is focused on this solution. In fact, these materials can be designed to combine the mechanical properties and the morphological characteristics of natural bone, as well as the vascularization function and the stimulation of bone tissue growth. Furthermore, metallic foams represent one of the most suitable option to coherently develop a biomimetic device that reproduces the main features of natural bone.

In the light of the requirements outlined so far, pure magnesium represents an optimal solution. This metallic material in fact meets the multi-functionality requirement previously described: it has mechanical properties of the same order of magnitude as those of natural bone tissue (Table 9), it can be produced in the form of foam, it is biocompatible and bioresorbable. This last feature enables the possibility to avoid second surgery usually needed to remove orthopaedic devices once their function is fulfilled. Supporting this choice, there is a wide scientific literature [3], [4], [46]-[54] which, in recent years, has recognized magnesium as a

very promising material for biomedical applications, although there are still some critical aspects to be solved. In fact, the process of corrosion of magnesium in the body fluids results in the formation of gaseous hydrogen that, if produced too rapidly, can be harmful for the human body [4].

The shift from bulk magnesium to magnesium foam generally leads to a reduction of the mechanical performance (in terms of Young's modulus and compressive strength) which is directly dependent on the size distribution and the percentage of porosity [55]. Data relating to magnesium foams that can be found in scientific literature are, however, in line with the mechanical characteristics of cancellous bone [3], [4], [42]. Thus, magnesium foams fulfil the mechanical requirements identified for orthopaedic applications.

Table 9 Mechanical characteristics of pure magnesium

Bulk magnesium density	1,74 – 2 g/cm3
Young's Modulus of bulk magnesium	41 – 45 GPa
Young's Modulus of porous magnesium	0,8 – 1,8 GPa
Yield strength of bulk magnesium	65 – 100 MPa
Yield strength of porous magnesium	12 – 17 MPa

Given the fact that the final mechanical performance of the implant has a relevant dependency from the foam morphology, it is of major importance to carefully select the manufacturing process of the metallic foam itself. In the following a review of the state of the art of the current foam manufacturing processes is presented, together with a selection of the most suitable ones.

3.3 Magnesium foam manufacturing process selection

The first step in the assessment of the viability of magnesium foams as biomedical materials was the identification of the most appropriate manufacturing process, i.e. that allows the production of magnesium foams with open and interconnected porosity and, at the same time, enables a control on pore size distribution and porosity percentage.

Nowadays a relatively large number of methods for the production of metal foams has been proposed and developed. In fact, metallic scaffold can be produced both with conventional technologies or advance manufacturing techniques [56].

However, only some of these processes have emerged from research laboratories and are currently used on industrial scale for the production of commercial products [45], [57]. In the following an overview of the state-of-the-art of the processes for the production of metallic foams is presented.

3.3.1 Melt gas injection (air bubbling)

This process is based on the insufflation of a gas in the metallic bath for the creation of closed porosity. In order to keep the gas within the molten metal before the foam is solidified, it is necessary to increase its viscosity by non-soluble or slowly soluble ceramic particles in the bath. This way the foam can be stabilized. This process is used successfully for the production of aluminium foams and the foaming agents that can be used are air, CO_2, oxygen, inert gases and, sometimes, also water. The foam topology is controlled by adjusting the gas blowing process and the cooling rate of the foam. [58], [59] Below a diagram of the process is presented (Figure 26).

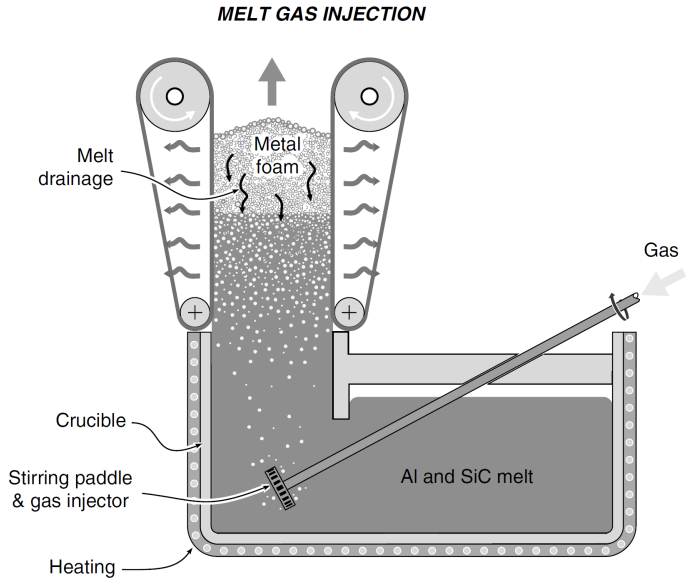

Figure 26 Metal gas injection (air bubbling) [57]

3.3.2 Gas-releasing particle decomposition in the melt

This process uses Titanium Hydride (TiH_2) as a foaming agent which, at the temperature of 465°C, decomposes in metallic Ti and gaseous H_2. In particular, TiH_2 particles are added to the vigorously agitated metallic bath and the formation

of gaseous hydrogen bubbles gives rise to closed porosities in the solidified metal. Also in this case, it is necessary to increase the viscosity of the metallic bath (using calcium particles that are rapidly oxidized in CaO and, in the case of Al alloys, in $CaAl_2O_4$) to prevent the gas from escaping before the foam is stabilized by the solidification of the alloy. [57], [60] The process is outlined below (Figure 27).

Aluminium alloys foams are produced with this technology since the hydrogen, that partially dissolves in the metallic bath, may lead to embrittlement phenomena in many alloys and because its decay rate is too high in the case of alloys with a higher melting point.

Tane et al. [61] produced porous magnesium with unidirectional cylindrical pores using this technique. In particular, they used MgH_2 powders as a foaming agent, leveraging the decomposition in metallic Mg and gaseous H_2, and driving the solidification process along one direction. This process resulted in the creation of unidirectional elongated pores.

3.3.3 Gas-releasing particle decomposition in semi-solids

This technique can be considered a powder metallurgy process. In fact, in this case the foaming agent particles (again TiH_2) are mixed with the metallic powders and then compacted. The "green" is then extruded to obtain precursor bars. The latter are inserted in a closed mould and, by heating just above the metal/alloy solidus temperature, a hydride decomposition and a partial melting of the alloy are obtained [62], [63]. In this process, the metallic material swells (due to the pressure of the H_2 bubbles resulting from the decomposition of the TiH_2) filling the mould. It is then possible to get components with the desired geometry (that of the mould used) with a near net shape process. Further, this process allows the production of sandwich structures in which a metal foam layer is enclosed between two compact layers. The process diagram is presented in Figure 28.

This process has been used also to produce iron foams starting from a ceramic foam precursor. The iron oxide foam precursor was obtained using foaming agent particles mixed with ceramic particles exploiting the hydrogen release. Afterwards the ceramic precursor was reduced in a controlled atmosphere to obtain the final iron foam. [64]

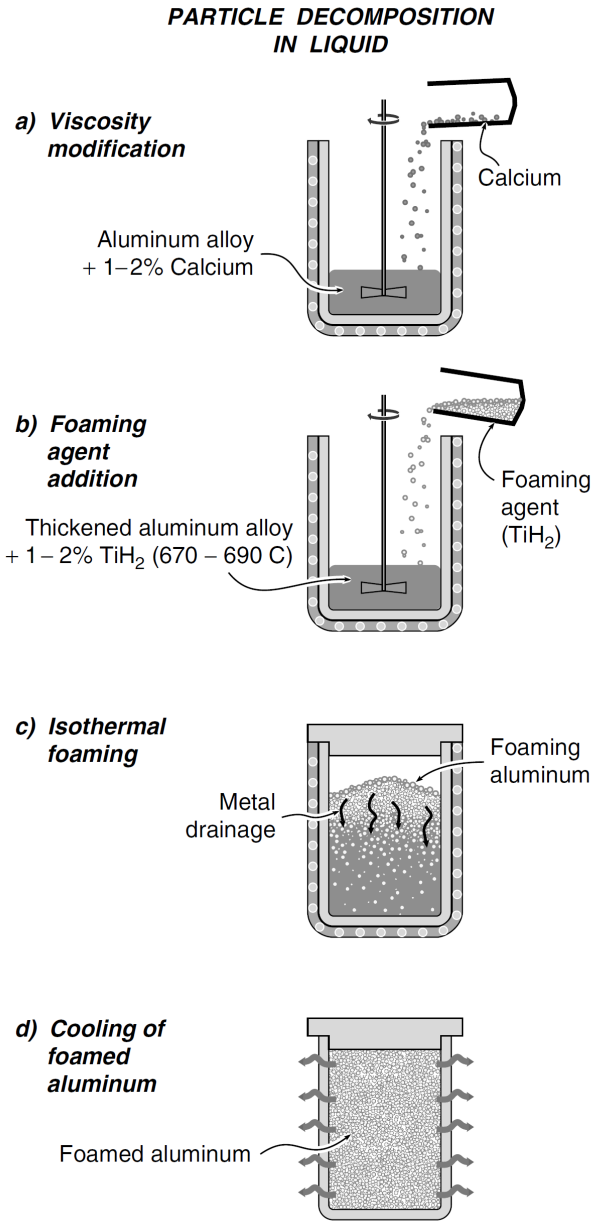

Figure 27 Gas-releasing particle decomposition in the melt [57]

3.3.4 Casting using a polymer or wax precursor as template

This technique is a kind of lost-wax casting that uses as a preform a polymeric foam selected in accordance with the characteristics of the metallic foam that is required (morphology and dimensional distribution of porosity).

The polymeric foam is placed in an open mould and infiltrated with a ceramic slurry that fills all the porosities. By heating the mould, the polymer is pyrolyzed and the ceramic green is densified: the result of this operation is a ceramic preform that reproduces the negative of the starting polymer foam. The metallic alloy is then casted into the ceramic preform. Once solidification occurs, the ceramic preform is removed by mechanical stress.

As an alternative to the molten alloy, a slurry of metal powders can be used instead, with a following sintering [65]. This method is very versatile and can be used with all metals and foundry alloys. The process scheme is presented in Figure 29.

3.3.5 Metal deposition on cellular preforms

This production process is based on the Chemical Vapour Deposition (CVD) technique, applied using a polymeric foam as a substrate. It is thus possible to deposit a metallic layer on the surface of the pores of the polymer. The polymer is subsequently removed by localized heating. The result is a metallic foam in which the connecting structures between the pores are internally grooved: through a sintering process it is finally possible to obtain densification. [45], [66]

This method has limited applications because of the technological difficulties in controlling process parameters and since it can be used to deposit only pure metals. Figure 30 illustrates the steps of this production technique.

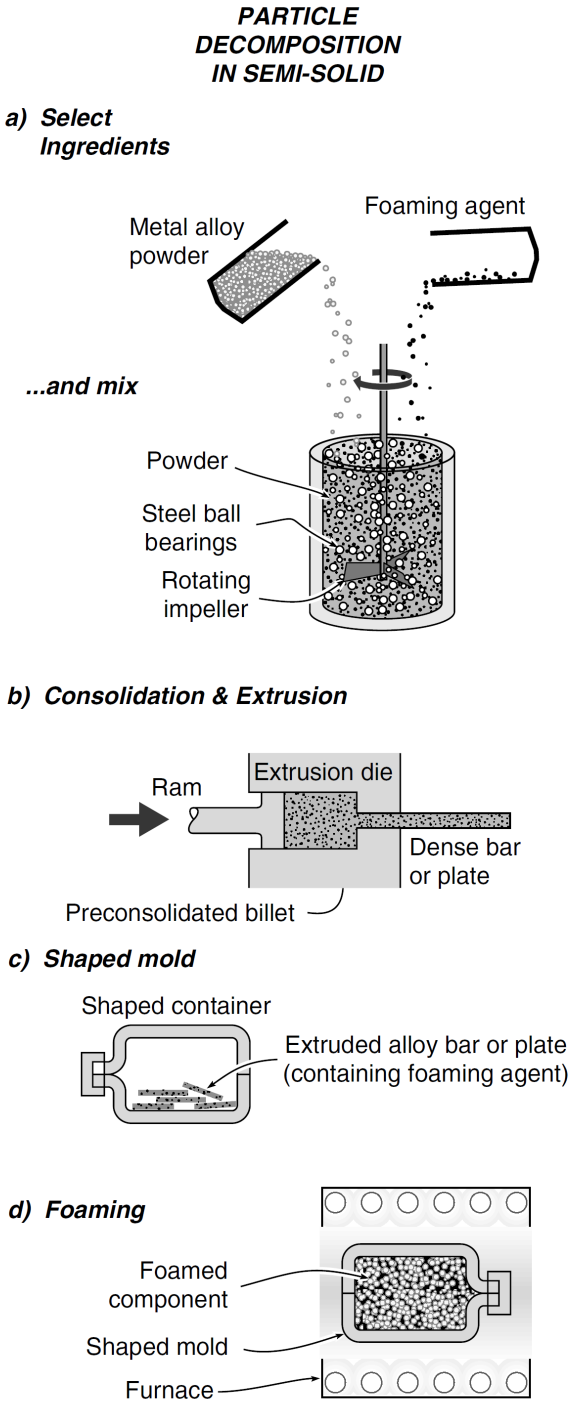

Figure 28 Gas-releasing particle decomposition in semi-solids [57]

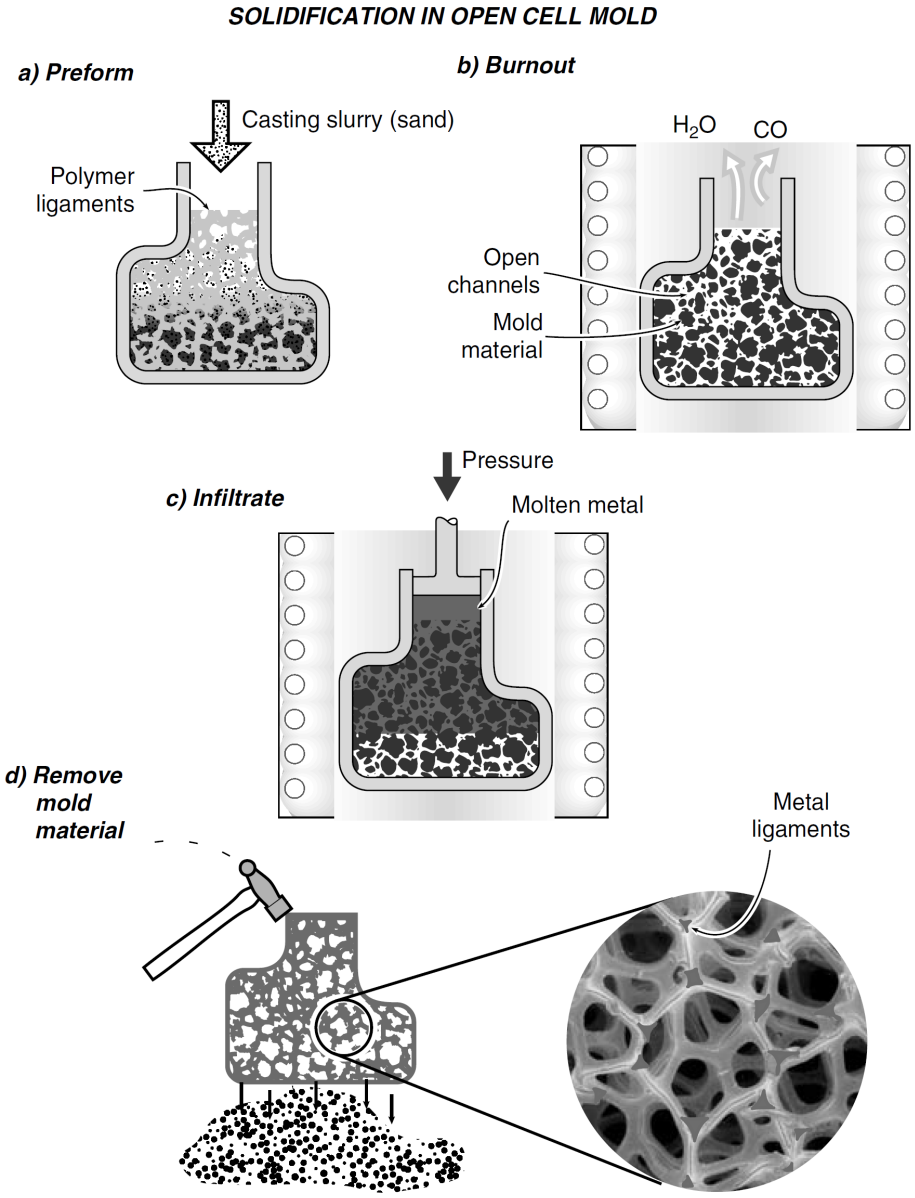

Figure 29 Casting using a polymer or wax precursor as template [57]

3.3.6 Entrapped gas expansion

This process belongs to the family of the powder metallurgy technologies and exploits the low solubility of the Argon in metallic alloys. In fact, the production method involves introducing the metallic powders into a closed metal container

inside which the vacuum is applied and, subsequently, Argon is introduced. The heating of this system causes the sintering of the metal powders and the increase of the gas pressure: the latter therefore expands, and, thanks to creep phenomena, it is able to create porosity within the alloy. [67]

A following cold rolling process (preferably biaxial) allows to obtain panels with a sandwich structure, characterized by a spongy core and a dense surface. After lamination, a thermal treatment is necessary to homogenize the dimensional distribution of the pores and increase their average size. The numerous thermal treatments required make the process (Figure 31) expensive.

3.3.7 Hollow sphere structures

With this production method, sponge structures are obtained starting from internally cave metallic spheres. To obtain a component with the desired geometry, these balls are compacted in a mould and sintered by *Hot Isostatic Pressing* (HIP) or by liquid-phase sintering. In the latter case, without the occurrence of high pressures, the porosity maintains a regular spherical structure. [68], [69]

The production of the metallic balls is a key aspect of the process. These can be made from a slurry containing a precursor hydride (e.g. TiH_2) which, by decomposing at high temperature, generates the internal cavity. The peculiarity of this process lies in the fact that it allows the production of metal foams with both open and closed pores. The process diagram is presented in Figure 32.

3.3.8 Space holder method

This metallic foam manufacturing process is based on mixing metal powders with a proper space holder material (generally organic) that are mixed and compacted so to obtain a green body. The green body is thermally treated at low temperature to remove the space holder material and promote initial neck formation among metal particles. Finally, a sintering process allows a complete densification of the metallic structure and the achievement of the final mechanical properties of the metallic foam [45], [70]. This method was experimentally validated by Wen et al. [71], [72] who produced titanium and magnesium high porosity foams with mechanical properties comparable with those of human bones.

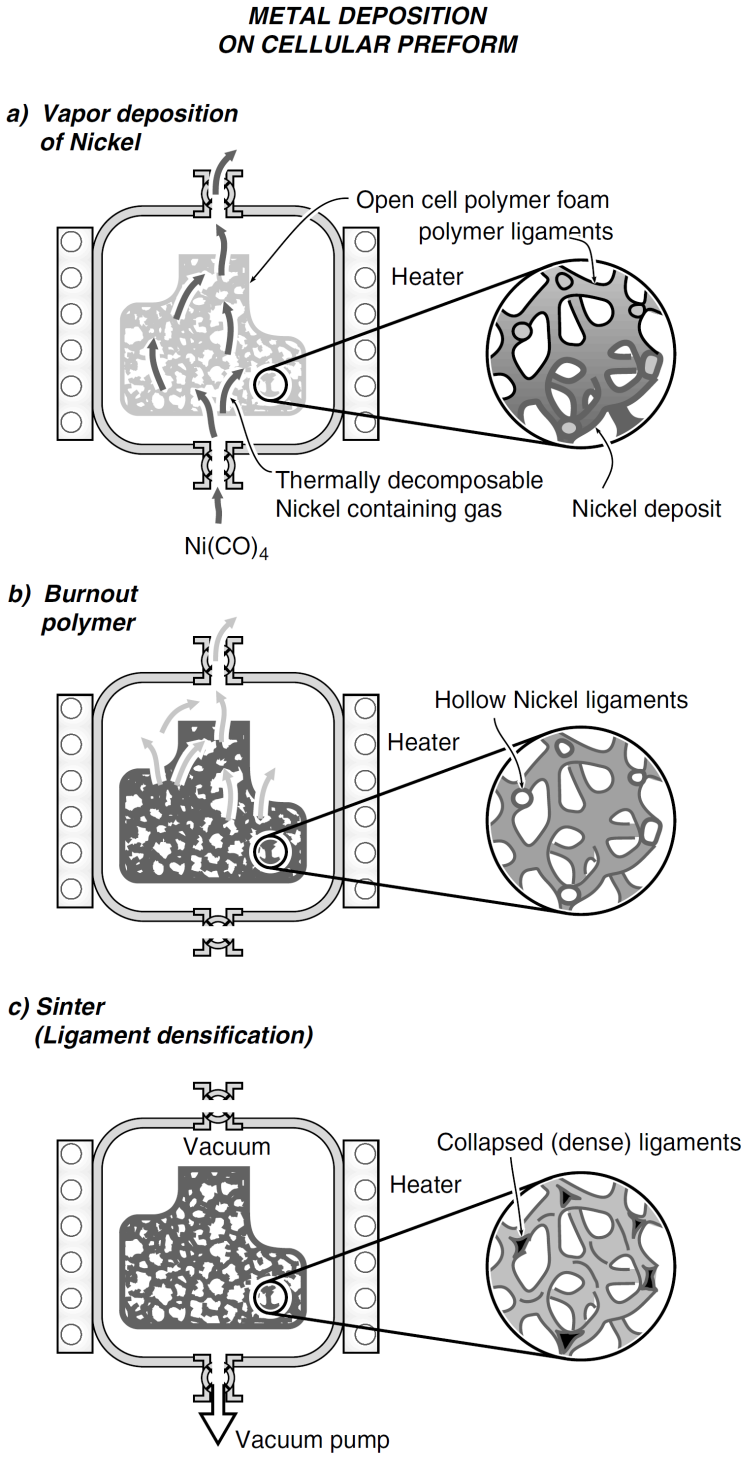

Figure 30 Metal deposition on cellular preforms [57]

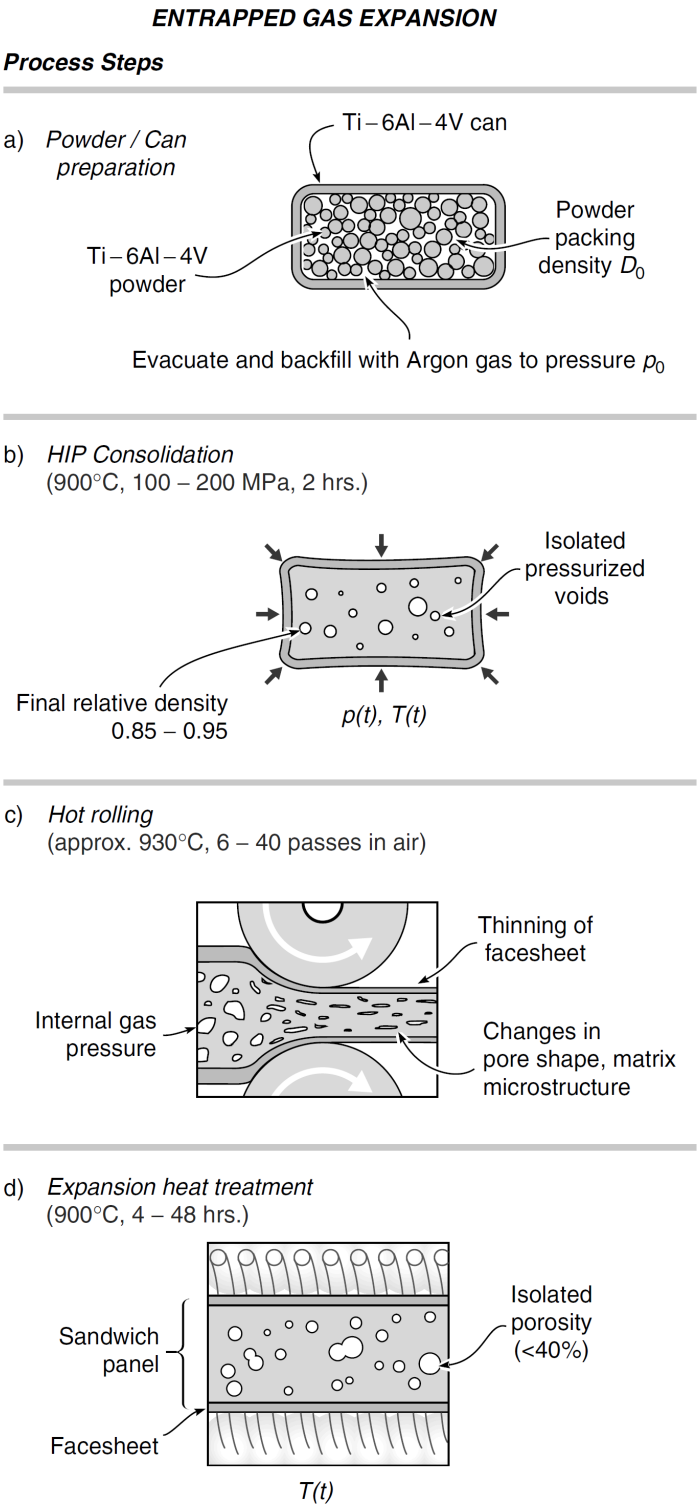

Figure 31 Entrapped gas expansion [57]

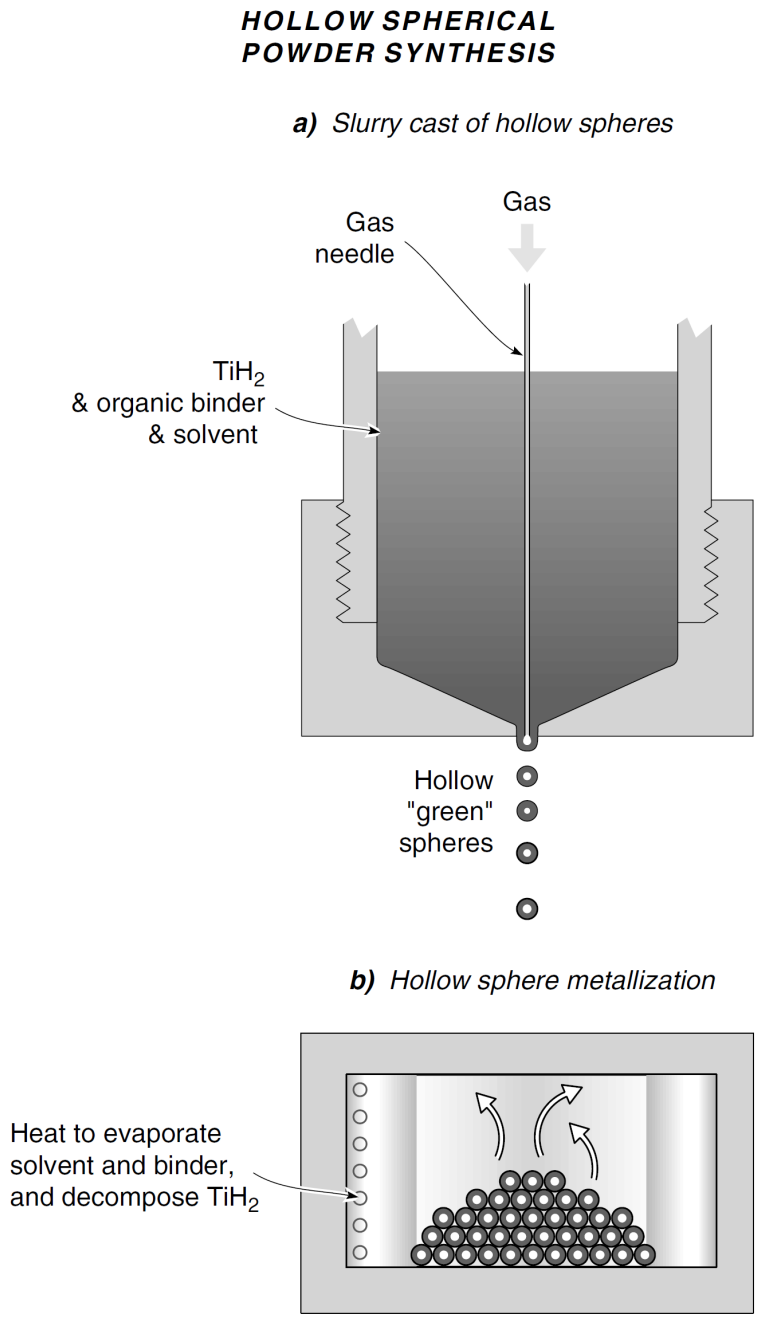

Figure 32 Hollow sphere structures [57]

3.3.9 Co-compaction of two materials, one leachable

In this process, two powders of different materials (generally a metallic one and a ceramic one) are mixed and compacted to obtain a co-continuous interconnected structure of both phases. Once densification occurs, one of the phases (e.g. NaCl) is removed by a suitable solvent. It is also possible to infiltrate a bed of dissolvable particles within the molten metal bath and, after solidification, remove them by solvent, leaving open pores in the final product (Figure 33).

This method was used by Osorio-Hernández et al. [73] to produce pure magnesium foams with open cell porosity. In particular, a porous preform of NaCl was obtained by cold pressing NaCl spherical particles, and it was then infiltrated with molten magnesium in controlled (argon) atmosphere. Finally, the NaCl particles were dissolved in a basic solution (NaOH + H_2O) to avoid the occurrence of pitting corrosion in the magnesium matrix. The sample obtained showed homogeneous porosity with open interconnected pores and had mechanical properties compatible with the requirements of metallic scaffolds.

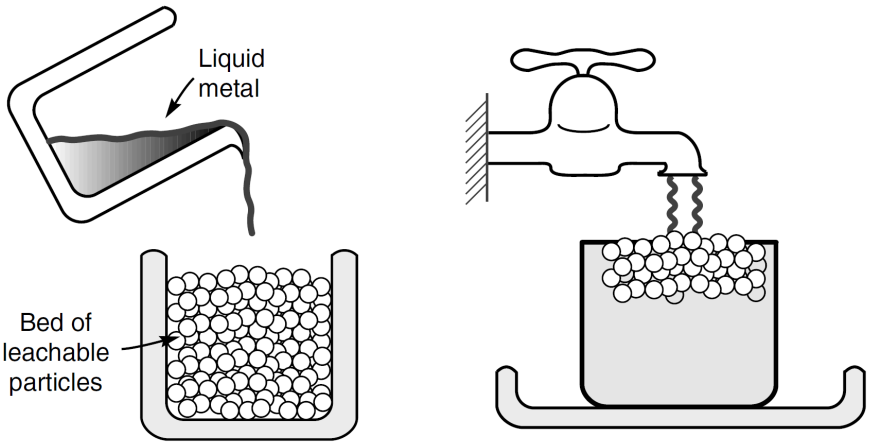

Figure 33 Co-compaction of two materials, one leachable [57]

3.3.9.1 Spark Plasma Sintering variant

This process variant is based on the *Spark Plasma Sintering* (SPS) technology [74]: metal powders are mixed with ceramic powders (eg NaCl), are introduced into a graphite die and current pulses are applied (in the order of kA). The application of these electric discharges causes very high and localized heating of the powders that leads to the densification of the component (melting of the hoppers), without altering the morphology of the starting particles. The sintered product obtained by this technique is characterized by a co-continuous structure of the two phases (metallic and ceramic) interconnected. Finally, it is possible to remove the ceramic phase by obtaining the desired metal foam.

The SPS process has several advantages: given the rapidity of the treatment, there is no increase in the size of crystalline grains and, consequently, the dimensional distribution of porosity is determined by the granulometry and by the amount of ceramic powders used.

3.3.10 Gas-metal eutectic solidification

This process allows to obtain a metal foam starting from a metal-hydrogen binary system with a eutectic composition: during cooling from the liquid state, these alloys solidify by releasing gaseous H_2. The preparation involves the saturation of the metallic bath with hydrogen under pressure, followed by a progressive cooling accompanied by a pressure reduction. The resulting structure, called GASAR, is characterized by porosity with a high degree of order. [75] The process is schematized in Figure 34.

a) Metal - Hydrogen binary phase diagram

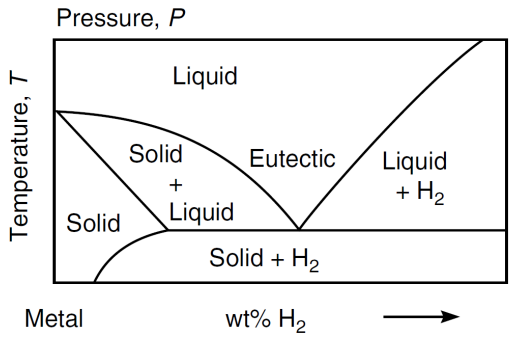

b) Directional solidification

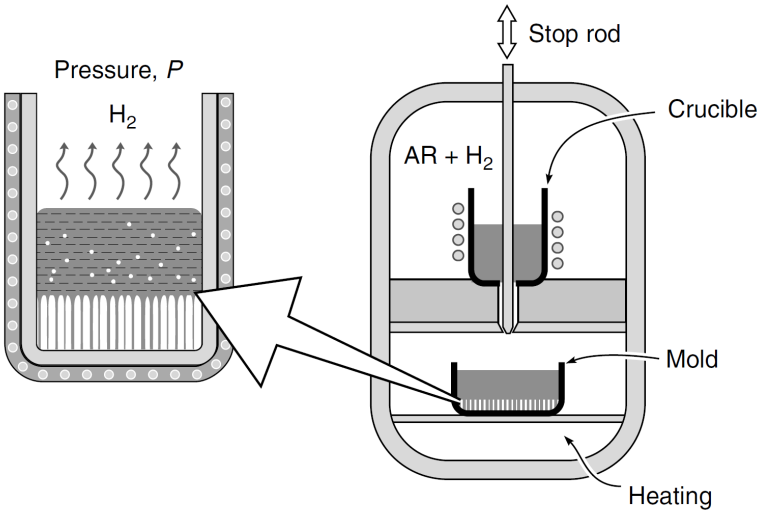

c) Final pore structure

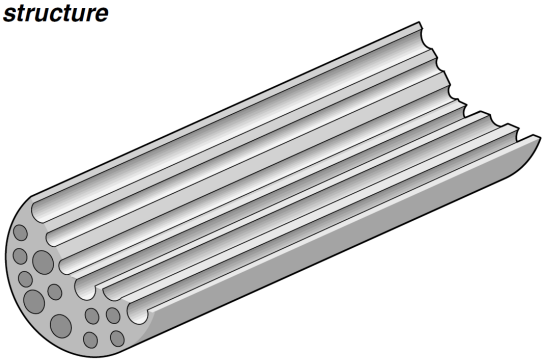

Figure 34 Gas-metal eutectic solidification [57]

3.3.11 Solid freeform processes

Solid freeform processes include a wide set of technologies that are united by the same working principle. In fact, in all the manufacturing processes belonging to this family, the shape of the final object is obtained with no need of a mould, a container or a preform. On the contrary, the final object is obtained by stacking thin layers of material, that are deposited or superimposed using different techniques. For this reason, they are also known as layer by layer production techniques.

The literature review highlighted that some layer by layer processes were successfully used to produce metallic objects, starting from metallic powders dispersed in an organic medium. Due to the high reactivity of magnesium powders, were excluded from the analysis all the processes involving the metal fusion. The most suitable technologies identified are:

- Tape casting
- Micro-stereolithography (SLA) & Digital Light Processing (DLP)
- Fused Deposition Modelling (FDM)

3.3.11.1 Tape casting

Tape casting was successfully used to produce functionally graded materials by stacking and laminating monolithic layers obtained from different mixtures of copper and magnesium powders, with a composition ranging from 100% Cu to 100% Mg [76], [77]. The sintering of the multi-layered green is done by hot pressing in controlled atmosphere.

3.3.11.2 SLA & DLP

Micro-stereolithography (SLA) was used to produce 3D microstructures starting from several photo curable suspensions containing metallic powders. In particular, in this process each layer is hardened by curing a photopolymer, that is present in the suspension, using a focused UV laser beam. This allows the production of a wide variety of morphologies and microstructures.

SLA has been successfully used to produce 3D structures containing micrometric copper powders (3 μm diameter) [78], tungsten carbide (WC) powders or cobalt (Co) powders [79]. In all the cases, the SLA was used to produce a green bodies the underwent a subsequent sintering process in order to remove the organic components and increase the final density of the sample. The critical aspects of this

technology concern the nature of the metallic powders, as well as their granulometry, since a good light scattering within the suspension must be ensured to enable the photo curing reaction. Furthermore, the stability of the suspension and its viscosity must be optimized, as well [78], [79].

A point in favour of this technology is represented by the fact that biocompatible and biodegradable resins have been developed and tested [80], [81]. Those results open the possibility to conceive a composite material, characterized by a polymeric matrix reinforced with magnesium powders, that is completely biodegradable.

3.3.11.3 FDM

The Fused Deposition Modelling is one of the most common and widespread layer by layer technology, especially applied for rapid prototyping. It is based on the use of a thermoplastic polymeric filament that is locally molten, deposited and that solidifies by cooling. Such polymeric filament can be filled with ceramic or metallic powders in order to produce complex shape objects with a composite material. By means of a subsequent thermal treatment (e.g. sintering), the polymeric matrix can be removed and this results in a complex shape ceramic or metallic object.

The literature review highlighted the use of this technology with iron and copper powders (diameter up to 45 μm), with a polymeric matrices of ABS or Nylon [82]-[84].

3.3.12 Process selection

As shown from the previous review, the foam morphology that can be obtained is very variable, depending on the method used: it is in fact possible to produce structures with open and interconnected porosity or with closed pores. Pore size as well as pore size distribution can be tailored, and high porosity levels can be reached. Regular structures, with oriented porosity in one or more directions, can be produced as well introducing a specific anisotropy in the component, or by means of computer aided design (CAD) technologies. Table 10 summarizes the main characteristics of the available technologies for the production of metallic foams [57], [71], [72].

Table 10 Comparison of available technologies for metallic foams production

	Foam relative density	**Pores size (mm)**	**Pores morphology**	**Notes**
Melt gas injection (air bubbling)	0,03 – 0,1	5 – 20	Closed-cell	Potential biocompatibility issues due to process additives [58], [59]
Gas-releasing particle decomposition in the melt	0,2 – 0,07	0,5 – 5	Closed-cell (partially open-cell after lamination)	Potential biocompatibility issues due to process additives [57], [60]
Gas-releasing particle decomposition in semi-solids	> 0,08	1 – 5	Closed-cell	[62], [63]
Casting using a polymer or wax precursor as template	> 0,05	1 – 5	Open-cell	[65]
Metal deposition on cellular preforms	0,02 – 0,05	0,1 – 0,3	Open-cell	Very expensive Lowest relative density available [45], [66]
Entrapped gas expansion	0,5	0,01 – 0,3	Closed-cell	[67]
Hollow sphere structures	> 0,05	0,1 - 5	Mixed open and closed-cell	[68], [69]
Space holder method	0,22 – 0,5	0,1 – 0,24	Open-cell	Successfully used for Ti and Mg foams [71], [72]
Co-compaction or casting of two materials, one leachable	0,3 – 0,5	0,01 – 10	Open-cell	Very wide range in pores size [73]
Gas-metal eutectic solidification	0,7	0,03 – 0,2	Open-cell	Highly ordered pores [75]

Given the requirements previously identified, the technologies which give closed-cell pores morphology are excluded from the viable metallic foam production processes. After the first screening, the candidate technologies are:

- Solid freeform process: Tape casting
- Co-compaction or casting of two materials, one leachable
- Casting using a polymer or wax precursor as template
- Metal deposition on cellular preforms
- Gas-metal eutectic solidification

Among these processes the first one has been selected as the most suitable process for the application intended in this study since it allows the production of metallic foams with complex morphology. In particular, the layer by layer approach can be used to obtain structures that mimics the hierarchical structure of natural bones. In fact, the final 3D geometry to be obtained can be sliced into 2D layers with different profiles and reproduced by cutting each layer, i.e. each tape. Afterwards the cut tapes can be sandwiched with the proper positioning to fully reproduce the starting 3D geometry. This way is possible to mimic the macroscopic trabecular structure of bones. At the same time, the constituent material of each tape has an inner porosity, given by the manufacturing process itself, that brings to a microscopic porosity of each trabecula of the overall structure.

The co-compaction or casting of two materials, one leachable process (in the SPS variant) is also a viable alternative and it is used in the present work to evaluate the possibility to monitor the porosity morphology *in situ*, during the sintering process itself.

3.4 Proof of Concept: Tape casting

3.4.1 Introduction

Tape casting technology for the production of metallic and ceramic films can be dated back to the 1940s. Before, this technology was well known and widely used in other sectors such as paper, painting (to test the covering power of paint formulations) and plastics industries [85]. Glenn Howatt patented this technique to produce thin ceramic sheets with controlled thickness [86], forming ceramic materials into flat plates, especially useful in the electric and radio fields. Tape casting consists of the preparation of a suspension containing a mix of ceramic powders and organics components (dispersant, binder and plasticizer) in a proper

solvent, which is spread or "cast" on a flat moving support. After the casting phase, solvents slowly evaporate and the so-called "green ceramic tape" is obtained in the form of a thin and flexible sheet. The thickness for green tapes usually goes from 5 microns to some millimetres [87].

Tape casting can be used not only for the production of ceramic sheets but also to metals, adopting proper modifications.

Slip casting is probably the most similar processing method to tape casting because the starting conditions are the same, but it involves the use of both ceramic or metallic powders. However, they mainly differ in the drying conditions: slip casting uses a porous mould to absorb the water vehicle while in tape casting a plastic carrier film is used, and the drying occurs by solvent evaporation from the surface. Moreover, in tape casting the use of nonorganic solvents is very common to allow a fast-drying process. The literature reports that, for his first applications, Howatt used a porous plaster to use water as liquid media. Then in the 1950s, the American Lava Corporation introduced the use of a plastic carrier or "non-absorptive moving polymer carrier" which enabled the mass production and also a more convenient storage of the green tape that could be rolled.

Figure 35 shows the basic apparatus used for tape casting; it is constituted by:

- a reservoir where the slurry is placed before the casting phase;
- a doctor blade which is the most important component; the term "doctor" indicates a scraping blade able to remove the excess of substance from the moving surface that is being coated [87].

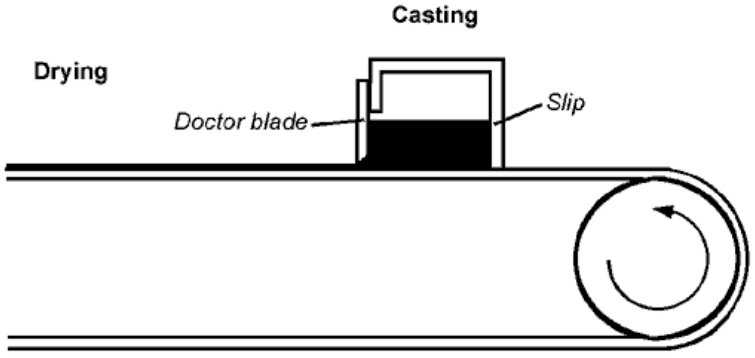

Figure 35 Basic scheme of a typical tape casting system

The doctor blade is the moving part of the slurry reservoir which, once opened, allows the slurry to be cast on a moving carrier polymeric film. It also regulates the amount of the slip by removing the excess of suspension during the process. The thickness of the tape is controlled by selecting:

- the doctor blade opening gap;
- the chemical composition of the slip;
- the carrier material

The casting rate is constant and controlled to obtain a uniform film.

Manifold parameters mast be taken into account during the tape casting process: the slurry formulation, the rheological properties of the slip, the doctor blade gap, the speed of the carrier, the reservoir depth, the shape of the doctor blade and the drying chamber (that is strongly dependent on the type of solvents used in the formulation). All those factors greatly influence the properties of the resultant green tape.

Tape casting is one of the most suitable methods to obtain large, thin and flat ceramic layers with a low variation of density along the casting direction and a homogeneous pore distribution (if present). It can be used for the production of multilayer structures with similar layers or alternating layers with different chemical composition. A significant advantage of tape casting is its cost-effective application both for industrial and laboratory testing techniques.

Tape casting shows a linear relation between the slurry, the green tape and the sintered product: the homogeneity and the stability of the slurry determine the properties of the green body such as the packing of the particles. Moreover, they have an influence on the sintering process and, ultimately, on the characteristics of the final products [88].

Clegg et al. [89] originally reported the processing and characterization of SiC/C multilayer mainly regarding mechanical properties: SiC powder with an addition of 0,4 %wt B was firstly mixed, pressed into a 2-mm-thick-sheet and then rolled into flat sheets (about 200 μm in 38 thickness). After cutting, these thin sheets were coated with graphite, stacked and pressed to form a 2 mm thick plate. After debinding and sintering treatments, a SiC/C multilayer was obtained, and its relative density was measured around 98%. The main difference between a monolithic and laminated material is in the load/deflection behaviour: the former behaved in a

linear elastic trend until catastrophic failure. On the other hand, the laminate deformed with a linear elastic fashion until the crack reached the same stress intensity as the monolithic SiC, and then the cracks deflected along the SiC-C interface. Therefore, the apparent toughness increased from 3,6 to 15 MPa*$m^{1/2}$, and the work of fracture increased from 28 to 4625 J/m^2.

3.4.2 Materials and processing

The different components which form the slurry have a high influence on the properties of both the green tape and the final sintered product. For this reason, it is necessary to study in detail all the aspects linked to each constituent. In the following sections, the materials selection process and the properties of each of them will be discussed.

3.4.2.1 Powders

In any fabrication process based on powders, the most important element is the starting powder because it essentially influences the final product properties. In fact, after the removal of the organic components and the densification process, the powders are the only element of the batch that remains and they will define the performance of the product [85]. The criteria for the selection of the powders mainly depend on the requirements of the specific application and the manufacturing technique. Particularly in the case of tape casting, it is necessary a complete characterization of the powders in order to tune a proper chemical formulation.

The most important criteria to be considered are chemical purity, particle size, distribution and shape, surface area, density, agglomeration/segregation degree, homogeneity in composition, sintering activity, ability to be mass-produced, compatibility with other slip components and costs of production. In fact, the optimization of the slurry formulation and its preparation is necessary to avoid inhomogeneity and segregation and, moreover, to promote the packing of the particles in the following phases. The presence of impurities can inhibit and modify the sintering mechanism: for this reason, it is important to know and eventually check the level of impurities present in the starting powder. The effect of particle size and distribution have been widely discussed in the literature [90], [91]. The tape casting process takes advantage of gravity and shrinkage of organic components during the drying phase to generate a packed system. Therefore, to obtain the highest possible bulk density of the green, the selection and control of the particle size and distribution is fundamental.

McGeary [92] reported a detailed theoretical study on the packaging of the powders: he predicted a maximum packaging of 74 %vol, for mono-size particles with ideal sphere shape with no Van der Waals interaction between particles. The arrangement has to be octahedral or tetrahedral, with a coordination number of 12. For coordination number of 10, 8 and 6 theoretical calculation of the packing densities lead to 69,8 %vol, 60,5 %vol and 52,4 %vol respectively. Experimental calculations indicate a packaging around 58 to 65 %vol when the coordination number is 8. For liquid suspensions, a good approximation for packing density values is established around 40-45 %vol with particles of approximated 1 μm of diameter [93].

Shanefield [94] showed that in commercial powders with a standard particle size distribution, the best packing factor correspond to about the 55% of the theoretical one. This relatively low value is due to the fact that, in most of the cases, the powder processing method favours the production of very fine particles without taking into account that to a finer powder corresponds a higher surface energy and, thus, a higher driving force during the sintering process.

The surface area is another crucial parameter because it gives an indication of the best interaction factor among components in order to have a good dispersion, lubrication or binding qualities. In fact, there is a direct relation between the total powders surface area and the amount of organics needed. Moreover, the selection of the proper dispersant/solvent combination, as well as the proper dispersant (and its concentration), are all critical factors for powders with a very high surface area [87]. In general powders with a high surface area, that means above 20 m2/g, are much harder to work with and the ideal range is between 5 and 15 m2/g.

Dispersion milling could be necessary also in order to homogenize the particle size of different powders used in a unique system. In general, this process can be carried out by ball milling (wet or dry), vibratory ball (wet and dry too), attrition milling in wet ultrasonic dispersion technique and ring gap mill.

The density of the powders is another important factor in powder selection. During tape casting process is also necessary to maintain a high quantity of particles in suspension and, depending on the particle weight, is possible to determine the particle size required for a specific formulation.

3.4.2.2 Solvents

Tape casting is a fluid forming process, and the component which lets the powders behave like a liquid and flow on a support is the solvent; this liquid element is also used to homogeneously distribute the other ingredients in the slurry producing a uniform mixture [95]. The solvent or mixture of solvents used to formulate the slurry composition have to:

- dissolve the organics components of the slurry such as binder and plasticizers;
- disperse the powders;
- provide a uniform distribution of all other components to obtain a homogeneous mixture of them;
- give to the suspension the desired rheological properties such as a suitable viscosity;
- provide a quick evaporation at moderate temperature (often the drying phase is conducted at room temperature);
- ensure a good consolidation of the tape.

Another factor that could influence the solvent selection is the production cost and its effects on health and its environmental impact. Some solvents such as Xylenes, MEK, toluene and benzene have been banned for industrial use in some Countries because of their carcinogenicity and also for their long-term effects on the human body.

All organics present in the slip need to be dissolved, for this reason, it is common to use a mixture of solvents to increase the ability to dissolve [96] and at the same time to control the drying rate, the costs and to improve safety. Some studies determined that when a mixture of two types of solvents (respectively classified as “kinetic solvents” and "thermodynamic solvents”) is used, it is possible to lower the amount of solvent. This is due to the combined effect of an efficient interaction and a faster evaporation. This is the case of the so-called azeotropes, introduced by Boch and Chartier in 1988: they are a mixture of solvents with the suitable feature to acts as one; they show an excellent solubility and the evaporation rate is quite fast.

Most of the tape casting slurries are prepared with nonaqueous solvents and, among them, the organic ones are the most used.

Water is recommended because is very cheap and it is one of the most environmentally friendly solvents. Nevertheless, it is not the most commonly used because of the difficulty in finding water-soluble binders and plasticizers. Additionally, adopting aqueous suspension formulation the casting speed increases and the evaporation rate (drying step) decreases: this affects the production cost because of a reduction in productivity.

The formulation of the slip starts with the selection of the powder because, as it was mentioned previously, it has a significant influence on the final product properties; after that, it is necessary to choose the binder(s) and then, the liquid to dissolve the selected binder(s).

The chosen solvents must not adversely affect the powders [87] and all the organic components present in the slip that have to be dissolved as well. For this reason, the investigation on the interactive force between the liquid media and the rest of the suspension components is required. Those forces can be classified based on the atomic origin: ionic forces, dipole/dipole forces, hydrogen bonding forces and Van Der Waals forces.

This kind of interactions can affect the performance of the solvents. Therefore, it is important to choose a liquid media characterized by a good compatibility with the binder. For example, they should have similar functional groups because their polarity has an effect on the way in which they interact [85].

3.4.2.3 Surfactants

The role of surfactants in tape casting processing is crucial. The literal meaning is SURFace ACTive AgeNT. They include different chemical aids like dispersants, deflocculants, wetting agents, flattening agents, flocculants and many others. In general, the surfactant is an additive which actively modifies the particles surface to give them the desired properties such as a surface charge, a surface energy or a specific chemical activity. In this case, the term surfactant is regarding the dispersant agent used to control the natural agglomeration of the powders within the slurry [87], so that its addition helps the dispersion of particles and hold them in a homogeneous suspension. The dispersant action can be performed by steric hindrance or ionic repulsion.

The natural tendency of powder to agglomerate is due to the attractive and repulsive forces acting on small particles which bring them together. These forces are the Van der Waals forces which are attractive: they are generated by the

interaction of atoms with permanent or induced electron/nucleus dipoles on the particles surface. On the other hand, the repulsive forces can have both electrostatic and steric nature. The first ones occur when the particles have the same the electric charge, so they repel each other. In those cases, it is common using polar solvents such as water-based slurries. The second ones are predominant in non-polar organic solvents, where the electrostatic forces are usually lower. The mechanism involves the separation of particles by putting a coating on one particle which physically avoids another particle coming into contact with it. Organic long chained macromolecules are often used in both aqueous and non-aqueous system to favour this mechanism.

Most of the dispersants used in solvent-based tape casting are of the steric hindrance type: the purpose is to obtain an electro-steric stabilization of the particle powders in the first step of the process. This mechanism can be briefly explained as follows: there are macromolecules formed by hydrocarbons with acid or basic head groups or of amphipathic copolymers which attach themselves to the particle surface while the rest of molecules are extended into the liquid medium [85]. These hydrocarbon chains form a network surrounding each particle and keep them separated from the others.

A secondary function of the dispersant is its deflocculant action: the agglomerates tend to trap air in powder interstitial spaces; if these particle groups are not broken the air could form bubbles in the green tape or even pores in the sintered material.

It is well-known that binder overlaps the surfactant effects; nevertheless, the use of a dispersant improves the working place for the binder that can act on each particle, just separated by the dispersant/deflocculant, instead of enveloping an agglomerate and makes it a particle group.

3.4.2.4 Binder

The binder supplies the network which holds the entire chemical system together during the casting process: when the solvents evaporate, the green tape forms a matrix with these organic components. Then when the powders are entrapped into the chains, they can produce a network leaving a residual porosity resultant from the drying process.

Being the only continuous phase in the green tape, the binder has a substantial effect on its properties such as flexibility, strength, plasticity, laminability, durability and smoothness [87].

Binder is one of the most important components in a slurry formulation and, ultimately, in the tape processing route. For this reason, it is necessary to identify all the parameters to select a proper casting binder such as solubility, viscosity, cost, strength, Tg or ability to modify Tg, firing atmosphere of the powder, ash residue, burnout temperature and others [85], [87].

There are many different binders widely used for slip formulation. They can be classified into two groups: polyvinyls (vinyl) and polyacrylates (acrylic). Both of them show a good film forming capability, but they differ in the burnoff/removal properties under different atmospheres. In general, there are long-chain polymers or precursors (monomers or emulsion particles) that become long-chain polymers during drying [85], [87].

There is a third group of binders, cellulose, which is less commonly used, especially in those formulations in which water is used as a solvent.

Vinyl

Vinyl binders include many compounds widely diffused and known both in consumer market and industries. Among them, polyvinyl chloride (PVC) is the most commercially known and it has applications in many different industries, such as fabrication of water and sewer pipes or lawn furniture. Besides, polyvinyl alcohol (PVA), used in food and textile industries, and polyvinyl butyral (PVB or Butvar), used in the textile industry and for the production of safety glass, are common in the slurry formulation, even more than PVC.

Depending on the gaseous atmosphere used in the furnace during the process, the vinyl can react. In an oxidizing atmosphere, the burn-out could be complete because these polymers burn at high temperature and require oxygen from the gaseous atmosphere. The residual carbon from this process interacts with oxygen to form CO and CO_2. Wet hydrogen, nitrogen and cracked ammonia atmospheres can also ensure a proper removal of the binder. In the presence of a non-oxidizing atmosphere, the decomposition of the binder releases carbon (ash) [85].

Acrylics

The main advantages in using acrylics binders are the cost effectiveness, the absence of ash residue in neutral or reducing atmospheres, the strength, the solubility, and the ability to modify T_g. Acrylics show a different decomposition mechanism respect to vinyl binders; in fact, they break down, unzip their chain and evaporate [87]. This mechanism is convenient in reducing or inert atmosphere with the formation of only a little amount of carbon residue. Polymethyl methacrylate and Polyethyl methacrylate give an outstanding strength to the green tape at low concentrations. Both Vinyl and Acrylics can be plasticized by several additives.

Cellulose

These polymers have been mostly used in water-based slurries because most of the cellulose polymers are water soluble. Some considerations must be taken into account in using these compounds. The first one is the thickening properties: since the cellulose requires more liquid medium providing a low solid loading slip that raises up the drying shrinkage, cracking and porosity of the tape. Another problem is related to the high quantity of air entrapped into the slurry that generates many bubbles during the casting, and a high porosity or flaws in the green tape [87].

3.4.2.5 Plasticizer

The last organic additive is the plasticizer, which has the role of ensuring flexibility and plasticity to the green tape. This means that it is possible to bend the tape without damage or crack it. Its working principle consists in increasing the binder(s) workability and flexibility [85].

The molecular weight of a plasticizer has to be around 300 and 400 with a boiling temperature of more than 200°C. Moreover, it has to show chemical and physical stability, low cost and no hazardous environmental impact. Furthermore, the plasticizer has to interact with the binder allowing the binder polymer chains to move inside the tape matrix without breaking the matrix itself.

Plasticizers are classified into two types depending on the mechanism that can provide flexibility and plasticity to green tape. The first one, “Type I” is a plasticizer that softens the polymer chains between particles allowing them to stretch; while plasticizers of the “Type II” can add plasticity (plastic deformation) to the green tape matrix [87].

The first class of plasticizer is a chemical which softens the polymer chains between particles allowing them to stretch more easily. They modify the glass transition temperature (T_g) by shortening the polymer chains and allowing a greater flexibility at a given temperature. Besides, the plasticizer can also dissolve the binder: the addition of a component such as phthalates can in fact partially dissolve it. The quantity of Type I plasticizers added to the slurry affects the properties of the resulting green tape: in fact, a significant amount leads to a higher elasticity of the tape. In this case, it is possible to stack the layers without using any adhesive material because the surface is particularly sticky. However, an excess of plasticizer may cause the adhesion of the polymer to the carrier surface [87].

The second class of plasticizer interposes between the polymer chains hindering the formation of molecular bonds between the chains and giving them higher mobility in the dry tape: the resultant effect is the lubrication of the matrix. Other capabilities of the Type II plasticizer are to avoid cracking problems during drying of the green tape, to reduce the yield stress and to increase strain to failure. Rheological parameters such as shear behaviour and shear viscosity are positively affected: in fact, the lubrication effect enhances the mobility within the slurry before drying, improving the motion of the fluid through the blade during the cast. Furthermore, the lubrication improves the release of the film from the casting support, because the bottom side of the tape results lubricated by the plasticizer. On the other hand, the abuse of a type II plasticizer may reduce the yield stress providing and easier deformation of the tape under its weight [87].

3.4.3 Experimental procedure

The goal of the experimental activities carried out was the study of the viability of successfully tape cast a magnesium-rich slurry. The analysis of the available literature revealed that very little research was conducted about using metallic magnesium powder in a Tape Casting process.

L. Peter Martin et al. [76], [77] exploited the Tape Casting technology in order to produce compositionally graded structures to be used as light-gas gun impactors. In particular, they produced a metallic graded structure with a composition ranging from 100% Mg to 100% Cu, using a stack of tape casted layers obtained starting from different slurries containing a variable mixture of Mg and Cu powders. This study was the starting point for the investigations presented in the following. The slurry composition was studied and optimized in order to maximize the metallic

powder content so to have a magnesium-rich green tape that, after sintering, will maintain suitable mechanical properties.

3.4.4 Slurry formulation and optimization

The slurry preparation was performed according to the following procedure. First of all, the solvent and the surfactant (dispersant) are manually mixed. After that Mg powders are added to the mixture under controlled atmosphere conditions. This caution is needed because magnesium powders are highly sensitive to oxidation and, if they are handled in air, they might explode. Furthermore, surface oxidation of the metallic powders is known to inhibit densification in the following thermal treatments [97]. The controlled atmosphere is ensured by mixing all the components inside a glove box in a Nitrogen atmosphere. Afterwards, this mixture is ball milled for 24 h in order to allow the uniform wetting of the metallic powders, the break-up of any particle agglomerate and the proper mixing of the components. Then, the binder and the plasticizer are added, and the mixture is ball milled for further 24 h. Finally, the slurry obtained is tape casted onto a Mylar support (PET film) with a blade gap of 1 mm and at a speed of 100 mm/min. The tape is subsequently dried at room temperature for 12 h. The detachment of the green tape from the Mylar support is performed by hand with no problem since no permanent adhesion occurs.

The components of the slurry formulation that was optimized are reported in Table 11. In particular, the magnesium powder (Goodfellow) used has a commercial purity of the 99,8% and a particle diameter around 50 μm (–325 mesh).

Table 11 Slurry components

Binder	Methyl methacrylate ethyl acrylate (Sigma-Aldrich, average M_w ~101,000)
Plasticizer	Dibutyl Phthalate
Solvent	Methyl ethyl ketone (MEK)
Dispersant	Hypermer KD-1
Metallic powder	Mg powder (99,8% purity)

A number of different formulations was produced and tape casted, following the process previously described. The adjustments in the composition were guided by the resulting tapes. The starting formulation is reported in Table 12. The slurry showed very poor slipping properties due to the high viscosity of the formulation,

as well as a partial mixing of the components and the presence of metallic powder agglomerates. The resulting tape (Figure 36a) was, consequently, totally not uniform and discontinuous.

Table 12 Slurry formulation n. 1

	%wt	**g**
Binder	9,65	5,79
Plasticizer	1,74	1,044
Solvent	30,1	18,06
Dispersant	0,62	0,372
Solid	57,9	34,74
Total	100	60

In order to improve the rheological characteristics and homogeneity of the slurry, the amount of solvent was progressively increased. Thus, six more formulations (Table 13) were prepared and casted.

Table 13 Summary of the slurry formulations (solvent increase)

Formulation n.	**1**	**2**	**3**	**4**	**5**	**6**	**7**
Solvent increase (%wt)	-	+ 10%	+ 20%	+ 25%	+ 50%	+ 75%	+ 100%
Binder (%wt)	9,65	9,37	9,10	8,97	8,39	7,87	7,42
Plasticizer (%wt)	1,74	1,69	1,64	1,62	1,51	1,42	1,34
Solvent (%wt)	30,1	32,14	34,07	34,99	39,24	42,97	46,27
Dispersant (%wt)	0,62	0,60	0,58	0,58	0,54	0,51	0,48
Metallic powder (%wt)	57,9	56,20	54,61	53,84	50,32	47,23	44,50
Total (%wt)	100	100	100	100	100	100	100

The resulting green tapes are shown in Figure 36. As previously mentioned, the starting formulation (n. 1) produced a very poor green tape. On one side, the increase of the solvent content was effective in improving the characteristics of the slurry and of the tape, but, on the other, an excessive amount of solvent gave rise to some irregularities in the tape. In particular, formulations n. 3 and n. 4 present a high number of bubbles on the surface. Those regions are characterized by a lower quantity of magnesium powder and were formed during the drying of the tape because of the excessive amount of solvent. Finally, the formulations n. 6 and n. 7 were too liquid, and it was not possible tape cast them successfully.

To better understand the morphology of the green tapes produced, some samples were cut and observed by means of a SEM (Scanning Electron Microscope). In particular, the formulations n. 2, n. 3 and n. 5 were analysed.

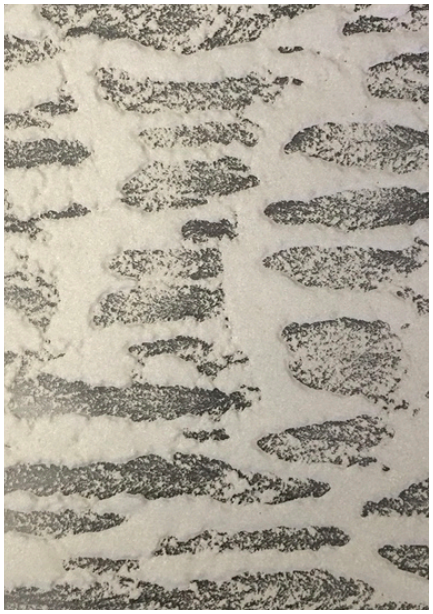

(a) Formulation n. 1

(b) Formulation n. 2

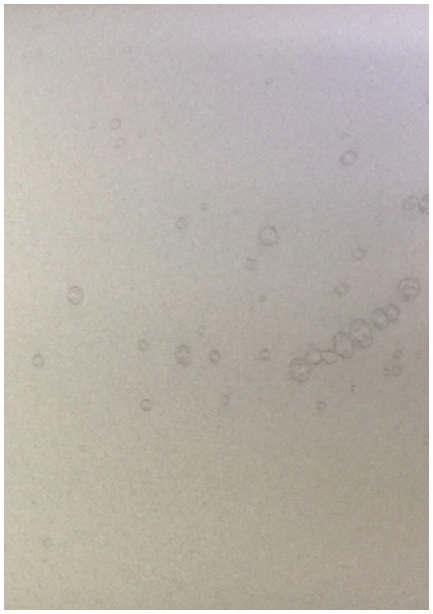

(c) Formulation n. 3

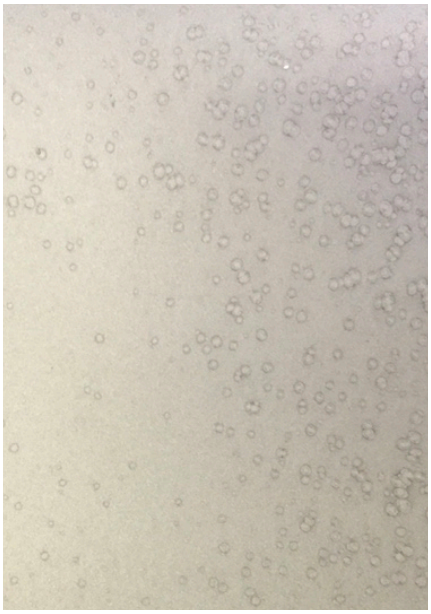

(d) Formulation n. 4

(e) Formulation n. 5

Figure 36 Green tapes obtained from the different formulations

The tape obtained from formulation n. 2 (Figure 37) shows a good overall homogeneity, with a uniform distribution of the metallic powders and of the binder. Furthermore, there is a good wetting of the solid particles by the plasticizer and the residual solvent after drying. The formulation n. 3 (Figure 38) produced a tape with similar characteristics, but the cross-section highlights a non-uniform distribution of particles in some regions of the tape, corresponding to the bubbles that can be observed in Figure 36c. Finally, the formulation n. 5 (Figure 39) shows a good distribution of the solid particles, but poor wetting of the system and a low amount of binder.

These observations led to the selection of the formulation n. 2 as the best alternative of this first step of optimization.

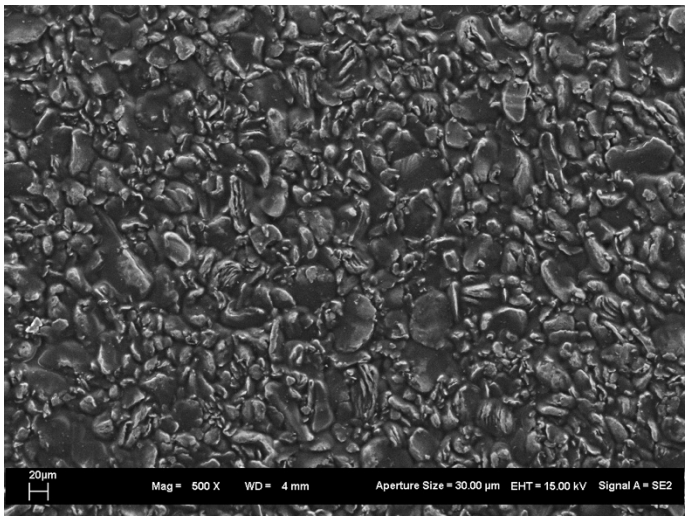

(a)

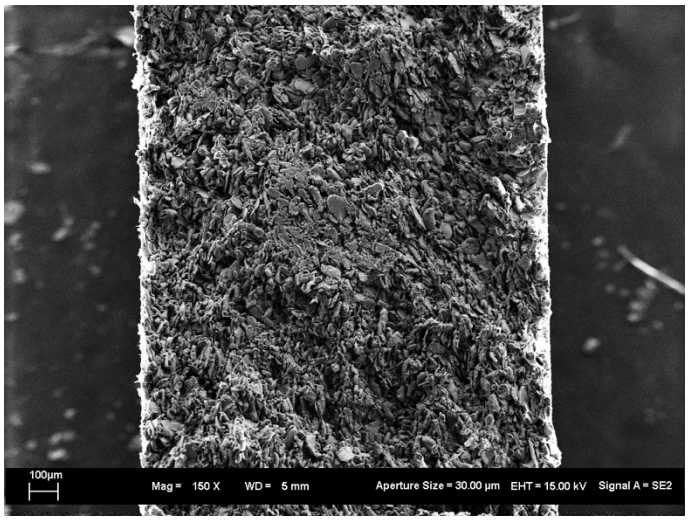

(b)

Figure 37 SEM images of tape formulation n. 2 (a) top side (b) cross section

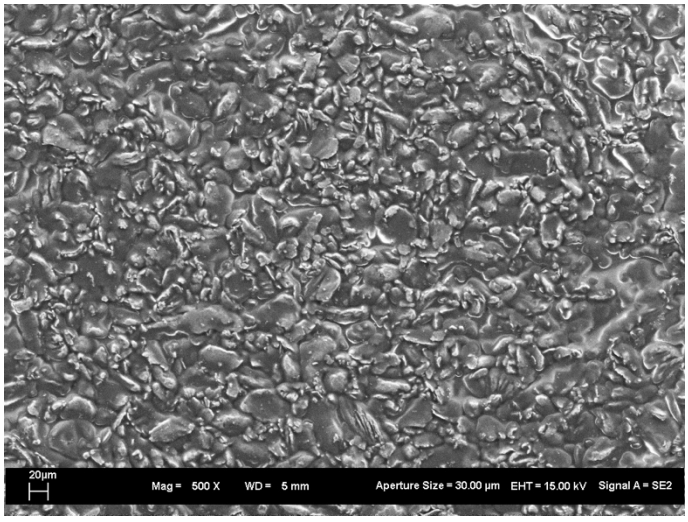

(a)

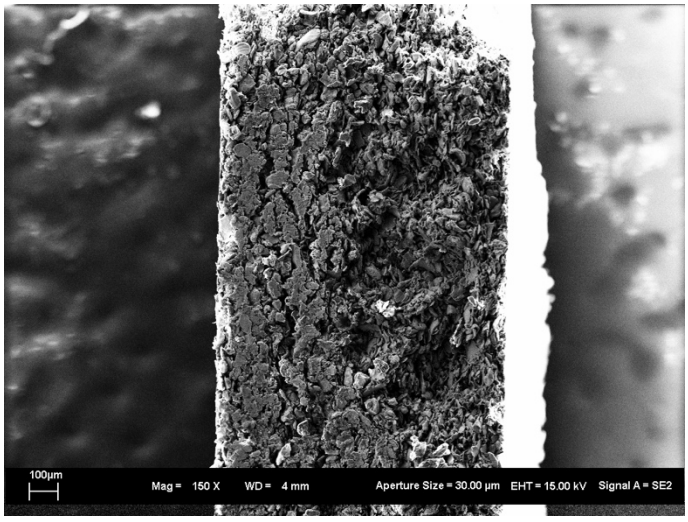

(b)

Figure 38 SEM images of tape formulation n. 3 (a) top side (b) cross section

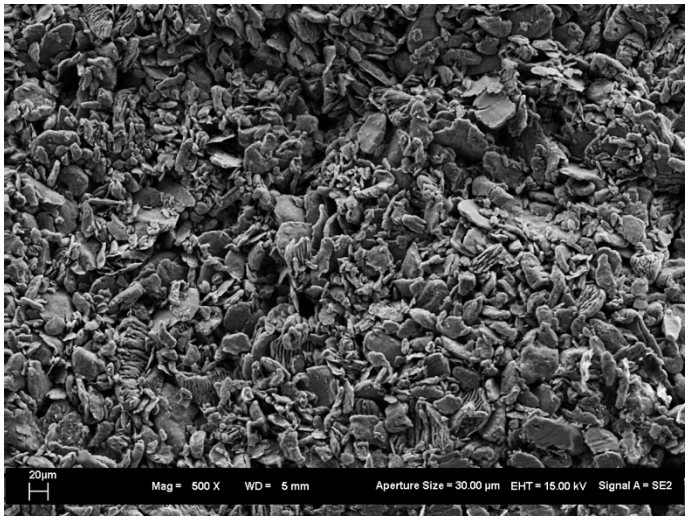

Figure 39 SEM image of tape formulation n. 5, top side

Since the tapes obtained were brittle, a second optimization step was performed in order to reach a higher flexibility of the green and improve the handling of the tapes during the subsequent processes. Therefore, starting from the formulation n. 2, the amount of plasticizer in the formulation was increased respectively of the 10% and 50% (Table 14).

Table 14 Summary of the slurry formulations (plasticizer increase)

Formulation n.	**2**	**2b**	**2c**
Plasticizer increase (%wt)	-	+ 10%	+ 50%
Binder (%wt)	9,37	9,35	9,29
Plasticizer (%wt)	1,69	1,85	2,51
Solvent (%wt)	32,14	32,09	31,87
Dispersant (%wt)	0,60	0,60	0,60
Metallic powder (%wt)	56,20	56,11	55,73
Total (%wt)	100	100	100

The resulting slurries (2b and 2c) were tape casted twice: once with a blade gap of 1 mm and once with a blade gap of 0,7 mm. In both cases the casting speed was of 100 mm/min. The tapes obtained this way were more flexible and maintained a

good homogeneity, with a uniform distribution of the metallic powders and of the binder.

3.4.5 Tape sandwich preparation

After the optimization of the slurry formulation and the production of a homogeneous tape, this was cut in in small square samples (2 cm x 2 cm). The next step was to stack and glue those samples in a sandwich in order to obtain a layered thick object to be sintered.

Different trials were performed with glues produced using the organic components of the slurry. In particular, successful gluing was obtained with a glue formulation made of Methyl ethyl ketone (Solvent) and Dibutyl Phthalate (Plasticizer) as reported in Table 15.

Table 15 Glue formulation

	%wt	**g**
Plasticizer	95,12	19,50
Solvent	4,88	1,00
Total	100	20,50

The gluing process was performed stacking each tape sample on top of the other, using a brush to apply the glue. Afterwards the resulting sandwich was put under a weight for 24 hours. This way a series of sandwiches was produced using the tapes obtained from formulation 2b and 2c, with a blade gap of both 0,7 mm and 1 mm. In particular, 5-layers and 7-layers sandwiches were prepared.

Finally, the resulting samples underwent a debinding and sintering process.

3.4.6 Debinding and sintering

The debinding and sintering process is intended to remove the organic components from the green tape and to allow the densification of the metallic powders. In order to define the most proper thermal treatment, the organic components of the slurry were characterized by means of thermogravimetric analysis (TGA).

Each organic component was put in an alumina (Al_2O_3) crucible and the analysis was performed in a flowing Argon atmosphere. The selected temperature profile consisted of a first static phase at 25°C for 10 min, followed by a temperature increase with a heating rate of 10°C/min up to 650°C (Figure 40).

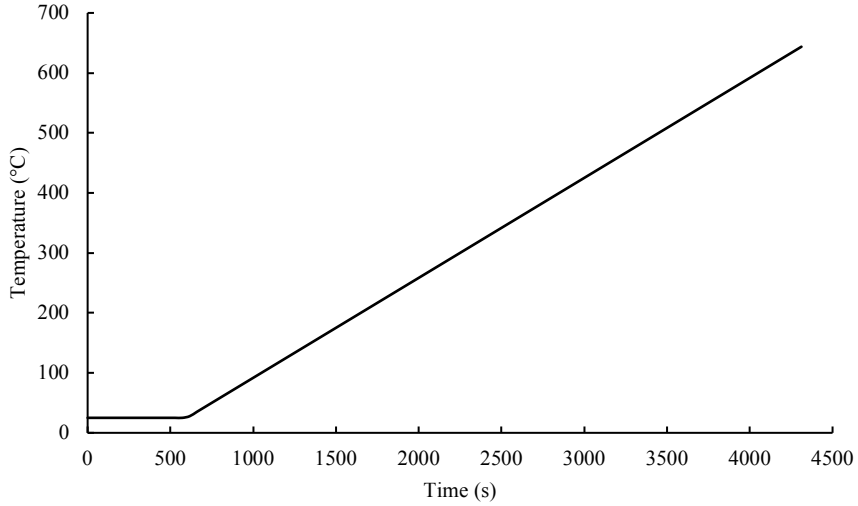

Figure 40 TGA temperature profile

The TGA results are shown in Figure 41. Both the plasticizer (Dibutyl Phthalate) and the binder (Methyl methacrylate ethyl acrylate) were completely removed, respectively at 310°C and 425°C. As far as the dispersant (Hypermer KD-1) is concerned, the degradation proceeds no further above 460°C, leaving a carbon residue of the 1,6% of the initial mass (Figure 41).

In order to tune the thermal profile of the debinding and sintering process, also the degradation rate of the organic components was taken into account. In particular, the degradation rate peak occurs at 305°C for the plasticizer, at 380°C for the binder and at 415°C for the dispersant (Figure 42). Given those results, the maximum temperature that must be reached to remove all the organics from the green tape is 415°C. The carbon residue left by the dispersant is expected to be around the 0,1‰ of the initial mass of the whole green and, therefore, is negligible.

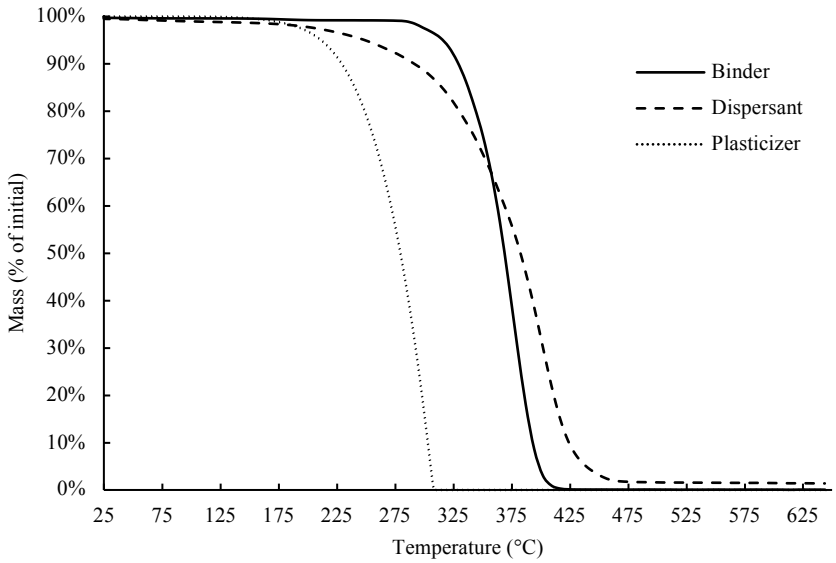

Figure 41 Thermogravimetric analysis (TGA) showing the mass loss vs. temperature of the organic components of the tape formulation

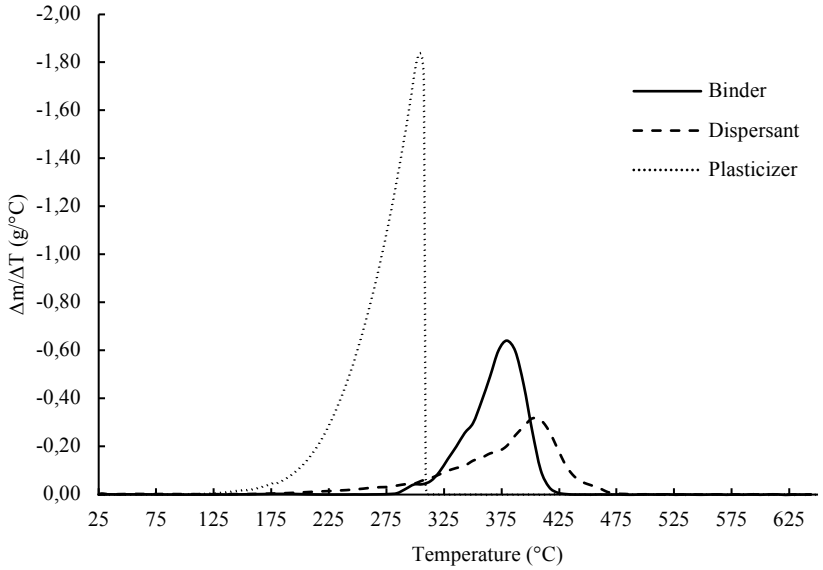

Figure 42 Thermogravimetric analysis (TGA) showing the mass loss rate vs. temperature of the organic components of the tape formulation

The final thermal profile used is shown in Figure 43. The green samples are heated up to 400°C with a heating rate of 1°C/min, then the temperature is kept constant at 400°C for 3h. During this phase all the organic components are removed from the green. Afterwards, the temperature is raised up to 550°C, with a heating rate of 1°C/min, and maintained at 550°C for 2h. This phase is intended to sinter the magnesium powders. Finally, the system is cooled down to room temperature. The overall process is pressureless and conducted in flowing argon.

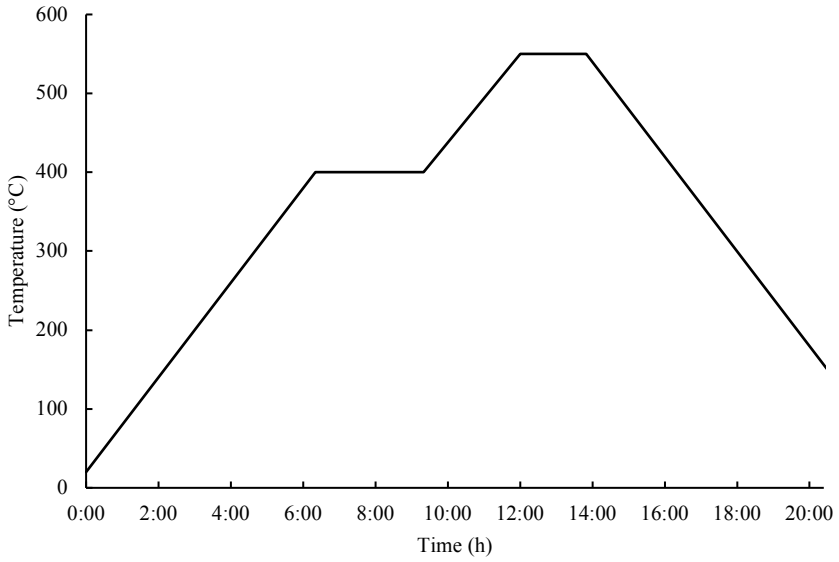

Figure 43 Debinding and sintering thermal profile

The debinding and sintering process was applied to 5 samples, whose characteristics are reported in Table 16.

Table 16 Green samples characteristics

Sample id	Formulation	Layer thickness (mm)	# layers	Green mass (g)	Green density (g/cm3)
A	2b	0,7	5	0,674	0,872
B	2b	0,7	7	1,013	0,824
C	2c	0,7	5	0,745	0,791
D	2c	1	5	1,091	0,859
E	2c	1	7	1,465	0,827

The sintered samples were brittle and difficult to handle. In order to evaluate the degree of sintering that was reached, the samples were cut to observe the cross section, by means of optical microscope. It was possible to observe the cross section of samples A, B and D with a 50x magnification.

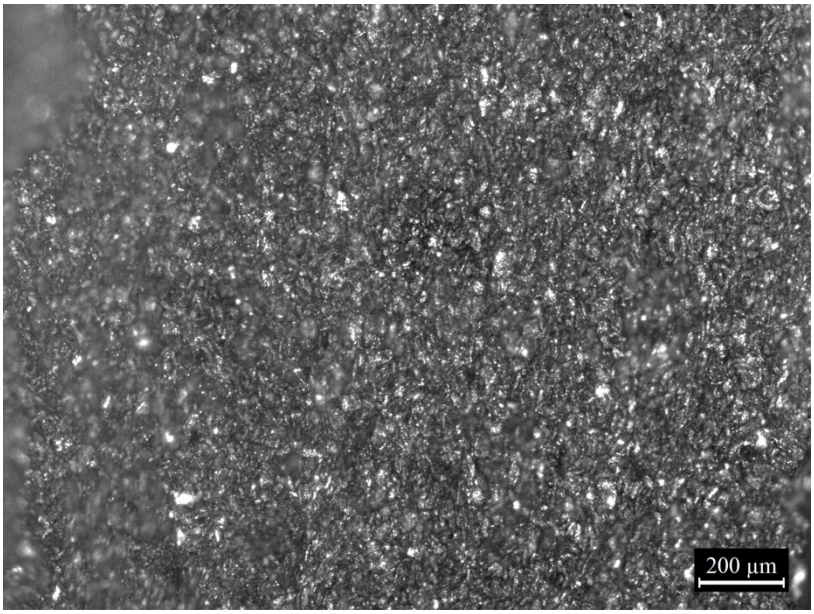

Figure 44 Sample A cross section

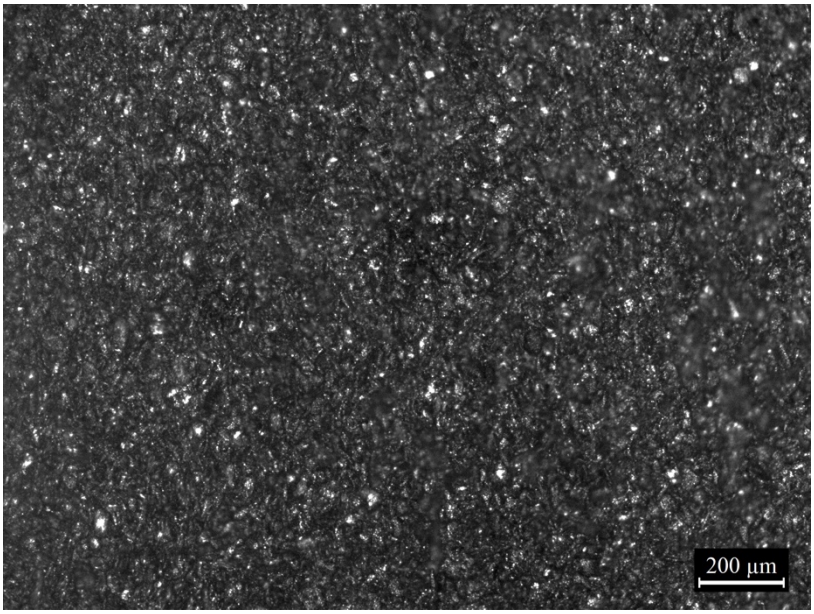

Figure 45 Sample B cross section

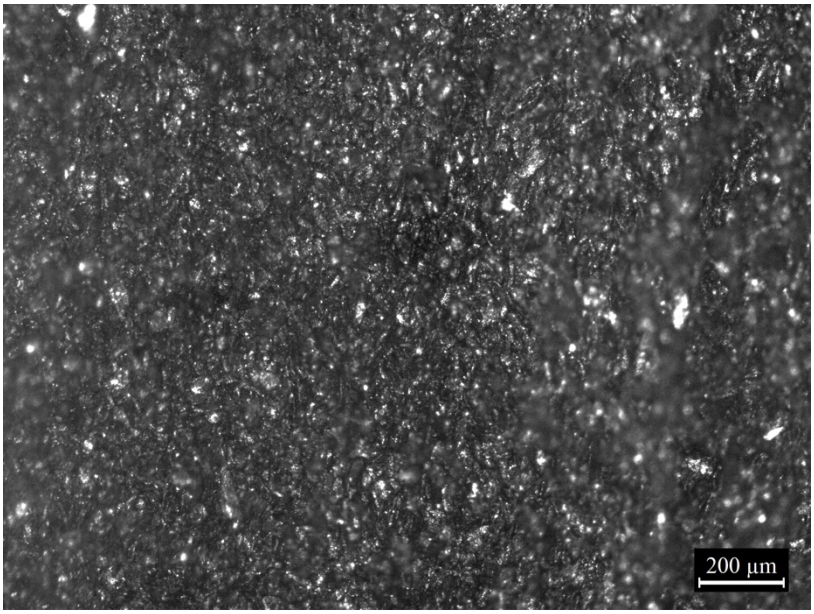

Figure 46 Sample D cross section

All the samples showed a good removal of the organics and a homogeneous structure. In particular, it's not possible to distinguish the single layers, meaning that there was a good coupling among them and that the debinding process was effective. The sintering process, instead, did not perform as expected. In fact, the magnesium powders showed a limited sintering and the single particles are still distinguishable. Furthermore, the brittleness and fragility of the samples is another indicator of the incomplete sintering. Given the quality of the final samples, it was not possible to perform mechanical analyses on them.

3.4.7 Conclusions and further activities

The tape casting process that was studied and tuned up in the present work produced some encouraging results, but also highlighted some critical aspects that need to be addressed. In particular, it was possible to successfully obtain homogeneous magnesium-rich tapes and to stack them to produce thick green samples. Also, the debinding process successfully removed the organic components of the green.

On the contrary, the sintering process was not successful and did not bring to a completely sintered magnesium foam. The failure of the sintering can be traced

back to two possible causes: (1) oxidation of the magnesium powders along the process and/or (2) non-completely optimized sintering parameters.

Regarding the first cause, the overall process involved the handling of magnesium powders and magnesium-rich semifinished product (green tapes) at different stages. The production of the slurry formulation was performed in a glove box under controlled atmosphere (N_2), while the tape casting process and the sandwich preparation were performed in air. Even if the magnesium powders were incorporated within the organic components of the slurry, partial exposure to oxygen may have happened. This exposure can be limited by performing all the operations in a controlled atmosphere. The most critical operation to control strictly is the tape casting itself and a specific setup must be designed.

As far as the sinterization is concerned, the process was performed without applying any pressure since the final goal was to reach a porous structure. A totally pressureless process proved not to be suitable for the purpose because a complete sintering of the metallic powders was not achieved. Further experimental activity is required to introduce and tune the application of a pressure on the green sample during the sintering.

Given the impossibility to bring to completion effectively this manufacturing route, the experimental activities were shifted towards another approach, described in the following.

3.5 An optimized production method including indirect porosity characterization

The second manufacturing route taken into consideration, according to the process selection previously performed, is the method based on the *co-compaction of two materials, one leachable*.

This technique is here adopted in order to produce magnesium foam with open and interconnected porosity, with a fine control on pores size. In this process, two powders of different material (usually a metal and a salt) are mixed and compacted to obtain a co-continuous interconnected structure of both phases. Once the densification is occurred, the salt phase is removed by means of an appropriate solvent.

Furthermore, an improvement of this productive method is here proposed. In fact, the densification in the "traditional" process is obtained under high temperatures and pressures: this causes a deformation of metal and salt particles and it eventually limits the possibility of controlling the final morphology of the porous structure. In order to overcome such issue, the densification of the powders is achieved using *Spark Plasma Sintering* (SPS) technology: metallic powder, mixed with salt powder (in this case NaCl), is introduced in a graphite die and high current pulses (or alternate current) are applied (order of magnitude of hundreds of Ampere). The application of these electrical pulses causes a very high heating of the powders, localized on the particles surface, that leads to the densification of the component, with local fusion of necks between the particles. Thanks to the speed and the local nature of the thermal effect, there is no alteration of the particles morphology. The sintered component obtained by means of this technique is characterized by a co-continuous interconnected structure of the two phases (metal and salt). Then, by means of an appropriate solvent, the salt phase is removed, obtaining the desired metallic foam. [98]

The SPS process has several advantages: given the rapidity of the treatment, there is no crystalline grains growth, and consequently, the size distribution of porosity is determined by the amount of salt powder used, the initial size of NaCl particles and the interaction among magnesium and NaCl powders during the process. A specific milling procedure is adopted in order to obtain the most suitable size distribution of NaCl particles. SPS technique is already successfully used to produce titanium foam [99], but it is new in the case of magnesium foam, since it has not been widely developed in the literature currently available.

The porosity control of magnesium foam is of major importance for the intended application: in a biomimetic perspective, the reproduction of the spongy bone structure requires a fine monitoring and control on average pores size and pores size distribution. Finite Element Modelling (FEM) is proposed in literature for monitoring and control SPS process parameters, such as current and temperature distributions, in order to identify a correlation between them and the sample densification [100], [101]. In the present work, to perform such control, an integrated *in-situ* monitoring system is proposed.

3.5.1 Current porosity characterization techniques

The biomimetic approach, which represents the grounding of the present thesis, claims for the achievement of a porous structure as close as possible to the

cancellous bone one. Therefore, an accurate measurement and control of pores morphology, as well as pores size distribution, is essential. Generally, this requirement can be met through the optimization of the production process of the metallic foam, i.e. by tuning the experimental settings with an iterative fashion.

On the other hand, the analytical techniques for the characterization of porous materials currently available are manifold. They are generally grouped into two categories: *non-destructive testing* and *destructive testing*. The methods belonging to the first category are intended to assess primarily the morphology of pores, while the others can be used to evaluate both the morphology and the mechanical properties of porous materials. Table 17 summarizes the most relevant techniques for porous materials characterization [102].

Table 17 Current characterization techniques for porous materials

Non-destructive testing	Brief description	Advantages	Limits
Density measurements	Based on Archimedes' principle to measure weight and volume of the sample	Easy and quick	Indication of the porosity percentage, not morphology
X-ray radiography and radioscopy	Mapping by X-ray absorption techniques	Resolution of single pores and true pore morphology	Effective only on very thin slices of material (surface measurement)
X-ray computed tomography	Large number of X-ray images obtained from different directions and combined to create a 3D model of the sample	3D virtual reconstruction of the foam morphology	Usually with low resolution, suitable for millimetric pores
Eddy-current sensoring	Multifrequency electrical impedance measurements	Measurement of local density of the foam	Requires accurate calibration
Acoustic measurements	Sound absorption measured in an impedance tube	Quick and precise measurement	More effective for open porosity
Vibrational analysis	The sample is forced into vibrations to determine Young's modulus and loss factor related to mass distribution and to porosity	Non-destructive measurement of the mechanical properties	Average values of Young's modulus and loss factor not accounting for the inhomogeneities of the sample
Porosimetry and permeametry	Based on the intrusion and/or extrusion of a fluid throughout the sample	Measurement of specific surface area, pore size distribution and channel size distribution	Suitable for just open porosity

Non-destructive testing	Brief description	Advantages	Limits
Electrical conductivity measurements	Measurement of electrical resistivity of the porous sample in the four point mode	Straightforward	Small cross-section desiderable and problems arising from the contact between the leads and the foam
Destructive testing	**Brief description**	**Advantages**	**Limits**
Optical image or SEM analysis	Observation at various magnification of the surface and/or cross-section of the sample	Measurement of pore size distribution and pore geometry	Surface analysis requires interpretation
Mechanical testing	Analogous to mechanical testing methods for bulk materials, particularly compression test	Complete mechanical characterization of the foam structure	To obtain meaningful results a lot of sample have to be tested

From data presented in Table 17, it results that most of the current techniques for porosity measurement have some limitations and that a comprehensive investigation of the morphology of the porous sample can be performed only by means of destructive tests. The indirect characterization method proposed in the present work aims at overcoming some of these limitations. Furthermore, the presented approach is potentially a control system of the foam production process.

3.5.2 Theoretical model

The goal of the measurement procedure is to relate the production process parameters with the porosity of the sample while the densification is ongoing. In particular, such measurement is based on the electrical parameters that characterize the SPS process. In fact, the AC generator imposes a predetermined current on the system, continuously adjusting the voltage applied. Current and voltage are varied according to the system impedance which changes throughout the process: thus, the system impedance can be used to have an indication about the progress of the material densification. Combining the information collected *in-situ* with traditional analyses on porosity is then possible to create a model to predict the evolution of the porous structure and to setup a procedure to obtain the desired morphology with a fine control on porosity.

The major issue is the monitoring of the sample impedance throughout the SPS densification process. Figure 47 shows the experimental setup of the SPS system: inside the vacuum SPS chamber, the sample is located between two graphite punches and enclosed within a graphite die. A thermocouple is put in contact with the graphite die to measure the temperature of the system.

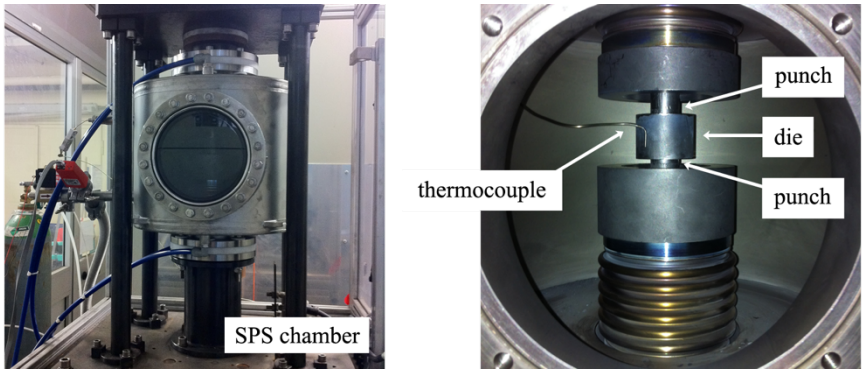

Figure 47 Experimental setup of the SPS system. On the left it is shown the closed vacuum chamber while on the right the interior is presented: the sample is located between the two graphite punches and enclosed inside the graphite die. The thermocouple is put in contact with the graphite die. [98]

In Figure 48a, it is presented a schematic representation of such system. On a first approximation, the electrical topology is modelled as indicated in Figure 48b: the sections of the die in contact with the punches are incorporated in the punches resistance (R_{punch}), while the section of the die in contact with the sample represents the die resistance (R_{die}). Figure 48c shows the equivalent circuit of such electrical topology. The punches resistance ($R_{punches\ eq}$) is in series with the parallel of the die resistance (R_{die}) and the sample resistance (R_{sample}). Other contributes to the overall resistance of the system (not reported in Figure 48 for scheme clarity) are the contact points among the different parts. Such contact resistance can be particularly relevant for some process conditions and geometries [100] and, therefore, cannot be neglected. In agreement with [100], if the pressure applied on the punches is constant during the process, the contact resistance can be assumed to remain constant as well.

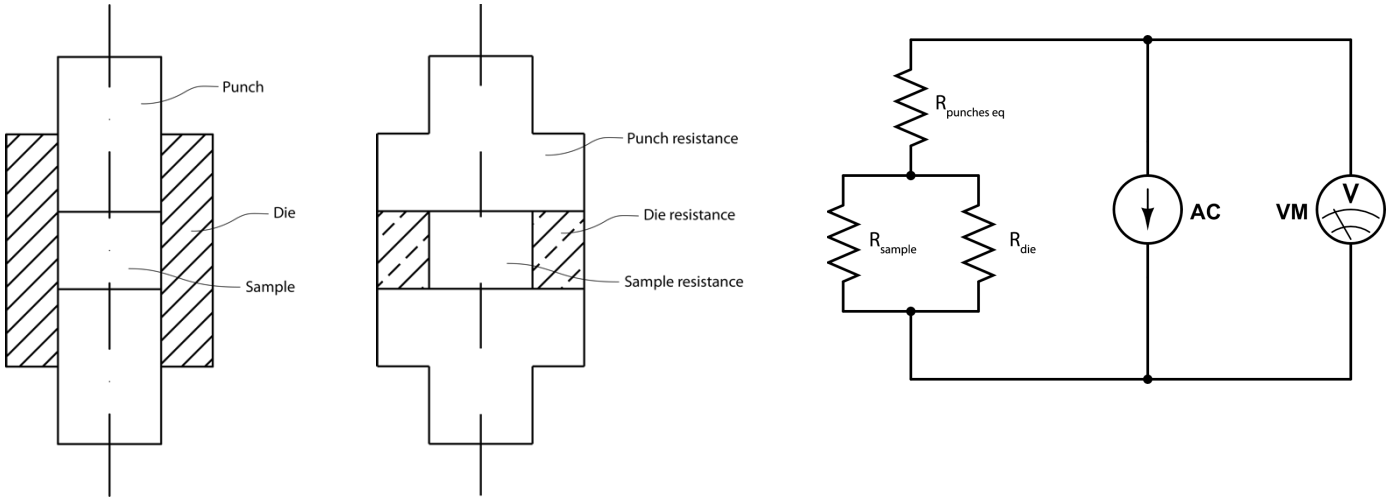

a b c

Figure 48 (a) Holder of the sample in the SPS chamber (b) Electrical topology of the sample holder (c) Equivalent electrical circuit of the sample and holder system [98]

While the SPS process is ongoing the applied alternate current and voltage are monitored as function of time, as well as the temperature of the graphite die. Appling the Ohm's law, it is possible to compute the overall impedance of the system as a function of time:

$$\overrightarrow{Z_{tot}}(t) = \frac{\vec{V}(t)}{\vec{I}(t)}$$

On first approximation, the reactance of the system can be neglected so that:

$$\overrightarrow{Z_{tot}}(t) \cong R_{tot}(t)$$

This assumption is supported by the experimental measurements which showed a value of the power factor constantly equal to about 1.

The resistance of the graphite die and of the punches is dependent on the temperature of the system, that changes with time. Therefore, it is necessary to measure the characteristic $R_{graphite}(T)$ of the die and punches by means of a fully ceramic, non-conductive, sample test. Such test is performed by replacing the

magnesium/NaCl sample with the same volume of alumina (Al_2O_3) powder: this way the geometry of the system is the same and the alumina powder works as electrical insulator. With this test, the resistance of punches ($R_{punches\ eq}$) and die (R_{die}) is globally evaluated, even if, with the current equipment, it is still not possible to distinguish the separate contributions. Such measure includes also the contact resistance. This way it is possible to have a reference to be used for obtaining a measure of R_{sample} not affected by the resistance variation of the graphite parts and by the contact resistances.

The function $R_{sample}(t)$ is expected to have a trend variation corresponding to the densification process of the sample. In fact, on one hand the resistivity of magnesium powder rises with temperature almost linearly. On the other hand, during the sintering, the particles surface is reduced by the formation of necks among them: this results in a progressive decrease of the specific area of the porous sample and, accordingly, its resistance is expected to decrease. While the densification is ongoing these two phenomena have opposite effects and their interaction should result in a deviation from the regular trend of the overall resistance function.

The porosity of the magnesium foams depends on different factors, both related to the powders mix characteristics and to the SPS process parameters (current, temperature, time, pressure, etc).

3.5.3 Experimental procedure

A series of samples of porous magnesium were produced with the method previously described, monitoring the electrical parameters of the process, as well as the temperature.

The samples were made by mixing pure magnesium powder, with particle diameter around 50 μm, and NaCl powder, with particle diameter in the range 50 – 100 μm. The NaCl powder size distribution was obtained by ball milling: an agate grinding system (agate bowl + 250 agate balls with diameter 0,5 cm) was used and the desired granulometry was reached after 60 minutes of grinding at 160 rpm. The final grain size distribution was evaluated by means of FESEM (Field Emission Scanning Electron Microscope – Supra 40 Zeizz), as shown in Figure 49.

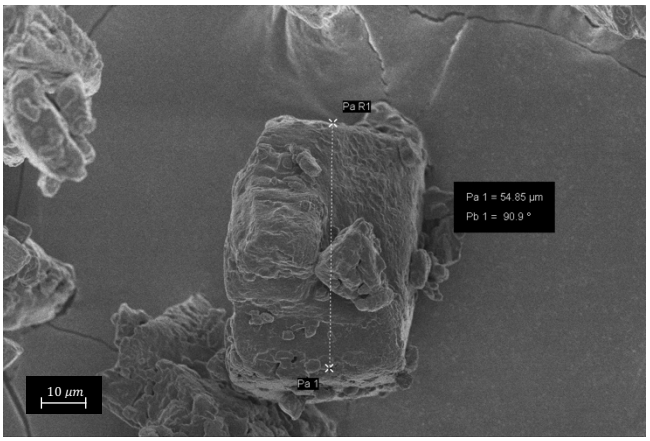

Figure 49 FESEM image of NaCl grinded powder sample

The same ball mill was used to mix magnesium powder and NaCl powder (10 minutes at 120 rpm). The volume ratio between magnesium powder and NaCl powder was 70%vol – 30%vol for Sample A, while it was 50%vol – 50%vol for Sample B. The total volume of the mixed powder was 1,5 cm^3 for both the samples. The graphite punches that were used had a diameter of 20 mm and a height of 25 mm, while the die had an external diameter of 40 mm and a height of 30 mm. The SPS process was conducted in inert atmosphere (Argon) and an AC (50 Hz) was applied for 15 min, with a constant value of 450 A. The temperature of the system (reported in Figure 50) was measured on the external surface of the graphite die by means of a thermocouple. Voltage, current intensity and resistance of the system were measured every 10 s. Afterwards, maintaining the same process parameters, two alumina sample tests were performed to evaluate the resistance of just the graphite die and punches with the same temperature ramps.

Afterwards, the samples obtained were rinsed in NaOH solution (with pH = 11,5) for 20 min in order to remove the NaCl and set the porosities free. Finally, a cross-section of the sample was obtained and rinsed in the same solution for 5 min more in order to observe the internal morphology by means of FESEM (Field Emission Scanning Electron Microscope – Supra 40 Zeizz).

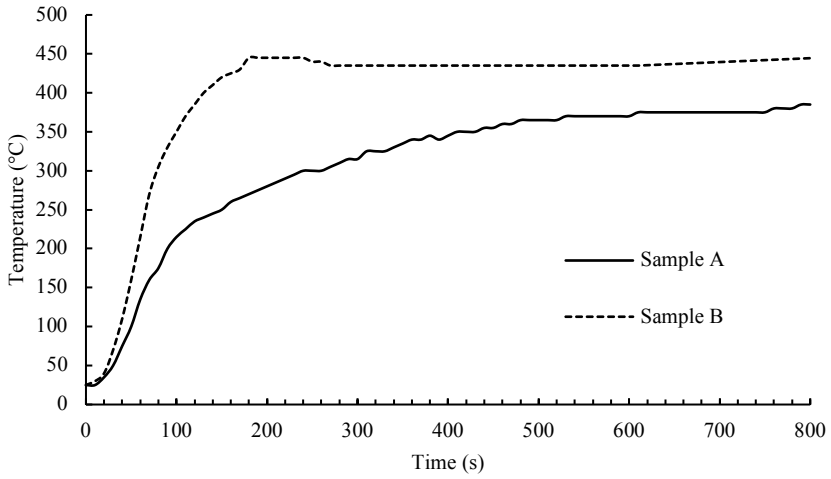

Figure 50 Temperature of the system measured during the SPS process of Sample A and Sample B

3.5.4 Results

In Figure 51 the resistance functions measured during the SPS process of Sample A and Sample B are reported, comparing each sample with the respective fully ceramic test.

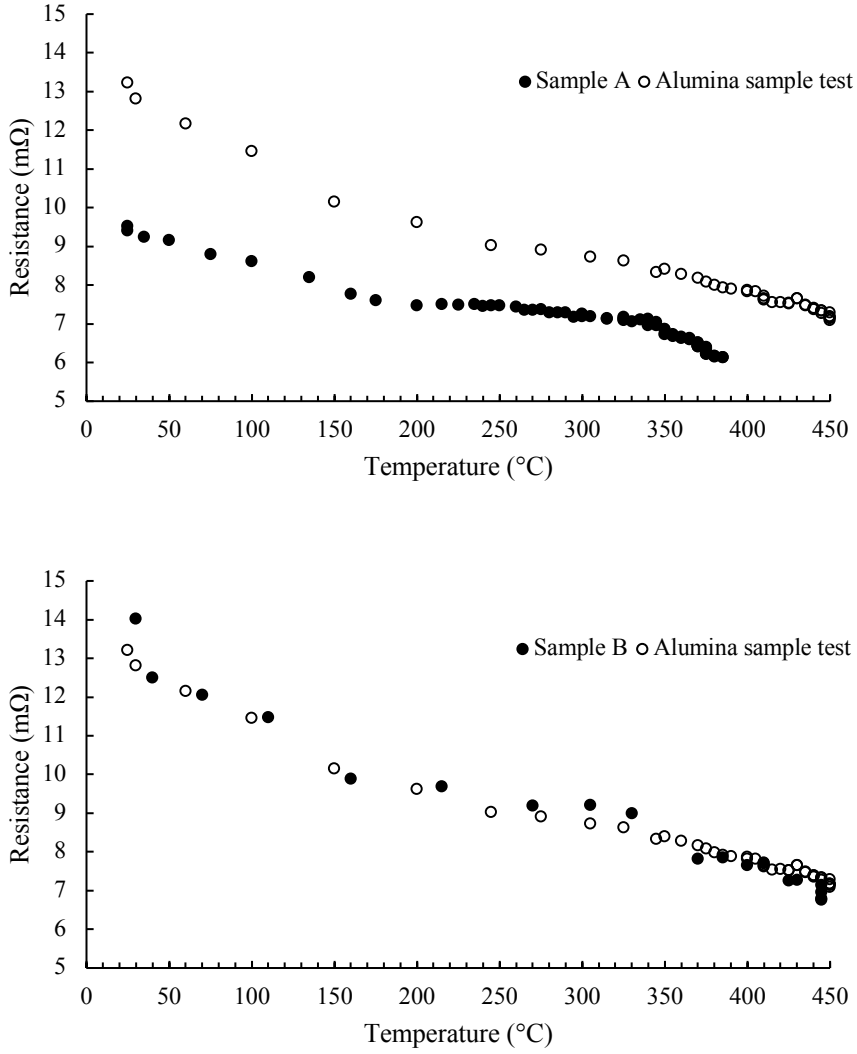

Figure 51 Resistance functions measured during the SPS process of Sample A (above) and Sample B (below), compared with the respective alumina sample test resistance functions.

As far as Sample A is concerned, the two resistance functions are clearly distinguishable, and they decrease with different rates. In particular, it is possible to point out a plateau region for the sample resistance in the temperature interval between 200°C and 330°C (timeframe 90 s – 340 s). This trend variation is an interesting phenomenon that is being modelled. Furthermore, it can be hypothesized that the densification process occurs during the plateau interval.

Data related to Sample B show that there is no appreciable difference between the resistance function relating to the magnesium/NaCl sample and the fully ceramic one. This result can be related to the increase of the volume fraction of NaCl from 30% to 50% that reduces the overall conductivity of the sample.

Sample A is presented in Figure 52. From an optical inspection it is possible to identify a uniform distribution of the porosity, with a wide size distribution of pores. Figure 53 reports a FESEM image of the fracture surface of Sample A. The FESEM image shows the presence of a high percentage of porosity, with submicrometric pores size, coherent with the dimension of the crystalline grains which build up the polycrystalline structure of the particles of the powders mixture.

The FESEM image of Sample B is presented in Figure 54. The increase of NaCl content resulted in higher porosity percentage and larger dimension of pores (micrometric). Furthermore, it is possible to observe an extended fracture crack that can be associated with higher fragility of Sample B with respect to Sample A.

In both samples, NaCl traces are still present on the external surface and on the fracture surface, meaning that the rinsing procedure has not been completely effective.

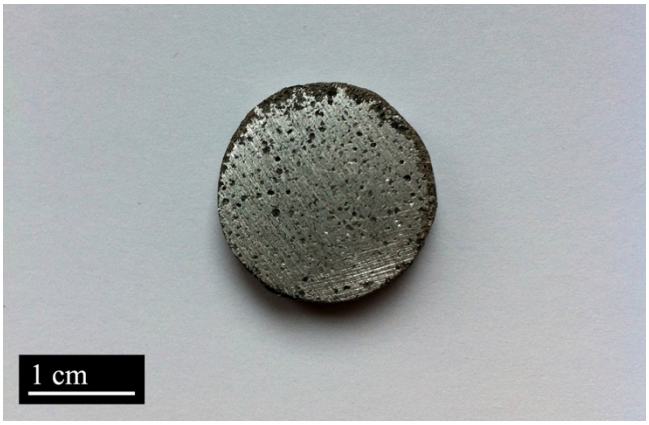

Figure 52 Image of Sample A surface after NaCl dissolution

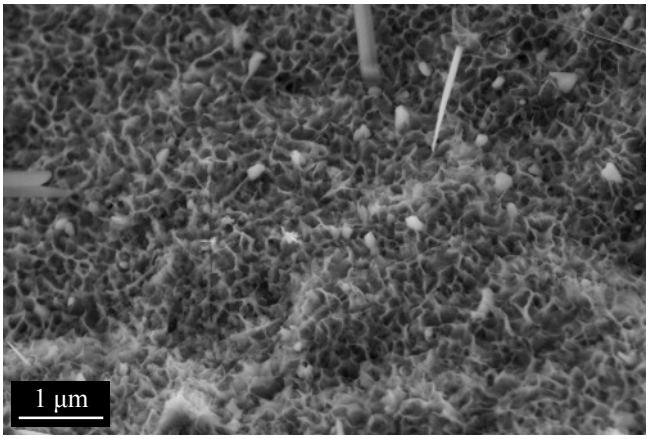

Figure 53 FESEM image of Sample A fracture surface after NaCl dissolution

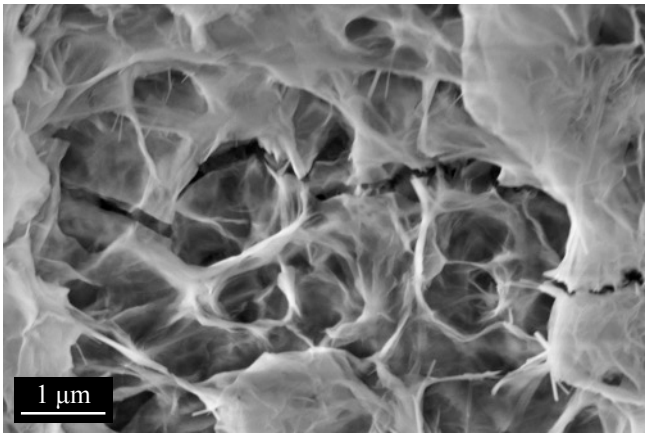

Figure 54 FESEM image of Sample B fracture surface after NaCl dissolution

3.5.5 Conclusions and further activities

The results obtained with these tests are encouraging and a preliminary correlation between the electrical parameters of the SPS process and the sample morphology can be observed, particularly in the case of samples with high magnesium volume fraction. More critical is the interpretation of the results related to NaCl-richer samples, since it is not possible to see a proper distinction between the two resistance functions introduced in the electrical model. This model seems to fall apart when the conductivity of the sample is too low, as in the case of NaCl-richer samples, but such result can be also ascribed to the sensibility of the current instrumental setup, that it is too low.

Currently the experimental results need to be integrated within a mathematical model that is being developed. Furthermore, the instrumentation used is still affected by too large measure uncertainty and a new measurement setup is under development in order to get rid of such uncertainty and to have a higher measurement sensibility.

Finally, further experiments are required to define a proper relation to forecast the resulting porosity of the magnesium foam from the evolution of the sample resistance with the time.

References

[1] D. S. T. Edge2003, “The beauty of biomimicry,” 2AD.

[2] R. Zeng, W. Dietzel, F. Witte, N. Hort, and C. Blawert, “Progress and Challenge for Magnesium Alloys as Biomaterials,” *Adv. Eng. Mater.*, vol. 10, no. 8, pp. B3–B14, Aug. 2008.

[3] M. P. Staiger, A. M. Pietak, J. Huadmai, and G. Dias, “Magnesium and its alloys as orthopedic biomaterials: A review,” *Biomaterials*, vol. 27, no. 9, pp. 1728–1734, Mar. 2006.

[4] A. H. Yusop, A. A. Bakir, N. A. Shaharom, M. R. Abdul Kadir, and H. Hermawan, “Porous Biodegradable Metals for Hard Tissue Scaffolds: A Review,” *International Journal of Biomaterials*, vol. 2012, no. 4, pp. 1–10, 2012.

[5] X. N. Gu, W. R. Zhou, Y. F. Zheng, Y. Liu, and Y. X. Li, “Degradation and cytotoxicity of lotus-type porous pure magnesium as potential tissue engineering scaffold material,” *Materials Letters*, vol. 64, no. 17, pp. 1871–1874, Sep. 2010.

[6] P. Freni, E. M. Botta, L. Randazzo, and P. Ariano, *Innovative Hand Exoskeleton Design for Extravehicular Activities in Space*. Cham: Springer International Publishing, 2014.

[7] P. Freni and M. Stoppa, “Deformable actuating device with coaxial configuration,” WO2015145476 A1, 2015.

[8] D. Chen and Q. Pei, “Electronic Muscles and Skins: A Review of Soft Sensors and Actuators,” *Chem. Rev.*, vol. 117, no. 17, pp. 11239–11268, Sep. 2017.

[9] M. Milwich, S. K. Selvarayan, and G. T. Gresser, “Fibrous Materials and Textiles for Soft Robotics,” in *Soft Robotics*, no. 14, Berlin, Heidelberg: Springer Berlin Heidelberg, 2015, pp. 157–172.

[10] J. D. W. Madden, N. A. Vandesteeg, P. A. Anquetil, P. G. A. Madden, A. Takshi, R. Z. Pytel, S. R. Lafontaine, P. A. Wieringa, and I. W. Hunter, “Artificial Muscle Technology: Physical Principles and Naval Prospects,” *IEEE Journal of Oceanic Engineering*, vol. 29, no. 3, pp. 706–728, Jul. 2004.

[11] R. Pelrine, R. D. Kornbluh, Q. Pei, S. Stanford, S. Oh, J. Eckerle, R. J. Full, M. A. Rosenthal, and K. Meijer, “Dielectric elastomer artificial muscle actuators: toward biomimetic motion,” presented at the SPIE's 9th Annual International Symposium on Smart Structures and Materials, 2002, vol. 4695, pp. 126–137.

[12] P. Brochu and Q. Pei, “Advances in Dielectric Elastomers for Actuators and Artificial Muscles,” *Macromolecular Rapid Communications*, vol. 31, no. 1, pp. 10–36, Jan. 2010.

[13] F. Carpi, R. Kornbluh, P. Sommer-Larsen, and G. Alici, “Electroactive polymer actuators as artificial muscles: are they ready for bioinspired applications?,” *Bioinspiration & Biomimetics*, vol. 6, no. 4, p. 045006, Nov. 2011.

[14] Y. Bar-Cohen, “Electroactive polymers: current capabilities and challenges,” presented at the SPIE's 9th Annual International Symposium on Smart Structures and Materials, 2002, vol. 4695, pp. 1–7.

[15] S. Nemat-Nasser, “Micromechanics of actuation of ionic polymer-metal composites,” *Journal of Applied Physics*, vol. 92, no. 5, pp. 2899–2915, Sep. 2002.

[16] M. Shahinpoor and K. J. Kim, “Ionic polymer–metal composites: IV. Industrial and medical applications,” *Smart Mater. Struct.*, vol. 14, no. 1, pp. 197–214, Dec. 2004.

[17] Y. Bahramzadeh and M. Shahinpoor, “A Review of Ionic Polymeric Soft Actuators and Sensors,” *Soft Robotics*, vol. 1, no. 1, pp. 38–52, Mar. 2014.

[18] Q. Pei and O. Inganaes, “Electrochemical applications of the bending beam method. 1. Mass transport and volume changes in polypyrrole

during redox," *The Journal of Physical Chemistry*, vol. 96, no. 25, pp. 10507–10514, Dec. 1992.

[19] Q. Pei and O. Inganaes, "Electrochemical applications of the bending beam method. 2. Electroshrinking and slow relaxation in polypyrrole," *The Journal of Physical Chemistry*, vol. 97, no. 22, pp. 6034–6041, Jun. 1993.

[20] R. Shankar, T. K. Ghosh, and R. J. Spontak, "Dielectric elastomers as next-generation polymeric actuators," *Soft Matter*, vol. 3, no. 9, pp. 1116–1129, 2007.

[21] J. D. W. Madden, J. N. Barisci, P. A. Anquetil, G. M. Spinks, G. G. Wallace, R. H. Baughman, and I. W. Hunter, "Fast Carbon Nanotube Charging and Actuation," *Adv. Mater.*, vol. 18, no. 7, pp. 870–873, Apr. 2006.

[22] Q. M. Zhang, "Giant Electrostriction and Relaxor Ferroelectric Behavior in Electron-Irradiated Poly(vinylidene fluoride-trifluoroethylene) Copolymer," *Science*, vol. 280, no. 5372, pp. 2101–2104, Jun. 1998.

[23] R. Pelrine, "High-Speed Electrically Actuated Elastomers with Strain Greater Than 100%," *Science*, vol. 287, no. 5454, pp. 836–839, Feb. 2000.

[24] F. Carpi, I. Anderson, S. Bauer, G. Frediani, G. Gallone, M. Gei, C. Graaf, C. Jean-Mistral, W. Kaal, G. Kofod, M. Kollosche, R. Kornbluh, B. Lassen, M. Matysek, S. Michel, S. Nowak, B. O'Brien, Q. Pei, R. Pelrine, B. Rechenbach, S. Rosset, and H. Shea, "Standards for dielectric elastomer transducers," *Smart Mater. Struct.*, vol. 24, no. 10, p. 105025, Sep. 2015.

[25] A. E. Aliev, J. Oh, M. E. Kozlov, A. A. Kuznetsov, S. Fang, A. F. Fonseca, R. Ovalle, M. D. Lima, M. H. Haque, Y. N. Gartstein, M. Zhang, A. A. Zakhidov, and R. H. Baughman, "Giant-stroke, superelastic carbon nanotube aerogel muscles.," *Science*, vol. 323, no. 5921, pp. 1575–1578, Mar. 2009.

[26] R. Pelrine, R. Kornbluh, J. Joseph, R. Heydt, Q. Pei, and S. Chiba, "High-field deformation of elastomeric dielectrics for actuators," *Materials Science and Engineering: C*, vol. 11, no. 2, pp. 89–100, Nov. 2000.

[27] K. Meijer, M. S. Rosenthal, and R. J. Full, “Muscle-like actuators? A comparison between three electroactive polymers,” presented at the SPIE's 8th Annual International Symposium on Smart Structures and Materials, 2001, vol. 4329, pp. 7–16.

[28] G. M. Spinks, V. Mottaghitalab, M. Bahrami-Samani, P. G. Whitten, and G. G. Wallace, “Carbon-Nanotube-Reinforced Polyaniline Fibers for High-Strength Artificial Muscles,” *Adv. Mater.*, vol. 18, no. 5, pp. 637–640, Mar. 2006.

[29] F. Xia, Z. Y. Cheng, H. S. Xu, H. F. Li, Q. M. Zhang, G. J. Kavarnos, R. Y. Ting, G. Abdul-Sadek, and K. D. Belfield, “High Electromechanical Responses in a Poly(vinylidene fluoride-trifluoroethylene-chlorofluoroethylene) Terpolymer,” *Adv. Mater.*, vol. 14, no. 21, pp. 1574–1577, Nov. 2002.

[30] R. D. Kornbluh, R. Pelrine, Q. Pei, S. Oh, and J. Joseph, “Ultrahigh strain response of field-actuated elastomeric polymers,” presented at the SPIE's 7th Annual International Symposium on Smart Structures and Materials, 2000, vol. 3987, pp. 51–65.

[31] R. E. Pelrine, R. D. Kornbluh, and J. P. Joseph, “Electrostriction of polymer dielectrics with compliant electrodes as a means of actuation,” *Sensors and Actuators A: Physical*, vol. 64, no. 1, pp. 77–85, Jan. 1998.

[32] A. Favetto, F. Chen Chen, E. P. Ambrosio, D. Manfredi, and G. C. Calafiore, “Towards a hand exoskeleton for a smart EVA glove,” presented at the 2010 IEEE International Conference on Robotics and Biomimetics (ROBIO), 2010, pp. 1293–1298.

[33] G. Kofod, “The static actuation of dielectric elastomer actuators: how does pre-stretch improve actuation?,” *Journal of Physics D: Applied Physics*, vol. 41, no. 21, p. 215405, Oct. 2008.

[34] S. P. Timoshenko and J. N. Goodier, *Theory of Elasticity (3rd ed.)*. Singapore, 1970.

[35] A. Mazzoldi, C. Degl'Innocenti, M. Michelucci, and D. De Rossi, “Actuative properties of polyaniline fibers under electrochemical stimulation,” *Materials Science and Engineering: C*, vol. 6, no. 1, pp. 65–72, Sep. 1998.

[36] R. Pelrine, “Variable Stiffness Mode: Devices and Applications,” in *Dielectric Elastomers as Electromechanical Transducers*, Elsevier, 2008, pp. 141–145.

[37] D. R. Sumner, T. M. Turner, R. Igloria, R. M. Urban, and J. O. Galante, "Functional adaptation and ingrowth of bone vary as a function of hip implant stiffness," *Journal of Biomechanics*, vol. 31, no. 10, pp. 909–917, Oct. 1998.

[38] D. M. Robertson, L. St Pierre, and R. Chahal, "Preliminary observations of bone ingrowth into porous materials," *J. Biomed. Mater. Res.*, vol. 10, no. 3, pp. 335–344, May 1976.

[39] H. U. Cameron, I. Macnab, and R. M. Pilliar, "A porous metal system for joint replacement surgery.," *Int J Artif Organs*, vol. 1, no. 2, pp. 104–109, Mar. 1978.

[40] W. C. Head, D. J. Bauk, and J. R. Emerson, "Titanium as the material of choice for cementless femoral components in total hip arthroplasty.," *Clin Orthop Relat Res*, no. 311, pp. 85–90, Feb. 1995.

[41] R. Zeng, W. Dietzel, F. Witte, N. Hort, and C. Blawert, "Progress and Challenge for Magnesium Alloys as Biomaterials," *Adv. Eng. Mater.*, vol. 10, no. 8, pp. B3–B14, Aug. 2008.

[42] V. KARAGEORGIOU and D. KAPLAN, "Porosity of 3D biomaterial scaffolds and osteogenesis," *Biomaterials*, vol. 26, no. 27, pp. 5474–5491, Sep. 2005.

[43] D. T. REILLY and A. H. BURSTEIN, "The Mechanical Properties of Cortical Bone," *The Journal of Bone & Joint Surgery*, vol. 56, no. 5, pp. 1001–1022, Jul. 1974.

[44] L. MATHIEU, T. MUELLER, P. BOURBAN, D. PIOLETTI, R. MULLER, and J. MANSON, "Architecture and properties of anisotropic polymer composite scaffolds for bone tissue engineering," *Biomaterials*, vol. 27, no. 6, pp. 905–916, Feb. 2006.

[45] G. Ryan, G. RYAN, A. PANDIT, A. Pandit, D. P. Apatsidis, and D. APATSIDIS, "Fabrication methods of porous metals for use in orthopaedic applications," *Biomaterials*, vol. 27, no. 13, pp. 2651–2670, May 2006.

[46] X. N. Gu, W. R. Zhou, Y. F. Zheng, Y. Liu, and Y. X. Li, "Degradation and cytotoxicity of lotus-type porous pure magnesium as potential tissue engineering scaffold material," *Materials Letters*, vol. 64, no. 17, pp. 1871–1874, Sep. 2010.

[47] F. Witte, H. Ulrich, M. Rudert, and E. Willbold, “Biodegradable magnesium scaffolds: Part 1: Appropriate inflammatory response,” *J. Biomed. Mater. Res.*, vol. 81, no. 3, pp. 748–756, Jun. 2007.

[48] F. Witte, H. Ulrich, C. Palm, and E. Willbold, “Biodegradable magnesium scaffolds: Part II: Peri-implant bone remodeling,” *J. Biomed. Mater. Res.*, vol. 81, no. 3, pp. 757–765, Jun. 2007.

[49] K. Alvarez and H. Nakajima, “Metallic Scaffolds for Bone Regeneration,” *Materials*, vol. 2, no. 3, pp. 790–832, Sep. 2009.

[50] B. Heublein, “Biocorrosion of magnesium alloys: a new principle in cardiovascular implant technology?,” *Heart*, vol. 89, no. 6, pp. 651–656, Jun. 2003.

[51] F. Witte, V. Kaese, H. Haferkamp, E. Switzer, A. Meyer-Lindenberg, C. J. Wirth, and H. Windhagen, “In vivo corrosion of four magnesium alloys and the associated bone response,” *Biomaterials*, vol. 26, no. 17, pp. 3557–3563, Jun. 2005.

[52] F. Witte, J. Fischer, J. Nellesen, H.-A. Crostack, V. Kaese, A. Pisch, F. Beckmann, and H. Windhagen, “In vitro and in vivo corrosion measurements of magnesium alloys,” *Biomaterials*, vol. 27, no. 7, pp. 1013–1018, Mar. 2006.

[53] Z. Li, X. Gu, S. Lou, and Y. Zheng, “The development of binary Mg–Ca alloys for use as biodegradable materials within bone,” *Biomaterials*, vol. 29, no. 10, pp. 1329–1344, Apr. 2008.

[54] E. Zhang, L. Xu, G. Yu, F. Pan, and K. Yang, “In vivoevaluation of biodegradable magnesium alloy bone implant in the first 6 months implantation,” *J. Biomed. Mater. Res.*, vol. 90, no. 3, pp. 882–893, Sep. 2009.

[55] C. E. Wen, Y. Yamada, K. Shimojima, Y. Chino, H. Hosokawa, and M. Mabuchi, “Compressibility of porous magnesium foam: dependency on porosity and pore size,” *Materials Letters*, vol. 58, no. 3, pp. 357–360, Jan. 2004.

[56] K. Alvarez and H. Nakajima, “Metallic Scaffolds for Bone Regeneration,” *Materials*, vol. 2, no. 3, pp. 790–832, Sep. 2009.

[57] M. F. Ashby, T. Evans, N. A. Fleck, J. W. Hutchinson, H. N. G. Wadley, and L. J. Gibson, *Metal Foams: A Design Guide*. Elsevier, 2000.

[58] M. Thomas, D. Kenny, H. Sang, Rio Tinto Alcan International Ltd, "Particle-stabilized metal foam and its production," Apr. 1997.

[59] I. Jin, L. D. Kenny, H. Sang, Rio Tinto Alcan International Ltd, "Method of producing lightweight foamed metal," Nov. 1990.

[60] V. Gergely and T. W. Clyne, "The Effect of Oxide Layers on Gas-Generating Hydride Particles During Production of Aluminium Foams," *MRS Proceedings*, vol. 521, p. 2783, Feb. 2011.

[61] M. Tane and H. Nakajima, "Fabrication of porous magnesium with directional pores through use of hydrogen thermally decomposed from MgH2 powders during unidirectional solidification," *Journal of Materials Research*, vol. 23, no. 3, pp. 849–855, Jan. 2011.

[62] Y. W. Gu, M. S. Yong, B. Y. Tay, and C. S. Lim, "Synthesis and bioactivity of porous Ti alloy prepared by foaming with TiH2," *Materials Science and Engineering: C*, vol. 29, no. 5, pp. 1515–1520, Jun. 2009.

[63] J. Baumeister, H. Schrader, and F. G. zur Forderung der Angewandten Forschung, "Methods for manufacturing foamable metal bodies," Sep. 1992.

[64] A. Verdooren, H. M. Chan, J. L. Grenestedt, M. P. Harmer, and H. S. Caram, "Production of Metallic Foams From Ceramic Foam Precursors," *Adv. Eng. Mater.*, vol. 6, no. 6, pp. 397–399, Jun. 2004.

[65] J. P. Li, S. H. Li, K. de Groot, and P. Layrolle, "Preparation and Characterization of Porous Titanium," *Key Engineering Materials*, vol. 218, pp. 51–54, 2002.

[66] J. D. Bobyn, G. J. Stackpool, S. A. Hacking, M. Tanzer, and J. J. Krygier, "Characteristics of bone ingrowth and interface mechanics of a new porous tantalum biomaterial," *J Bone Joint Surg Br*, vol. 81, no. 5, pp. 907–914, Sep. 1999.

[67] N. G. Davis, J. Teisen, C. Schuh, and D. C. Dunand, "Solid-state foaming of titanium by superplastic expansion of argon-filled pores," *Journal of Materials Research*, vol. 16, no. 5, pp. 1508–1519, Jan. 2011.

[68] J. M. Kendall, M. C. Lee, and T. G. Wang, "Metal shell technology based upon hollow jet instability," *Journal of Vacuum Science and Technology*, vol. 20, no. 4, pp. 1091–1093, Apr. 1982.

[69] D. J. Sypeck, P. A. Parrish, and H. N. G. Wadley, “Novel Hollow Powder Porous Structures,” *MRS Proceedings*, vol. 521, p. 43, Feb. 2011.

[70] M. Bram, C. Stiller, H. P. Buchkremer, D. Stöver, and H. Baur, “High-Porosity Titanium, Stainless Steel, and Superalloy Parts,” *Adv. Eng. Mater.*, vol. 2, no. 4, pp. 196–199, Apr. 2000.

[71] C. E. Wen, M. Mabuchi, Y. Yamada, K. Shimojima, Y. Chino, and T. Asahina, “Processing of biocompatible porous Ti and Mg,” *Scripta Materialia*, vol. 45, no. 10, pp. 1147–1153, Nov. 2001.

[72] C. E. Wen, Y. Yamada, K. Shimojima, Y. Chino, T. Asahina, and M. Mabuchi, “Processing and mechanical properties of autogenous titanium implant materials.,” *J Mater Sci Mater Med*, vol. 13, no. 4, pp. 397–401, Apr. 2002.

[73] J. O. Osorio-hernández, M. A. Suarez, R. Goodall, G. A. Lara-rodriguez, I. Alfonso, and I. A. Figueroa, “Manufacturing of open-cell Mg foams by replication process and mechanical properties,” *Materials & Design*, pp. 1–24, Jul. 2014.

[74] R. Miyao, M. Omori, F. Watari, A. Yokoyama, H. Matsuno, T. Hirai, and T. Kawasaki, “Fabrication of Functionally Graded Implants by Spark Plasma Sintering and their Properties.,” *Journal of the Japan Society of Powder and Powder Metallurgy*, vol. 47, no. 11, pp. 1239–1242, 2000.

[75] Y. Zheng, S. Sridhar, and K. C. Russell, “Controlled porosity alloys through solidification processing: a modelling study,” *Advances in Porous Materials*, pp. 365–370, 1994.

[76] L. P. Martin, D. Orlikowski, and J. H. Nguyen, “Fabrication and characterization of graded impedance impactors for gas gun experiments from tape cast metal powders,” vol. 427, 2006.

[77] L. P. Martin, J. R. Patterson, D. Orlikowski, and J. H. Nguyen, “Application of tape-cast graded impedance impactors for light-gas gun experiments,” *Journal of Applied Physics*, vol. 102, no. 2, pp. 023507–11, Jul. 2007.

[78] J. W. Lee, I. H. Lee, and D.-W. Cho, “Development of micro-stereolithography technology using metal powder,” *Microelectronic Engineering*, vol. 83, no. 4, pp. 1253–1256, Apr. 2006.

[79] P. J. Bartolo and J. Gaspar, “Metal filled resin for stereolithography metal part,” *CIRP Annals - Manufacturing Technology*, vol. 57, no. 1, pp. 235–238, 2008.

[80] R. Liska, M. Schuster, R. Inführ, C. Turecek, C. Fritscher, B. Seidl, V. Schmidt, L. Kuna, A. Haase, F. Varga, H. Lichtenegger, and J. Stampfl, “Photopolymers for rapid prototyping,” *J Coat Technol Res*, vol. 4, no. 4, pp. 505–510, Nov. 2007.

[81] M. Schuster, C. Turecek, F. Varga, H. Lichtenegger, J. Stampfl, and R. Liska, “3D-shaping of biodegradable photopolymers for hard tissue replacement,” *Applied Surface Science*, vol. 254, no. 4, pp. 1131–1134, Dec. 2007.

[82] S. H. Masood and W. Q. Song, “Development of new metal/polymer materials for rapid tooling using Fused deposition modelling,” *Materials & Design*, vol. 25, no. 7, pp. 587–594, Oct. 2004.

[83] S. Hwang, E. I. Reyes, K.-S. Moon, R. C. Rumpf, and N. S. Kim, “Thermo-mechanical Characterization of Metal/Polymer Composite Filaments and Printing Parameter Study for Fused Deposition Modeling in the 3D Printing Process,” *Journal of Elec Materi*, vol. 44, no. 3, pp. 771–777, Oct. 2014.

[84] M. Nikzad, S. H. Masood, and I. Sbarski, “Thermo-mechanical properties of a highly filled polymeric composites for Fused Deposition Modeling,” *Materials & Design*, vol. 32, no. 6, pp. 3448–3456, Jun. 2011.

[85] H. Hellebrand, “Tape Casting,” in *Materials science and technology*, vol. 11, no. 7, Wiley-VCH Verlag GmbH & Co. KGaA, 1996, pp. 190–260.

[86] G. N. Howatt and N. J. Metuchen, “Method of producing high dielectric high insulation ceramic plates,” US2582993, 22-Jan-1952.

[87] R. E. Mistler and E. R. Twiname, *Tape Casting*. Wiley-American Ceramic Society, 2000.

[88] A. Mukherjee, B. Maiti, A. Das Sharma, R. N. Basu, and H. S. Maiti, “Correlation between slurry rheology, green density and sintered density of tape cast yttria stabilised zirconia,” *Ceramics International*, vol. 27, no. 7, pp. 731–739, Jan. 2001.

[89] W. J. Clegg, K. Kendall, N. M. Alford, T. W. Button, and J. D. Birchall, "A simple way to make tough ceramics," *Nature*, vol. 347, no. 6292, pp. 455–457, Oct. 1990.

[90] R. N. Katz, "Characterization of Ceramic Powders," in *Treatise on Materials Science and Technology*, vol. 9, Elsevier, 1976, pp. 35–49.

[91] T. Allen and R. Davies, *Modern Aspects of Particle-Size Analysis*. Advances in Ceramics, 1987.

[92] R. K. McGeary, "Mechanical Packing of Spherical Particles," *Journal of the American Ceramic Society*, vol. 44, no. 10, pp. 513–522, Oct. 1961.

[93] R. J. Brook, R. W. Cahn, P. Haasen, and E. J. Kramer, "Processing of Ceramics," in *Materials science and technology*, Wiley-VCH, 1996, p. 999.

[94] D. J. Shanefield, *Organic Additives and Ceramic Processing*. Boston, MA: Springer US, 1995.

[95] P. Boch and T. Chartier, "Tape Casting and Properties of Mullite and Zirconia-Mullite Ceramics," *Journal of the American Ceramic Society*, vol. 74, no. 10, pp. 2448–2452, Oct. 1991.

[96] H. Burrell, "*Solubility Parameters*," *Interchem. Rev.*, vol. 1, pp. 3–16, 1995.

[97] R. M. German, *Powder Metallurgy Science*. 1997.

[98] P. Freni, P. Tecchio, S. Rollino, and B. De Benedetti, "Porosity characterization of biomedical magnesium foams produced by Spark Plasma Sintering," presented at the 2014 IEEE International Symposium on Medical Measurements and Applications (MeMeA), 2014, pp. 1–6.

[99] F. Zhang, E. Otterstein, and E. Burkel, "Spark Plasma Sintering, Microstructures, and Mechanical Properties of Macroporous Titanium Foams," *Adv. Eng. Mater.*, vol. 12, no. 9, pp. 863–872, Sep. 2010.

[100] U. Anselmi-Tamburini, S. Gennari, J. E. Garay, and Z. A. Munir, "Fundamental investigations on the spark plasma sintering/synthesis process," *Materials Science and Engineering: A*, vol. 394, no. 1, pp. 139–148, Mar. 2005.

[101] Z. A. Munir, U. Anselmi-Tamburini, and M. Ohyanagi, “The effect of electric field and pressure on the synthesis and consolidation of materials: A review of the spark plasma sintering method,” *J Mater Sci*, vol. 41, no. 3, pp. 763–777, Feb. 2006.

[102] J. Banhart, “Manufacture, characterisation and application of cellular metals and metal foams,” *Progress in Materials Science*, vol. 46, no. 6, pp. 559–632, Jan. 2001.